

Study of foam in model fractures: coarsening, gas trapping and gravity effects

Li, K.

DOI

[10.4233/uuid:d2ff078a-70f3-4d41-944d-44a81ed6fa07](https://doi.org/10.4233/uuid:d2ff078a-70f3-4d41-944d-44a81ed6fa07)

Publication date

2022

Document Version

Final published version

Citation (APA)

Li, K. (2022). *Study of foam in model fractures: coarsening, gas trapping and gravity effects*. [Dissertation (TU Delft), Delft University of Technology]. <https://doi.org/10.4233/uuid:d2ff078a-70f3-4d41-944d-44a81ed6fa07>

Important note

To cite this publication, please use the final published version (if applicable). Please check the document version above.

Copyright

Other than for strictly personal use, it is not permitted to download, forward or distribute the text or part of it, without the consent of the author(s) and/or copyright holder(s), unless the work is under an open content license such as Creative Commons.

Takedown policy

Please contact us and provide details if you believe this document breaches copyrights. We will remove access to the work immediately and investigate your claim.

**STUDY OF FOAM IN MODEL
FRACTURES: COARSENING, GAS
TRAPPING AND GRAVITY EFFECTS**

Study of Foam in Model Fractures: Coarsening, Gas Trapping and Gravity Effects

Proefschrift

ter verkrijging van de graad van doctor aan de Technische
Universiteit Delft,
op gezag van de Rector Magnificus prof.dr.ir. T.H.J.J. van der Hagen,
voorzitter van het College voor Promoties,
in het openbaar te verdedigen op
maandag 31 januari 2022 om 12.30 uur

door

Kai LI

Ingenieur Technische Aardwetenschappen, Technische Universiteit Delft, Nederland
geboren te Daoshiqiao, China

Dit proefschrift is goedgekeurd door de promotoren.

Samenselling promotiecommissie bestaat uit:

Rector Magnificus,	voorzitter
Prof.dr. W.R. Rossen	Technische Universiteit Delft, promotor
Dr. K-H.A.A. Wolf	Technische Universiteit Delft, promotor

Onafhankelijke leden:

Prof.dr. H. Bertin	Université de Bordeaux, France
Prof.dr. R.A.W.M. Henkes	Technische Universiteit Delft
Prof.dr. P.L.J. Zitha	Technische Universiteit Delft
Dr. A. Pluymakers	Technische Universiteit Delft
Dr. S. Vincent-Bonnieu	European Space Agency, Leiden, the Netherlands

This doctoral research is part of Joint Industry Project (JIP) on Foam for Enhanced Oil Recovery at Delft University of Technology, the Netherlands. We thank Shell, Equion, Engie, ConocoPhillips and PEMEX for sponsoring this project.



Keywords: Foam, naturally fractured reservoirs, fractures, image analysis, water saturation, capillary pressure, local equilibrium, gas trapping, capillary number, coarsening, gravity segregation

Copyright © 2022 by Kai LI

Printed by Gildeprint

ISBN: 978-94-6366-496-7

SUMMARY

Naturally fractured reservoirs (NFRs) gain much attention worldwide because they are often encountered in aquifer remediation, CO₂ sequestration, and hydrocarbon extraction. In hydrocarbon extraction, however, oil recovery by gas injection in NFRs is usually low, because of poor sweep efficiency. During gas injection, the displacement front is unstable. Conformance problems, such as gravity override, viscous fingering, and channeling, take place because the gas has a lighter density and lower viscosity compared to reservoir fluids, and tends to flow preferably through high-permeability zones in heterogeneous reservoirs. In addition, open fractures can have much greater conductivity than the matrix. As a result, gas flows through fractures, leaving much of the matrix unswept. Foam, by adding surfactant solution to gas injection, can effectively mitigate conformance problems by greatly reducing the mobility of gas. During foam flooding in porous media, the displacement front is more stable, and more gas is diverted to unswept zones, hence improving the sweep and increasing oil recovery. Foam can also be created in fractures, where it builds up a viscous pressure gradient and thus diverts the flow of gas into the matrix. As a result, the sweep is improved. In the field, foam pilots have achieved an increase in oil production rate and a reduction in gas/oil ratio. Despite this success, foam application in NFRs is still much less understood than in unfractured porous media.

In this dissertation, we aim to expand our understanding of foam in fractures through an experimental approach. To this end, we create four 1-m-long, 15-cm-wide glass model fractures (Models A, B, C and D) with different roughness and hydraulic apertures. Each model consists of two 2-cm-thick glass plates. The top plate is smooth and the bottom plate is roughened on the side facing the top plate. Between the two plates is a slit-like channel representing a single geological fracture. Model A has a roughened plate with a regular roughness. Models B, C and D, with increasing hydraulic apertures, use the same roughened plate with an irregular roughness. We profile the roughness of the roughened plates and study the aperture distribution of the model fractures to characterize the geometry of the model fractures. With local hills (maxima of height) and valleys (minima of height) on the roughened plates, the distribution of aperture of model fractures can be represented as a 2D network of pore bodies and pore throats. In the experiments, we inject pre-generated foam into the model fractures. We study foam behavior after foam flow reaches steady-state. As our models are transparent, we use a high-speed camera to directly visualize and record images of foam in the model fractures. Using ImageJ software, we analyze foam images to quantify the properties of the foam.

In **Chapter 1**, we provide an introduction of NFRs, gas injection in NFRs, foam injection, and foam injection in NFRs and its challenges. We also list the objectives and scope of this dissertation.

In **Chapter 2**, we summarize the methodologies adopted in this dissertation. We first illustrate our experimental setup and materials. We then describe the manufacturing procedures of the

four model fractures and explain how to characterize the geometries of model fractures. We afterward demonstrate how to quantify different properties of the foam using image analysis.

In **Chapter 3**, we report a novel technique of estimation of water saturation and capillary pressure of foam in two model fractures (Models A, and B) with different roughness and hydraulic apertures. In this chapter, foam is first pre-generated and then injected into the model fractures. The inlet and outlet valves are closed for 24 hours after foam reaches steady-state. We use the high-speed camera to visualize foam in the fractures, and estimate water saturation and capillary pressure by analyzing foam images and fracture geometry. We find that water in foam resides in locations of narrow aperture (water zones), Plateau borders, lamellae between bubbles, and water films on glass walls. Water-filled zones of narrow aperture and Plateau borders account for almost all the water. During the re-distribution of water and gas in static foam, in-flow and out-flow of water must take paths along Plateau borders and water-filled zones, as they are the only continuous paths for water flow. In both model fractures, the decrease in water saturation coincides with an increase in capillary pressure, as expected. This analysis is possible because aperture varies throughout our model fractures, unlike most microfluidic devices with uniform depth.

In **Chapter 4**, we study foam coarsening in the two model fractures (Models A, and B) with different roughness and hydraulic apertures. We inject pre-generated foam at different foam qualities into the model fractures. After foam reaches steady-state, we shut the inlet and outlet valves of the fractures for 24 hr. Foam coarsens by gas diffusion during this period. We use the high-speed camera to record images of the static foam during coarsening at two fixed locations in the fracture: 19 and 73 cm from the inlet, separately. We then use ImageJ software to process the images to study foam texture and quantify the coarsening process. By correlating the aperture histogram of model fractures and water-occupied area fraction, we estimate the local aperture at water-gas interfaces at each specific coarsening time. Using the local aperture, we further estimate the height of lamellae available for gas diffusion at the end of the coarsening experiments. Based on this information, we discuss whether coarsening stops at the end of the coarsening experiments because bubbles are at equal pressure, or slows nearly to a stop because bubbles lose contact through lamellae. Coarsening studies of foam in bulk and microfluidics assume coarsening slows and stops when lamella curvature is zero. We show in our model fractures that the lack of lamellae in wet foams can also play a part. In addition, we adopt the novel technique reported in Chapter 3 to calculate water saturation and capillary pressure of foam in the model fractures. We then explain how these foam properties affect its coarsening behavior.

In **Chapter 5**, we report foam experiments in one model fracture (Model B) to understand gas trapping in fractures and how it affects foam behavior. This chapter is part of a continuing program to determine how foam behaves as a function of the geometry of the fracture pore space (AlQuaimi and Rossen, 2018a). We find that the local equilibrium (LE) of foam (where the rate of bubble generation equals that of bubble destruction) has been achieved within the 1-m-long model fracture. Foam texture becomes finer and less gas is trapped as interstitial velocity and pressure gradient increase. Shear-thinning rheology of foam has also been observed. The fraction of trapped gas is significantly lower in our model fracture (less than 7%)

than in unfractured geological porous media. At the extreme, when velocity increases to 7 mm/s, there is no gas trapped inside the fracture. The experimental results of trapped-gas fraction correlate well with the correlation of AlQuaimi and Rossen (2018a) for fracture-like porous media. This suggests that the correlation can also be applied to gas trapping in fractures with other geometries.

In **Chapter 6**, we report foam experiments in three model fractures (Models B, C and D) to investigate how gravity affects foam in open vertical fractures. The three model fractures have the same roughness, but with increasing hydraulic apertures from Models B to D. We conduct foam experiments by horizontal injection in the three model fractures placed horizontally and sideways, i.e. with the model fractures turned on their long side, and in Model B placed vertically with injection upward or downward. We find that foam reaches LE in horizontal-flow experiments in all three model fractures placed horizontally and in the vertical-flow experiments in Model B. In fractures with a larger hydraulic aperture, foam is coarser, due to less in-situ foam generation. In the vertical-flow experiments in Model B, we find that the properties of the foam are different in upward and downward flow. Compared to downward flow, upward flow creates foam with a finer texture, as sections near the inlet are in a wetter state, which benefits in-situ foam generation. In addition, less gas is trapped during upward flow, as gravitational potential helps overcome capillarity and moves bubbles upward. In the sideways-flow experiments, gravity segregation takes place. As a result, drier foam propagates along the top of the fractures and wetter foam along the bottom. The segregation is more significant in fractures with a larger hydraulic aperture. At foam quality 0.8, gas saturation is 27.7% greater at the top than the bottom for Model D, and 19.3% and 10.8% for Models C and B, respectively. Despite the gravity segregation in all three model fractures, water and gas are not completely segregated. All three model fractures thus represent a capillary transition zone, with greater segregation with increasing aperture. Our results suggest that the propagation of foam in vertical natural fractures meters tall and tens of meters long, with an aperture of hundreds of microns or greater, is problematic. Gravity segregation in foam would weaken its capacity in the field to maintain uniform flow and divert gas in a tall fracture over large distances.

In **Chapter 7**, we summarize the conclusions and implications of this dissertation. We also propose additional aspects of foam in fractures that deserve further study.

SAMENVATTING

Natuurlijk gebroken reservoirs (NFR's) krijgen wereldwijd veel aandacht omdat ze van belang zijn voor de sanering van watervoerende lagen, de opslag van CO₂ en de winning van koolwaterstoffen. Bij koolwaterstofextractie is de oliewinning door gasinjectie in NFR's echter gewoonlijk laag vanwege de lage sweep-efficiëntie. Tijdens gasinjectie is het verplaatsingsfront onstabiel. Conformiteitsproblemen, zoals bovenlangs passeren door zwaartekracht, viskeuze fingering en kanaalvorming, treden op omdat het gas een lagere dichtheid en lagere viscositeit heeft in vergelijking met reservoirvloeistoffen, en de neiging heeft om in heterogene reservoirs bij voorkeur door zones met hoge permeabiliteit te stromen. Bovendien kunnen open breuken een veel grotere doorlatendheid hebben dan de matrix. Als gevolg hiervan stroomt gas door breuken, waardoor een groot deel van de matrix niet wordt behandeld. Schuim, gemaakt door een oppervlakteactieve oplossing toe te voegen aan gasinjectie, kan conformiteitsproblemen effectief verminderen door de mobiliteit van gas aanzienlijk te verminderen. Bij stroming van schuim in poreuze media is het verdringingsfront stabiel en wordt meer gas omgeleid naar unswept zones, waardoor de sweep-efficiëntie wordt verbeterd en de oliewinning toeneemt. Schuim kan ook ontstaan in breuken, waar het een viskeuze drukgradiënt opbouwt en zo de gasstroom in de matrix omleidt. Als resultaat wordt de sweep-efficiëntie verbeterd. In veldtesten is met schuim een verhoging van de olieproductiesnelheid en een verlaging van de gas/olieverhouding bereikt. Ondanks dit succes wordt schuimtoepassing in NFR's nog steeds veel minder begrepen dan in poreuze media zonder breuken.

In dit proefschrift willen we ons begrip van schuim in breuken uitbreiden door middel van een experimentele benadering. Hiervoor creëren we vier glasmodelbreuken van één meter lang en 15 centimeter breed (modellen A, B, C en D) met verschillende ruwheden en hydraulische openingen. Elk model bestaat uit twee glasplaten van twee centimeter dik. De bovenplaat is glad en de onderplaat is opgeruwd aan de naar de bovenplaat gerichte zijde. Tussen de twee platen bevindt zich een spleetachtig kanaal dat een enkele geologische breuk voorstelt. Model A heeft een opgeruwde plaat met een regelmatige ruwheid. Modellen B, C en D, met toenemende hydraulische openingen, gebruiken dezelfde opgeruwde plaat met een onregelmatige ruwheid. We maken een profiel van de ruwheid van de opgeruwde platen en bestuderen de apertuurverdeling van de modelbreuken om de geometrie van de modelbreuken te karakteriseren. Met lokale heuvels (maxima van hoogte) en valleien (minima van hoogte) op de opgeruwde platen, kan de verdeling van de opening van modelbreuken worden weergegeven als een 2D-netwerk van poriëlichamen en poriëvernauwingen. In de experimenten injecteren we vooraf gegenereerd schuim in de modelbreuken. We bestuderen het schuimgedrag nadat de schuimstroom een stabiele toestand heeft bereikt. Omdat onze modellen transparant zijn, gebruiken we een hogesnelheidscamera om beelden van schuim in de modelbreuken direct te visualiseren en vast te leggen. Met behulp van ImageJ-software analyseren we de gemaakte schuimafbeeldingen om de eigenschappen van het schuim te kwantificeren.

In **Hoofdstuk 1** geven we een introductie van NFR's, gasinjectie in NFR's, schuiminjectie en schuiminjectie in NFR's en de uitdagingen ervan. We vermelden ook de doelstellingen en reikwijdte van dit proefschrift.

In **Hoofdstuk 2** vatten we de methodologieën samen die in dit proefschrift zijn gebruikt. We illustreren eerst onze experimentele opstelling en materialen. Vervolgens beschrijven we de fabricageprocedures van de vier modelbreuken en leggen we uit hoe de geometrieën van modelbreuken kunnen worden gekarakteriseerd. Daarna demonstreren we hoe we verschillende eigenschappen van het schuim kunnen kwantificeren met behulp van beeldanalyse.

In **Hoofdstuk 3** rapporteren we een nieuwe techniek voor het schatten van waterverzadiging en capillaire druk van schuim in twee modelbreuken (Modellen A en B) met verschillende ruwheid en hydraulische openingen. In dit hoofdstuk wordt eerst schuim gegenereerd en vervolgens in de modelbreuken geïnjecteerd. Nadat het schuim de stabiele toestand heeft bereikt, de inlaat- en uitlaatkranen worden gedurende 24 uur gesloten. We gebruiken de hogesnelheidscamera om schuim in de breuken te visualiseren, en schatten waterverzadiging en capillaire druk door schuimbeelden en breukgeometrie te analyseren. Dit laat zien dat water in schuim zich bevindt op de locaties met nauwe openingen (waterzones), Plateaugrenzen, en dat er zich lamellen vormen tussen bellen en waterfilms op de glazen wanden. Vrijwel al het water bevindt zich in de water gevulde zones op de nauwe opening en Plateaugrenzen. Tijdens de herverdeling van water en gas in statisch schuim moeten in- en uitstroom van water paden langs Plateaugrenzen en watergepulde zones, aangezien dit de enige doorlopende paden voor waterstroming zijn. In beide modelbreuken valt de afname van de waterverzadiging samen met een toename van de capillaire druk, net zoals in geologische poreuze media. Onze analyse wordt mogelijk gemaakt doordat de opening in onze modelbreuken varieert, in tegenstelling tot de meeste microfluidische apparaten met uniforme diepte.

In **Hoofdstuk 4** bestuderen we schuimvergroving, het grover worden van de schuim textuur, in de twee modelbreuken (Modellen A en B) met verschillende ruwheid en hydraulische openingen. We injecteren voorgevormde schuim met verschillende schuimkwaliteiten in de modelbreuken. Nadat het schuim een stabiele toestand heeft bereikt, sluiten we de inlaat- en uitlaatkranen van de breuken gedurende 24 uur. Schuim wordt in deze periode grover door gasdiffusie. Met de hogesnelheidscamera nemen we beelden op van het statisch schuim tijdens de vergroving op twee vaste locaties in de breuk: 19 en 73 cm vanaf de inlaatkraan. Vervolgens gebruiken we ImageJ-software om de afbeeldingen te verwerken om de schuimtextuur te bestuderen en het vergrogingsproces te kwantificeren. Door het correleren van het apertuurhistogram van modelbreuken met de waterbezette oppervlaktefractie, kunnen we de lokale apertuur bij water-gasinterfaces inschatten voor elke specifieke vergrovingstijd gedurende het hele proces. Met behulp van de lokale opening schatten we aan het einde van de vergrovingsexperimenten de hoogte van de beschikbare lamellen voor gasdiffusie. Op basis van deze informatie bespreken we of de vergroving stopt aan het einde van de vergrovingsexperimenten omdat bellen onder gelijke druk staan, of bijna stopt omdat bellen het contact verliezen door lamellen. Vergrovingstudies van schuim in bulk en microfluidica gaan ervan uit dat de vergroving vertraagt en stopt wanneer de kromming van de lamellen nul

is. We laten in onze modelbreuken zien dat het ontbreken van lamellen in natte schuimen ook een rol kan spelen. Daarnaast gebruiken we de nieuwe techniek beschreven in Hoofdstuk 3 om de waterverzadiging en capillaire druk van schuim in de modelbreuken te berekenen. Vervolgens leggen we uit hoe deze schuimeigenschappen het vergrotingsgedrag beïnvloeden.

In **Hoofdstuk 5** bespreken we schuimexperimenten in één modelbreuk (Model B) om inzicht te krijgen in gasopsluiting in breuken en hoe dit het schuimgedrag beïnvloedt. Dit hoofdstuk maakt deel uit van een doorlopend programma om te bepalen hoe schuim zich gedraagt als een functie van de geometrie van de breuk-porieruimte (AlQuaimi en Rossen, 2018a). We vinden dat het lokale evenwicht (LE) van schuim (waarbij de snelheid van bellenvorming gelijk is aan die van bellenvernietiging) is bereikt binnen de 1 m lange modelbreuk. De schuimtextuur wordt fijner en er wordt minder gas vastgehouden naarmate de interstitiële snelheid en de drukgradiënt toenemen. Afschuifverduunningsreologie van schuim is ook waargenomen. De fractie van ingesloten gas is significant lager in onze modelbreuk (minder dan 7%) dan in niet-gebroken geologische poreuze media. In het uiterste geval, wanneer de snelheid toeneemt tot 7 mm/s, zit er geen gas meer opgesloten in de breuk. De experimentele resultaten van de ingesloten gasfractie correleren goed met de correlatie van AlQuaimi en Rossen (2018a) voor poreuze media met breuken. Dit suggereert dat de correlatie ook kan worden toegepast op gasopsluiting in breuken met andere geometrieën.

In **Hoofdstuk 6** bespreken we schuimexperimenten in drie modelbreuken (Modellen B, C en D) om te onderzoeken hoe zwaartekracht schuim beïnvloedt in open verticale breuken. De drie modelbreuken hebben dezelfde ruwheid, maar met toenemende hydraulische openingen van Model B naar D. We voeren schuimexperimenten uit door horizontale injectie in de drie modelbreuken die horizontaal en zijwaarts zijn geplaatst, dat wil zeggen met de modelbreuken gedraaid op hun lange zijde, en in Model B verticaal geplaatst met injectie naar boven of naar beneden. Schuim bereikt LE in horizontale stromingsexperimenten in alle drie de modelbreuken en in de verticale stromingsexperimenten in Model B. In breuken met een grotere hydraulische opening is schuim grover, vanwege minder in-situ schuimvorming. In de verticale stromingsexperimenten in Model B vinden we dat de eigenschappen van het schuim verschillend zijn in opwaartse en neerwaartse stroming. Vergeleken met neerwaartse stroming, creëert opwaartse stroming schuim met een fijnere textuur, omdat secties nabij de inlaat in een nattere toestand zijn, wat de in-situ schuimvorming ten goede komt. Bovendien wordt er minder gas vastgehouden tijdens opwaartse stroming, omdat de zwaartekracht helpt capillariteit te overwinnen en bellen naar boven laat bewegen. In de zijwaartse stromingsexperimenten vindt zwaartekrachtsegregatie plaats. Als gevolg hiervan plant droger schuim zich voort langs de bovenkant van de breuken en natter schuim langs de onderkant. De segregatie is belangrijker bij breuken met een grotere hydraulische opening. Bij schuimkwaliteit 0,8 is de gasverzadiging aan de bovenkant 27,7% groter dan aan de onderkant voor Model D en respectievelijk 19,3% en 10,8% voor Model C en B. Ondanks de zwaartekrachtsegregatie in alle drie de modelbreuken, zijn water en gas niet volledig gescheiden. Alle drie de modelbreuken vertegenwoordigen dus een capillaire overgangszone, met grotere segregatie met toenemende opening. Onze resultaten suggereren dat de verspreiding van schuim in verticale natuurlijke breuken van meters hoog en tientallen meters lang, met een opening van honderden microns of meer, problematisch is.

Zwaartekrachtsegregatie in schuim zou zijn capaciteit in het veld verzwakken om een uniforme stroming te handhaven en gas in een grote breuk over grote afstanden af te leiden.

In **Hoofdstuk 7** vatten we de conclusies en implicaties van dit proefschrift samen. We stellen ook aanvullende aspecten voor van schuim in breuken die nader onderzoek verdienen.

1 Introduction

1.1 Naturally fractured reservoirs

Naturally fractured reservoirs (NFRs) contain macroscopic fractures created by earth stresses that exceed the rupture strength of the rock. A fracture, as a quasi-planar discontinuity or mechanical parting caused by brittle failure (Narr et al., 2006), can greatly influence the permeability and porosity of reservoirs, hence affecting flow dynamics in the reservoirs (Nelson, 2001). NFRs exist in almost every lithology around the world (Narr et al., 2006), and gain much attention because of their large reserves of groundwater, geothermal energy, coalbed methane, and hydrocarbons (Persoff and Pruess, 1995), and as potential storage sites for CO₂ sequestration (March et al., 2018). In this dissertation, we discuss mainly hydrocarbon NFRs that contain oil and gas.

The Middle East accounts for 48% of global proved oil reserves and 40% of proved gas reserves (BP statistical review, 2021). Many of these reserves are characterized as carbonate NFRs (Cosentino et al., 2002; Phelps and Strauss, 2002). Despite the large reserves, NFRs are in general known for the absence of a transition zone, nonuniform fluid properties with depth, production anomalies, and large ratios of produced gas to oil and water to oil (Dominguez, 1992). In NFRs, flow behavior is complex because of the variations in fracture density, connectivity, and orientation. In addition, the difference in storage capacity and permeability in fractures and matrix makes flow behavior in NFRs even more difficult to predict (Aguilera, 1995; Nelson, 2001). Therefore, implementing an optimized production strategy in NFRs requires a good understanding of fundamental aspects of flow in fractures.

Fractures in NFRs can be open, partially open, or closed due to mineral sedimentation (van Golf-Racht, 1982). They have different lengths and heights, dip angles, apertures, densities, and morphology. Understanding the overall behavior of NFRs requires understanding flow dynamics in a single fracture (Rossen and Kumar, 1992). As shown in Fig. 1.1, a single open fracture consists of two walls with roughness. The gap between the two walls provides a flow channel with variable apertures, and the points where the two walls contact each other are called asperities (Brown, 1987; Odling, 1994; Olsson and Barton, 2001).

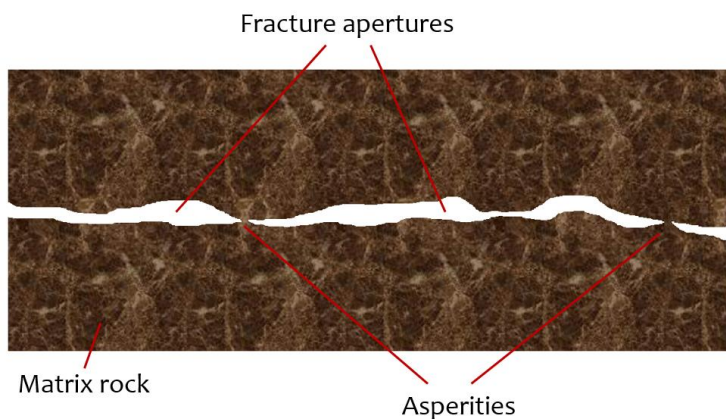


Figure 1.1. Schematic of a fracture with apertures and asperities.

Since the 1960s there have been many studies of flow in fractures to examine relative permeability and capillary pressure (Pruess and Tsang, 1990; Maloney and Doggett, 1997; Lian and Cheng, 2012). Romm (1966) observed a linear relationship between relative permeabilities and water saturation in fractures. This is valid only if capillarity is insignificant compared with viscous and gravity forces (Rossen and Kumar, 1992; Pieters and Graves, 1994; Persoff and Pruess, 1995). In fractures, capillarity is a function of aperture distribution, interfacial tension, and wettability. Aperture distribution is in part dependent on the roughness of the fractures. The roughness causes wide and narrow apertures within the space in fractures. Thus, a fracture can also be represented as a 2D network of pore bodies and pore throats (Tsang, 1984; Persoff et al., 1991; Rossen and Kumar, 1992; Hughes and Blunt, 2001).

1.2 Gas injection in NFRs

Gas injection, as an enhanced oil recovery (EOR) method of injecting an immiscible gas (nitrogen, flue gas) or a miscible gas (carbon dioxide, hydrocarbon gas) into reservoirs, can increase oil recovery (Pope, 1980). As of 2017, gas-injection projects account for 37.9% of EOR projects worldwide (IEA, 2019). During gas injection, both the residual oil saturation and oil viscosity may be reduced (Rodríguez et al., 2001; Sanchez Bujanos et al., 2005). In the case of miscible gas injection, the oil is swelled and the interfacial boundary between the gas and the oil disappears (Kalra and Wu, 2014; Seyyedsar et al., 2015). As a result, the microscopic displacement efficiency is improved at the pore level, with an increase in oil recovery.

However, gas injection often has an unstable displacement front and suffers from poor sweep efficiency due to conformance problems, including gravity override, viscous fingering, and channeling (Lake et al., 2014; Kim et al., 2005). This is because gas has a lower density and lower viscosity compared to reservoir fluids, and the reservoir is heterogeneous. In NFRs, the performance of gas injection is even poorer, with a much-lower sweep efficiency (Schechter et al., 1996), because open fractures can have an aperture of hundreds of microns or more (Luthi and Souhaite, 1990), with a much greater flow conductivity than the adjacent matrix. Therefore, oil and gas would preferably flow through high-permeability fracture channels, leading to an early breakthrough and leaving much of the matrix unswept. Allan and Sun (2003) conducted a production review of 100 NFRs and showed that the recovery in NFRs is somewhat lower than that in conventional reservoirs. To increase the recovery of hydrocarbons that are left behind in the matrix, an optimized EOR strategy is required. In the field, to mitigate the conformance problems of gas injection, water alternating gas (WAG) (Teigland and Kleppe, 2006; Kamali et al., 2017) and foam-assisted WAG (FAWAG) (Spirov et al., 2012; Groenenboom et al., 2017), also called surfactant alternating gas (SAG), have been implemented. In this dissertation, we focus on foam EOR in NFRs. Our results would also have an application to foam aquifer remediation and CO₂ sequestration.

1.3 Foam injection

1.3.1 Foam and its applications

Foam is a dispersion of gas in a liquid, where gas bubbles are separated by interconnected aqueous films. The films, called lamellae, are stabilized by surfactants (Rossen, 1996; Gauglitz et al., 2002; Lake et al., 2014). In this dissertation, we discuss foam in porous media, where foam bubbles are believed to have a size equal to or larger than the pore body. Foam has many applications in underground settings, such as matrix acid diversion in well stimulation (Thompson and Gdanski, 1993), aquifer remediation (Portois et al., 2018), and EOR (Kovscek and Radke, 1994; Rossen, 1996). In acid stimulation, foam can be used as a diverting agent in almost every type of completion to improve stimulation coverage across the zone of interest (Kennedy et al., 1992). In aquifer remediation, foam is applied to selectively block high-permeability layers, and displace dense non-aqueous phase liquid (DNAPL) from low-permeability layers that are often unswept during a conventional remediation process (Hirasaki et al., 1997). In EOR, by adding surfactant solution in gas injection, foam can effectively mitigate all conformance problems by reducing the mobility of gas by a factor of hundreds or more (Tang and Kovscek, 2006).

1.3.2 Foam in EOR

Foam in EOR has been studied theoretically and experimentally for decades (Bond and Holbrook, 1958; Fried, 1961; Bernard et al., 1980; Rossen, 1996). During foam injection, gas relative permeability is reduced due to gas trapping, and gas apparent viscosity is increased due to capillary forces and drag on moving lamellae. The mobility of gas is thus greatly reduced. As a result, the displacement front is more stable, and more gas is diverted to unswept zones, hence improving sweep, reducing gas/oil ratio, and increasing oil recovery (Patzek, 1996; Rossen, 1999).

In porous media, the main mechanisms of foam generation are snap-off, lamella division, and leave-behind (Nguyen, 2004). As shown in Fig. 1.2, snap-off occurs when gas invades a pore throat and then liquid accumulates in the throat, eventually bridging and blocking the throat (Rossen, 2003). In particular, “Roof snap-off” takes place when gas displaces liquid from a narrow pore throat and a wide liquid-filled pore body. Lamella division takes place when a lamella stretches around a branch point in its flow path and then splits in two as it encounters multiple downstream pore throats. Leave-behind occurs when gas invades adjacent liquid-filled pore bodies; a liquid lens is left in the pore throat in between. In porous media, foam with a finer texture (smaller bubbles) and a larger bubble density gives a greater reduction of gas mobility, because its higher lamella density per unit of length gives greater resistance to the flow (Hirasaki and Lawson, 1985).

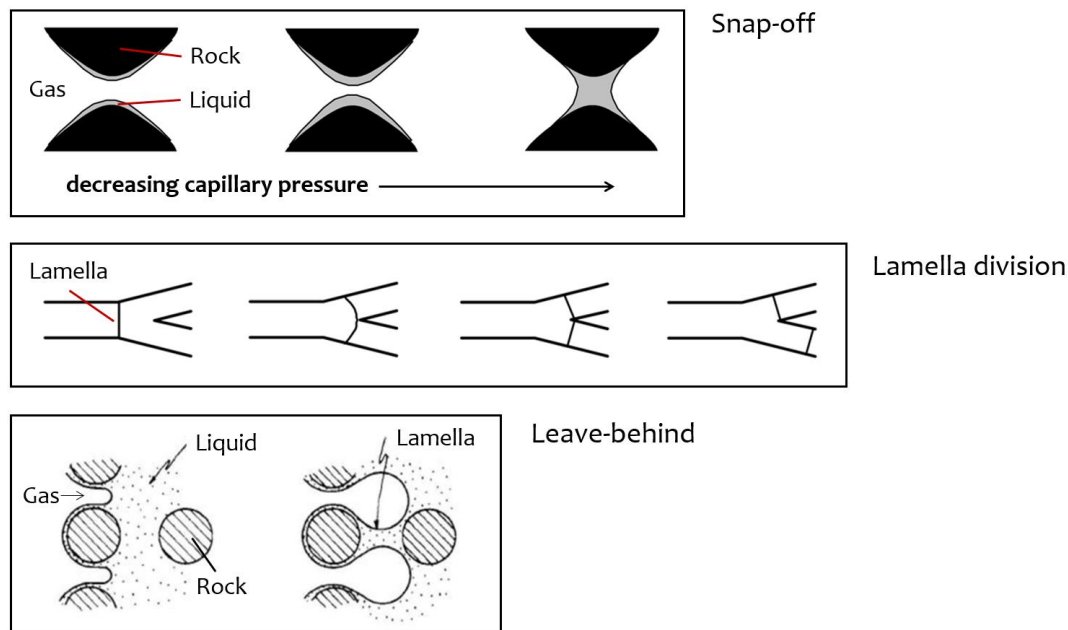


Figure 1.2. Schematic of foam generation by snap-off (Rossen, 2003), lamella division (Chen et al., 2006), and leave-behind (Ransohoff and Radke, 1988).

Foam is a non-Newtonian fluid and exhibits low- and high-quality flow regimes (Osterloh and Jante, 1992; Cheng et al., 2000; Alvarez et al., 2001). In foam, foam quality is defined as the ratio of gas volumetric flow rate to the total rate. Apparent viscosity is used to quantify the strength of the foam; it is the viscosity calculated from Darcy's law assuming that foam is a single-phase fluid. In the low-quality regime, the apparent viscosity of foam is controlled by gas superficial velocity and it increases as foam quality increases. Foam displays shear-thinning rheology in this regime. In the high-quality regime above the critical foam quality, the limiting capillary pressure is reached and foam becomes unstable. Apparent viscosity in this regime is controlled by liquid superficial velocity and it decreases as foam quality increases.

1.4 Foam injection in NFRs

1.4.1 Foam pilots in NFRs

Foam pilots have been implemented in NFRs in the past three decades. By building up a viscous pressure gradient in fractures, foam can divert the flow of gas into the matrix, hence delaying gas breakthrough, reducing gas/oil ratio, and improving oil production (Kovscek et al., 1995; Farajzadeh et al., 2010; Haugen et al., 2014). Friedmaan et al. (1997) reported a foam pilot in the Rangely field that was characterized as a sand unit with hydraulic fractures, natural fracture networks, reservoir heterogeneity, and injection/production imbalance. They found that the gelled foam improved volumetric sweep, reduced CO₂ recycling, and increased oil production at a lower cost than traditional polymer gel. Ocampo et al. (2014) presented two successful foam EOR field pilots in the naturally fractured Cupiagua in Recetor field. They used the technique of gas tracer to study foam and confirmed gas diversion deep in the reservoir and improvement in sweep efficiency. They found that foam mitigated gas recycling and increased oil/condensate recovery. In the tight, fractured reservoir in Woodbine, Katiyar et al. (2019)

reported an immiscible hydrocarbon foam pilot. The injection strategy of SAG was adopted. They observed an increased oil production rate and an increased gas utilization ratio. Foam was also successfully implemented in the naturally fractured gas-condensate Piedemonte field (Ocampo et al., 2020). By dispersing surfactant solution in the hydrocarbon gas, a delayed gas breakthrough and a reduction of gas/oil ratio were achieved.

1.4.2 Foam in model fractures

To enrich the understanding of foam behavior and its implications in NFRs, experimental studies of foam have been conducted in model fractures with various geometries since the 1990s. Kovscek et al. (1995) studied foam in two transparent epoxy replicas of natural rock fractures with hydraulic apertures of 30 and 100 μm , respectively. They found that foam reduced gas mobility by a factor of 100 to 540 at foam qualities from 0.6 to 0.99. They also reported in-situ foam generation by capillary snap-off in the model fractures, as in geological porous media.

Yan et al. (2006) conducted foam experiments in glass-plate model fractures with different geometries. Their model fractures each consisted of either one or two parallel side-by-side smooth slits. The apertures of single-slit fractures ranged from 100 to 300 μm , and the double-slit fractures had an aperture combination of 100/200 or 50/150 μm . They pre-generated foam at superficial velocities from 0.001 to 0.2 m/s and foam qualities from 0 to 0.9. They found that foam greatly improved the sweep efficiency in the double-slit fracture system.

Steinsbo et al. (2015) performed miscible CO_2 and CO_2 foam experiments in two fracture samples. The fractures were made of cores that were sawn in two halves and then assembled using spacers between the halves to maintain a uniform aperture of 1000 μm . They pre-generated foam at superficial velocities of 0.0334 to 0.6 mm/s and foam qualities of 0.8 and 0.9. They concluded that foam increased oil-production rate and the ultimate recovery in all their experiments due to the increase in viscosity of the flow in the fracture, leading to more CO_2 diversion into the matrix.

Fernø et al. (2016) conducted foam experiments in a fracture network. They found that foam was generated in situ in the fracture network during SAG and co-injection of gas and surfactant solution over a range of gas fractional flows. They reported gas-mobility-reduction factors from 200 to more than 1000. Foam significantly improved sweep and delayed gas breakthrough compared to gas injection.

AlQuaimi and Rossen (2018b) studied foam in five glass model fractures (length \times width: 400 \times 100 mm) with different roughness. By using a microscope, they investigated foam generation and propagation in the fractures. They identified capillary snap-off and lamella division as the main mechanisms of foam generation in their model fractures. Slit-shaped throats with a large width/height ratio were favorable for the snap-off of small bubbles that were often smaller than the pores. Foam generation by lamella division took place at high gas fractional flows when a lamella divided as it encountered a split in the flow path. In two of their model fractures, they observed low- and high-quality flow regimes as in porous media. In the low-quality regime, bubbles had a smaller size than the pores, contrary to what is believed the case in unfractured porous media (Alvarez et al., 2001). In the high-quality regime, the

foam was governed not by coalescence above the limiting capillary pressure, as in unfractured porous media (Khatib et al., 1988), but by fluctuations in foam generation.

Brattekkås et al. (2020) studied foam by co-injecting surfactant solution and gas through rough-walled, fractured marble rocks that mimicked natural fracture systems in carbonate reservoirs. The marble matrix was impermeable and flow was isolated within the fracture networks. By measuring apparent viscosity, they confirmed in-situ foam generation and identified two foam quality regimes (high-quality and low-quality regimes) in fractures, as in porous media.

1.4.3 Foam in microfluidic models

In recent years, a microfluidic device, a network of channels and pillars with uniform depth and widths of tens to hundreds of microns, has become increasingly useful in the research field of foam EOR (Kovscek et al. 2007; Marchalot et al. 2008; Conn 2015). It provides possibilities to replicate some aspects of the complex geometry of geological porous media, and its transparency allows direct observation of foam behavior at the pore scale. Gauteplass et al. (2015) carried out foam experiments in 5×5 cm etched-silicone micromodels that represented fracture systems. They pre-generated foam at a superficial velocity of 0.9 mm/s and foam qualities from 0.75 to 0.95. By studying lamella movement in the interior of the pore bodies and at permeability discontinuities, they identified snap-off as the main mechanism for in-situ foam generation in their models. Jones et al. (2018a) studied gas trapping in a microfluidic model and reported a strong response of trapped-gas fraction to velocity variations. The fraction of trapped gas increased from 12% to 63% as superficial velocity dropped from 400 to 50 mm/s. They argued that at lower velocities bubbles had a higher probability to coarsen to pore size, and in the process, more effectively blocking individual pores and increasing the trapped-gas fraction.

1.4.4 Challenges to foam in NFRs

Despite the field successes in NFRs and the major progress in theoretical understanding, foam application in NFRs is still far less understood than in unfractured porous media. In NFRs, fractures are created by earth stresses. They have different conductivity, aperture and roughness (van Golf-Racht 1982). Usually associated with folds, natural fractures can be meters tall and tens of meters long. In most NFRs, principle stresses (in parallel with the horizontal plane) are smaller than overburden pressure. Thus, fractures are typically inclined with a dip angle larger than 60° or even vertical (Stearns and Friedman 1972). All these complexities of fractures can significantly affect flow dynamics in NFRs.

During foam injection in unfractured porous media, much gas is trapped in-situ in the pore space, which greatly reduces gas relative permeability (Tang and Kovscek 2006; Nguyen et al., 2009; Balan et al. 2011). It has been reported that in porous media above 80% to almost 100% of gas is trapped. Gas trapping is the key mechanism to reduce the mobility of gas in porous media. However, it is not clear how gas trapping behaves in fractures. In addition, to achieve an optimized mobility control, the stability of foam must be maintained while it propagates deep into the reservoir. However, at the pore scale, foam coalescence can take place due to different mechanisms, including capillary coalescence and diffusive coarsening. How these mechanisms affect foam behavior in fractures is not yet known.

1.5 Objectives and scope of this dissertation

This dissertation investigates foam behavior in fractures with different roughness and hydraulic apertures. We build four glass model fractures (Models A, B, C and D); each represents a single open geological fracture. Model A has a roughened plate with a regular roughness. Models B, C and D, with increasing hydraulic apertures, use the same roughened plate with an irregular roughness. We characterize the fracture geometry and use a high-speed camera to quantify foam properties and their relation with foam behavior. In particular, we calculate water saturation and capillary pressure in the model and study diffusive coarsening, gas trapping, and gravity effects on foam in fractures. This dissertation comprises seven chapters.

In **Chapter 1**, we provide an introduction to NFRs, gas injection in NFRs, foam injection, and foam injection in NFRs and its challenges. We also list the objectives and scope of this dissertation. In **Chapter 2**, we show the experimental setup and materials. We elaborate on the procedures of creating model fractures and approaches to characterize fracture geometries. We also explain how to use ImageJ software to analyze different properties of the foam. In **Chapter 3**, we study the spatial structure of foam in the two model fractures (Models A and B) with different roughness and hydraulic apertures. We report a novel technique to estimate water saturation and capillary pressure of foam in the model fractures. This technique provides insights for studies of foam in NFRs with complex geometry, where measuring such foam properties is challenging. In **Chapter 4**, we repeat and extend the experiments of Chapter 3 to investigate how foam evolves during coarsening by gas diffusion in model fractures (Models A and B). During coarsening, foam bubbles restructure and lamellae relocate to achieve their minimum surface area. We estimate the height of lamellae through which gas can diffuse, and discuss how it relates to coarsening behavior. In **Chapter 5**, we investigate gas trapping in one model fracture (Model B) and how it affects foam behavior. We compare gas trapping in model fractures and unfractured porous media and explain the mechanisms using a modified capillary number (AlQuaimi and Rossen, 2018a) which takes fracture geometries into account. In **Chapter 6**, we investigate the effects of gravity on foam in the three model fractures (Models B, C and D) with the same roughness, but increasing hydraulic apertures. We also discuss how hydraulic aperture affects foam generation and gravity segregation in fractures. In **Chapter 7**, we summarize the findings of this dissertation. In addition, we discuss aspects of foam in fractures that deserve further study.

2 Methodologies

2.1 Experimental setup and materials

Figure 2.1 shows the experimental setup. We use a dual-cylinder pulse-free pump (VINDUM Engineering, INC., Model VP1-12 K™, range: 0 to 28 ml/min) to inject liquids, and a mass-flow controller (Bronkhorst Nederland B.V., F-230 M™, range: 0.19 to 10 ml/min) to inject gas. A mixing tee with a frit filter inside (Upchurch Scientific, PEEK™, UHMWPE frit, mesh size: 10 μm) is installed upstream of the inlet of the fracture to pre-generate foam. Seven absolute-pressure transducers (DEMO MPXH6400A, range: 4 bar, accuracy: ± 10 mbar) are mounted at different locations along the model fracture to measure the pressure. A computer regulates the injection rates of the liquid and gas, and record pressure measurements, from which pressure gradient can also be computed.

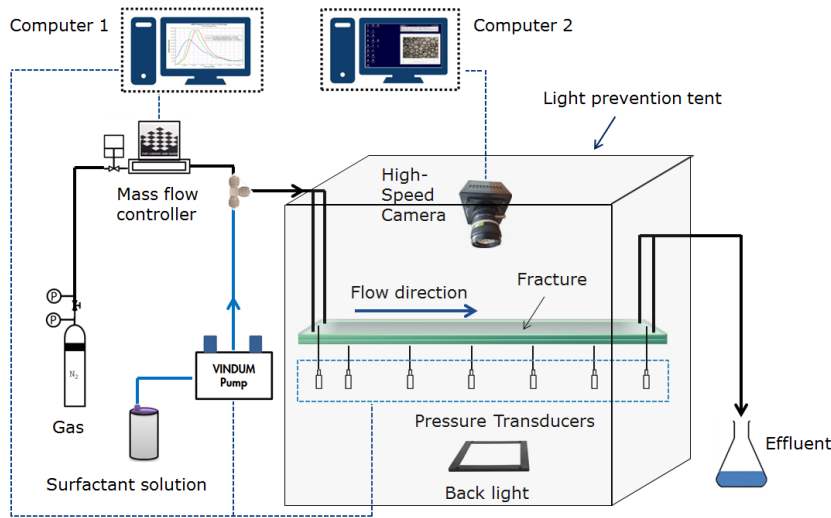


Figure 2.1. Experimental setup.

The centerpiece of the setup is a glass model that represents a single open geological fracture. We use a high-speed high-resolution camera (Photron Fastcam UX50™, up to 160,000 fps) installed perpendicular to the fracture plane to visualize foam inside the model fracture and record its images. A chip back-light device (VAL LED lighting, VL-CB-CL), mounted at the other side of the fracture opposite the camera, provides high-parallelism white light for the camera. A computer operates the camera and handles the image acquisition. The entire setup is placed inside a black tent to avoid scattered light to improve the imaging quality.

In all experiments, we inject a solution of 1 wt% AOS C14-16 surfactant (Stepan® BIO-TERGE AS-40 KSB, active content: 39%, molecular weight: 324 g/mol) with zero salinity and nitrogen (Linde Gas Benelux B.V., Purity $\geq 99.999\%$) to create foam. Additional dyes have not been used. The surface tension γ_s of the surfactant solution at 20°C is 32.2 mN/m, measured by using a tensiometer (KSV Sigma™). Demineralized water (Elga Veolia Labwater™) is used to make the surfactant solution and clean the model fractures. It is also used in experiments to measure the hydraulic aperture of model fractures.

2.2 Glass model fractures

2.2.1 Manufacturing procedures of model fractures

AlQuaimi and Rossen (2018b) used roughened glass plates to build a variety of model fractures to study foam. Their models represent geological fractures and also easily facilitate the imaging study of in-situ foam. In this dissertation, using similar methods, we create in total four model fractures, Models A, B, C and D, with the same dimension $1 \times 0.15 \times 0.04$ m (length \times width \times thickness), but different roughness and hydraulic apertures. Each model consists of two 2-cm-thick glass plates (Hijman Glas B.V., the Netherlands). The top glass plate is smooth and the bottom plate is roughened on the side facing the top plate. The roughness of the bottom roughened plate is created by moulding during the manufacturing process. The glass plates are strongly water-wet and stress-free to avoid optical effects.

Model A has a roughness in a regular pattern. Models B, C and D have the same roughness in an irregular pattern, but different hydraulic apertures. To create either Model A or Model B, we place the smooth plate on top of the roughened plate and glue them along edges using silicone rubber (ResinTechnology B.V., SR1-40B). As shown in Fig. 2.2, the model is then housed in an aluminum clamping frame. Due to a small penetration of glue along the edges, the two plates of either Model A or Model B are not directly against each other. The gap between the two plates represents a geological fracture with variable aperture. Along the model fractures, we drill in total 11 holes through the roughened plates for foam injection and discharge, and for linking to the pressure transducers. Each model fracture is thus divided into six sections of 18 cm length, except for section 1, which is 10 cm long. Two troughs (length \times width \times depth: $12 \times 2 \times 0.04$ cm) are milled in the roughened plates. The one at the inlet facilitates a uniform foam injection into the fracture along its width. The one at the end of the model fracture prevents convergence of foam flow toward the outlet. We disassemble Model B, after we perform all experiments on this model fracture, and use the same irregular-roughened plate to create Model C, using the same procedures. We also use the same irregular-roughened plate to create Model D after completing experiments on Model C. Models B, C and D thus share the same roughness pattern. However, in Models C and D, 3-mm-wide strips of copper foil (with the thickness of $25 \mu\text{m}$, $75 \mu\text{m}$, respectively) are placed along the edges between the two plates, to increase the apertures of the two model fractures.

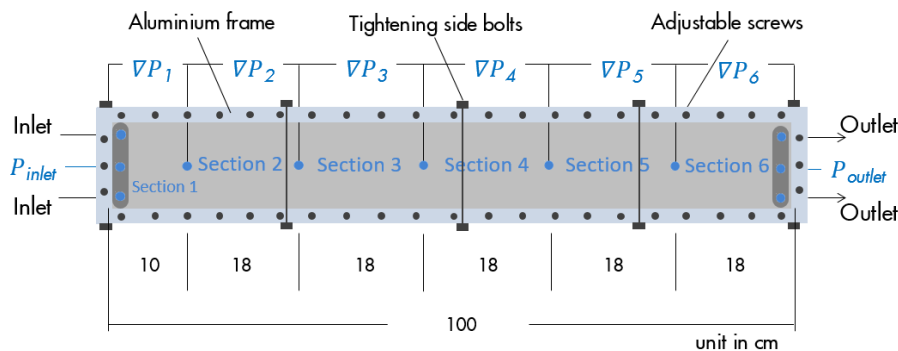


Figure 2.2. Assembly of the model fracture (top view of the horizontally-placed fracture).

2.2.2 Roughness and hydraulic aperture of model fractures

Figure 2.3 shows the relative height of the regular-roughened plate of Model A. The mean height value is $54 \mu\text{m}$. The area roughness parameters, arithmetical mean deviation and root mean square of the height, are 29 and $33 \mu\text{m}$, respectively.

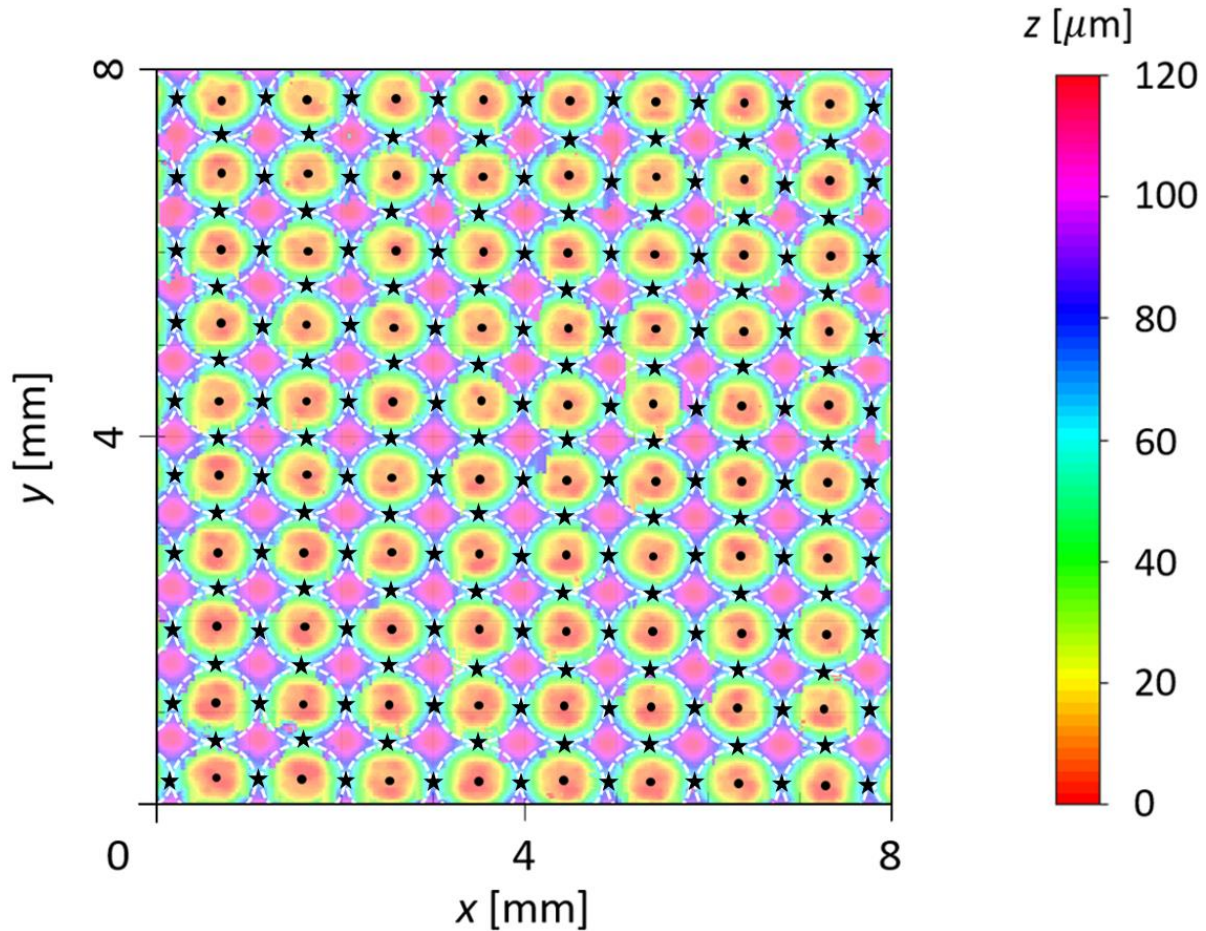


Figure 2.3. Relative height of the roughened plate of Model A (regular pattern): resolution, 960×960 ; pixel size, $69 \mu\text{m}^2$. The minimum height is set to $0 \mu\text{m}$. Black stars are saddle points on the roughened plate, and black dots are local minima in height. The height data are profiled using a digital microscope (Keyence, VHX-7000™). White dashed lines outline the boundaries of pore bodies (to be explained in Subsection 2.2.4).

Figure 2.4 shows the relative height of the irregular-roughened plate used for Models B, C and D. The mean height value is $95 \mu\text{m}$. Arithmetical mean deviation and root mean square of the height are 38 and $45 \mu\text{m}$, respectively. Although the roughness of this plate is irregular, a 20×20 mm profile of height is statistically representative along the whole plate.

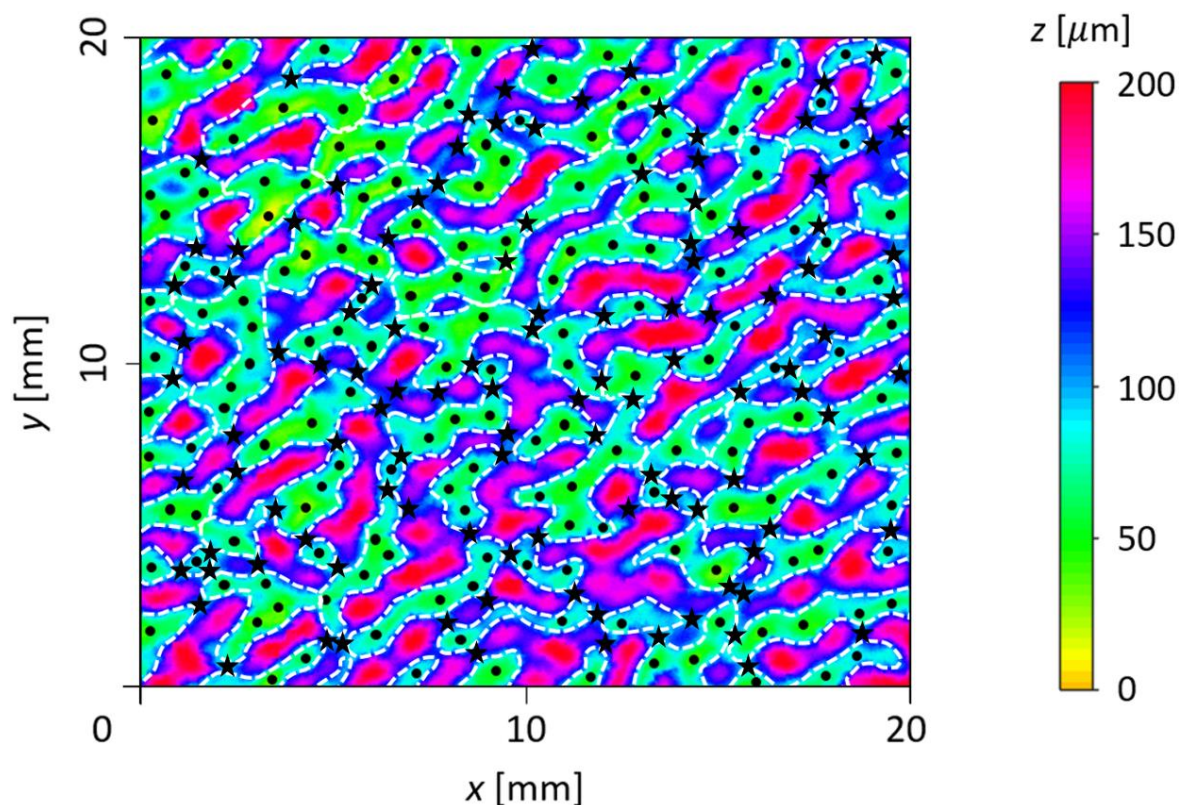


Figure 2.4. Relative height of the roughened plate used for Models B, C, and D (irregular pattern): resolution, 2860×2860 ; pixel size, $49 \mu\text{m}^2$. The minimum height is set to $0 \mu\text{m}$. Black stars are saddle points on the roughened plate, and black dots are local minima in height. The height data are profiled using a digital microscope (Keyence, VHX-7000TM). White dashed lines outline the boundaries of pore bodies (to be explained in Subsection 2.2.4).

As shown in Fig. 2.5, with the smooth plate on top of the roughened plate, each model fracture provides a slit-like channel with variation in aperture for foam flow.

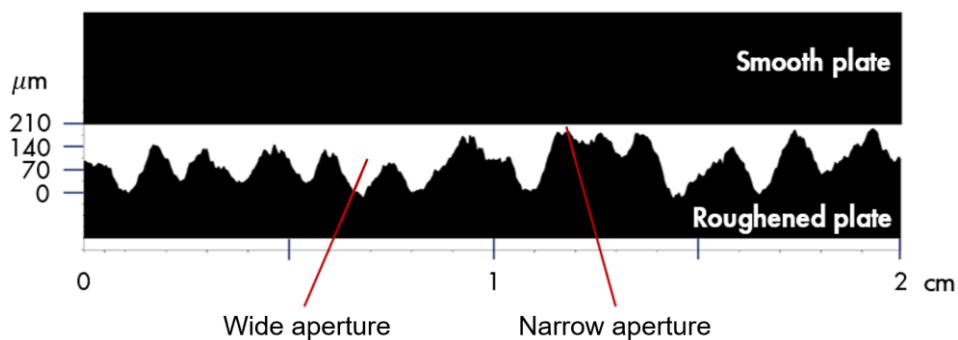


Figure 2.5. Cross-section view of Model B with irregular roughness. The vertical height scale is greatly exaggerated.

Before conducting any foam experiments, we measure hydraulic aperture d_H of the model fractures, by injecting demineralized water through the pre-vacuumed fractures at stepwise-increasing volumetric rates q_w . After water flow at each injection rate reaches steady-state, we record its pressure gradient ∇P_w . A regression of pressure gradient against the injection rate determines the hydraulic aperture d_H (Witherspoon et al., 1980):

$$|\nabla P_w| = 12 q_w \frac{1}{w d_H^3} \mu_w \quad (2.1)$$

where w is the width of the model fracture, and μ_w is water viscosity. The hydraulic apertures of Models A, B, C and D obtained from Eq. 2.1 are 46, 78, 98 and 128 μm , respectively.

The definition of hydraulic aperture approximates the model fracture as a smooth slit. It is then related to the permeability of the model fracture, k_f , by (Tsang 1992):

$$k_f = \frac{d_H^2}{12} \quad (2.2)$$

For our four model fractures, k_f values are 176, 507, 800, 1365 darcy, respectively.

In addition, we measure the fracture volume of the models by injecting demineralized water into the pre-vacuumed models while closing the outlet valve. We stop the injection once the models are fully saturated with water, without remaining gas. The volume of water injected by the pump to fill the fracture is considered to be the fracture volume. The measured volume of Models A, B, C and D are 9.1, 14.2, 16.9 and 20.8 mL, respectively.

The bending test of the fracture plates is also performed by pressurizing the containing water up to 100 kPa. A micrometer (Peacock, G-6C, full scale: 1 mm, precision: 1 μm) is mounted on the model to measure the bending. In this dissertation, all four model fractures are 4 cm thick. We house the fractures in aluminum frames. The maximum bending is 4 μm at the centroid of the fractures.

2.2.3 Characterization of fracture geometries

For each of our four models, the smooth plate does not directly contact the roughened plate, either due to the small penetration of glue (Models A and B), or because copper foils are placed between the two plates (Models C and D). There is thus an extra gap between the two plates. We estimate the gap d' by comparing the fracture volume V_f determined from the volume of water required to fill the fracture, and the integral volume derived from the roughness distribution V_r , which is given by Eq. 2.3:

$$V_r = \frac{L w}{A_p} \int (h_{max} - h_i) dA_i \quad (2.3)$$

where L is the length of the model fracture, and w is the width, A_p is the size of the height profile (Fig. 2.3 for Model A, and Fig. 2.4 for Models B, C and D), h_{max} is the maxima of the height dataset, h_i is the height at each pixel, and A_i is the size of each pixel. The extra gap between the two plates of the model fractures is estimated by Eq. 2.4:

$$d' = \frac{V_f - V_r}{L w} \quad (2.4)$$

d' of our four model fractures obtained from Eqs. 2.3 and 2.4 are 7, 11, 23 and 67 μm , respectively. We combine d' and $(h_{max} - h_i)$ to create the aperture distribution of each model fracture. Figure 2.6 shows the height histogram of the roughened plate and aperture distribution for the four model fractures.

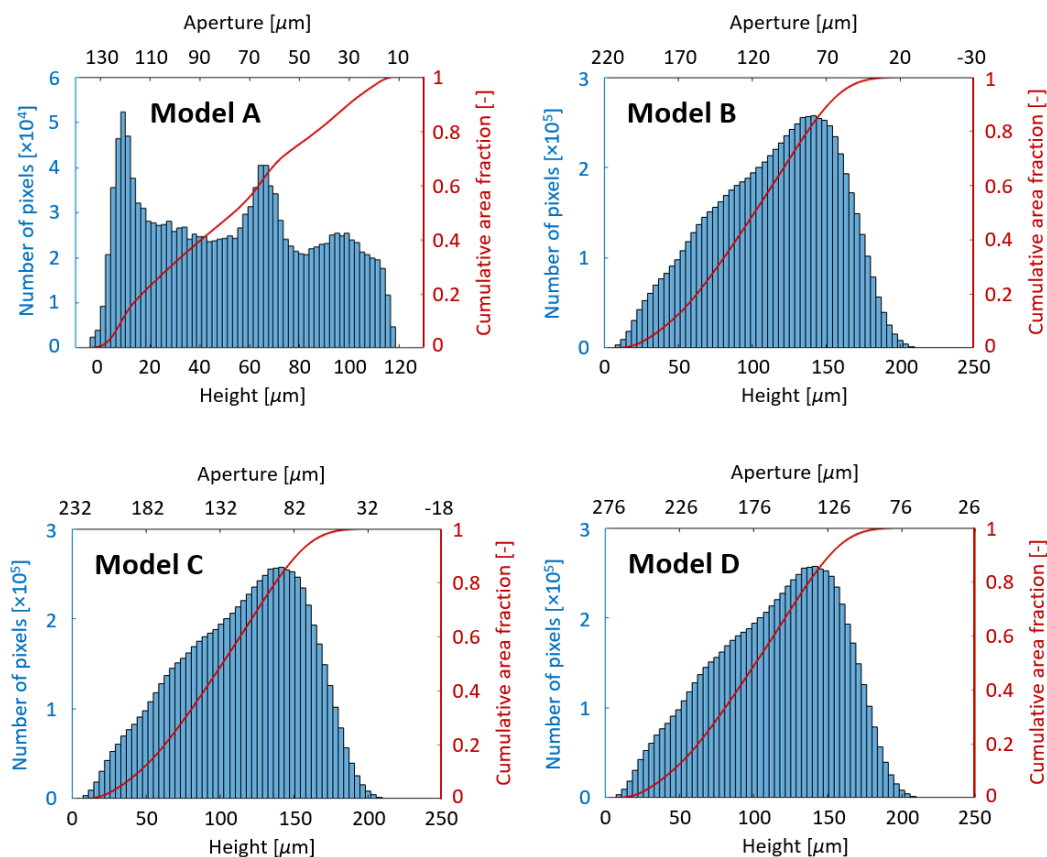


Figure 2.6. Height histogram of the roughened plate and aperture distribution for the four model fractures. Red curved lines are cumulative area fractions based on height histogram.

With local hills (maxima of height) and valleys (minima of height) on the roughened plates, the distribution of aperture of the four models can be represented as a 2D network of pore bodies and pore throats. Thus, with pore bodies and throats, the model fractures are comparable to the concept of microfluidic porous media. To characterize the geometry of the model fractures, as shown in Figs. 2.3 and 2.4, we define pore bodies centered on local minima of height on the roughened plate, and pore throats, which connect pore bodies, at saddle points between pore bodies. We measure the heights of these local minima and saddle points and convert them to apertures using aperture distribution. We then average apertures at local minima to estimate typical aperture of pore bodies and average apertures at saddle points to estimate typical aperture of pore throats. We measure the distance between positions of increasing height on either side of a saddle point as the typical width of the pore throat at that saddle point. The white dashed lines in Figs. 2.3 and 2.4 outline the boundaries of what we define as pore bodies. In Model A, the definition of pore bodies is unambiguous. Each pore body has one local minimum of height and is connected to the other four pore bodies through pore throats. In Models B, C and D, the definition of pore bodies is less clear-cut: there may be multiple local minima (with only slightly different heights) for each pore body on the irregular-roughened plate. We consider these to represent one pore body. Table 2.1 shows the spatial properties of the four model fractures. The ratio of throat aperture to body aperture, aspect ratio (aperture to width) of the pore throat, and pore density (number of pore bodies per unit area of the roughened plate) are also presented.

Fracture	Roughness	Hydraulic aperture, $d_H, \mu\text{m}$	Permeability of fracture, k_f, Darcy	Fracture volume, V_f, mL	Typical pore throat aperture, $d_t, \mu\text{m}$	Typical pore body aperture, $d_b, \mu\text{m}$	Typical pore throat width, $w_t, \mu\text{m}$	Ratio of throat aperture to body aperture, d_t/d_b	Aspect ratio of pore throat, d_t/w_t	Pore density / cm^2
Model A	Regular	46	176	9.1	55	119	274	0.46	0.20	149
Model B	Irregular	78	507	14.2	92	174	762	0.53	0.12	17
Model C	Irregular	98	800	16.9	110	192	762	0.57	0.14	17
Model D	Irregular	128	1365	20.8	136	218	762	0.62	0.18	17

Table 2.1. Spatial properties of the four model fractures.

2.3 General procedure of experiments

From Chapters 3 to 6, we report the results of different foam experiments in model fractures and their implications. Before each foam experiment, we clean the model fracture thoroughly by injecting 20 fracture pore volume of demineralized water, then vacuum and fully saturate the fracture with surfactant solution. In all experiments, we pre-generate foam by injecting surfactant solution and gas through the mixing tee with an inside-mounted frit filter (mesh size: 10 μm) at specific foam qualities and interstitial velocities. The designed velocities ensure that foam reaches a stable pressure gradient, and they are not great enough to compromise the safety of our setup with glass model fractures. Foam quality and interstitial velocity are corrected based on the pressure at the middle of the fracture. The pre-generated foam then flows into the model fracture. The pre-generation, combined with considerable foam coarsening by gas diffusion between the mixing tee and the inlet of the fracture, ensures that gas enters the fracture as relatively large bubbles instead of slugs. In all our experiments, there is no back-pressure at the outlet of the fracture. All experiments are conducted at 20°C and atmospheric pressure.

2.4 Image analysis

We investigate foam at different locations in the model fractures and record the images using a high-speed camera. We use ImageJ software (Ferreira and Rasband, 2012) to process raw images and calculate the properties of the foam. In all four model fractures, we observe only monolayer foam, with bubbles extending from top to bottom plates. Plateau borders form where lamellae meet the glass plates above and below. Figure 2.7 shows examples of raw and processed images of steady-state foam at a location 73 cm from the fracture inlet in Models A and B. For each foam image, we distinguish the water and gas phases in the foam by tuning the threshold of the grey values of pixels. Gas bubbles and lamellae are thus identified in binary foam images. We quantify foam texture by measuring bubble density (number of bubbles per unit area of the image), bubble size (2D average bubble area) and polydispersivity (ratio of standard deviation to average bubble size), and gas area fraction. Unlike microfluidics with uniform depth of etching, our model fractures have a variation of aperture, with the presence of hills and valleys on the roughened plates (Figs. 2.3 and 2.4). As a result, there are local accumulations of water (water zones) that occupy locations of narrow aperture in the model fractures, governed by capillarity. We use ImageJ to calculate area fraction of these water zones and total length of lamellae in the image.

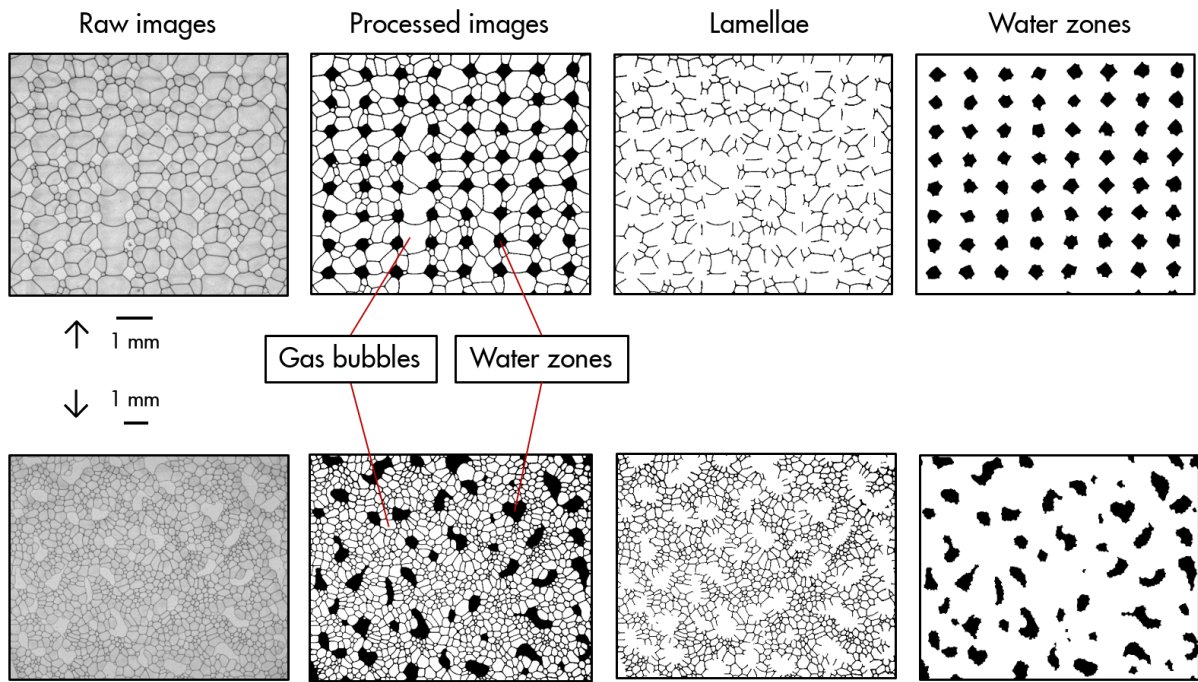


Figure 2.7. Raw and processed images of steady-state foam in Model A (top, image size: 7.8×6.8 mm), and B (bottom, image size: 12.3×9.8 mm). Water is shown in black, gas in white. Water zones occupy locations with narrow aperture in the model fractures.

3 Water Saturation and Capillary Pressure of Foam in Model Fractures¹

3.1 Introduction

In the laboratory, X-ray computed tomography (CT) is commonly used to evaluate the performance of foam in unfractured core plugs (Tang et al., 2019; Gong et al., 2020). A greater pressure gradient indicates finer-texture foam with greater gas mobility control. Water saturation is mapped at different times of the foam process to study foam behavior. However, foam properties such as bubble size and capillary pressure are much more difficult to measure. In recent years, microfluidic models have gained much attention because they easily facilitate the imaging study of in-situ foam. However, it is still challenging to estimate capillary pressure, in a model with a uniform depth of etching.

In this chapter, we conduct experiments in Models A and B to study foam texture and present a novel technique to estimate water saturation and capillary pressure. Model A has a regular roughness (Fig. 2.3), with a hydraulic aperture of 46 μm . Model B has an irregular roughness (Fig. 2.4), with a hydraulic aperture of 78 μm . Unlike microfluidics with uniform depth of etching, our model fractures each has a variation of aperture. We first describe the experiments. We then estimate the local aperture of water-gas interfaces in the model fractures by image analysis. We afterward estimate water volume in the fractures and present results of water saturation and capillary pressure of foam in the two model fractures. We end with a discussion on the uncertainty of our technique.

3.2 Experiments and image analysis

In this chapter, we pre-generate foam through the mixing tee at foam quality 0.9 and total interstitial velocity of 1.2 mm/s and 2 mm/s for Models A and B, respectively. The pre-generated foam is then injected into the horizontally-placed fracture. Despite considerable foam coarsening by diffusion between the mixing tee and the inlet of the fracture, the pre-generation step ensures that gas enters the fracture as relatively large bubbles instead of gas slugs. Within the model fracture, we have observed that foam is further refined during propagation due to in-situ bubble generation. After foam flow achieves steady-state, we

¹ This Chapter is based on Li, K., Wolf, K. H. A., and Rossen, W. R. 2021. A Novel Technique to Estimate Water Saturation and Capillary Pressure of Foam in Model Fractures. *Colloids and Surfaces A: Physicochemical and Engineering Aspects*. <https://doi.org/10.1016/j.colsurfa.2021.127800>.

maintain the injection for at least 1.5 hr, and then close the inlet and outlet valves of the fracture. The model fracture is then shut in for 24 hr at 20°C.

After shut-in, water and gas in foam flow along the model fracture to equalize pressure. At the beginning of the shut-in period, foam continues to flow, governed by a residual pressure gradient. Once this pressure gradient drops below a value that cannot compete with the yield stress of the foam, foam mostly stops flowing (0.08 and 0.10 hr after the shut-in of Models A and B, respectively) and starts to coarsen due to diffusion between bubbles. During coarsening, trains of bubbles occasionally flow in short bursts along separate pathways from outlet toward inlet. This evidently results from a pressure gradient from outlet toward inlet due to a small leak in the tubing upstream of the models. We also observed rare coalescence (rupture of lamellae) during convection of the bubble trains. However, the bubble texture wasn't much different after those intermittent periods of convection: the occasional convection of bubbles along separate pathways and coalescence of lamellae haven't significantly affected the overall behavior of foam coarsening in our study. In addition, water in foam is transported along our models even during periods with no bubble flow. We study coarsening behavior in Models A and B in detail in Chapter 4.

In this chapter, to estimate water saturation and capillary pressure of foam, we investigate foam at a fixed location 73 cm from fracture inlet (Fig. 3.1) and record the images of foam for 24 hr at 4 frames per minute. We use ImageJ software to process raw foam images and measure gas area fraction S'_g .

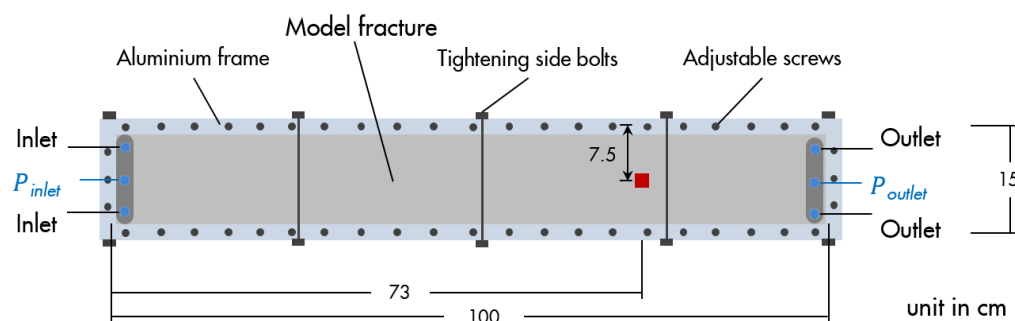


Figure 3.1. Horizontally-placed model fracture mounted in the aluminum clamping frame (top view). The red square indicates the location where foam is studied in this chapter.

Figure 3.2 shows processed images of foam at the location 73 cm from the fracture inlet at different times of the experiments in Models A and B. Our model fractures have a variation of aperture, unlike microfluidics with uniform depth of etching. Water accumulates in locations with narrow aperture within the model fractures, governed by capillarity. We distinguish these water zones and lamellae to calculate water-occupied area fraction, and then skeletonize all lamellae in the image to sum up their lengths.

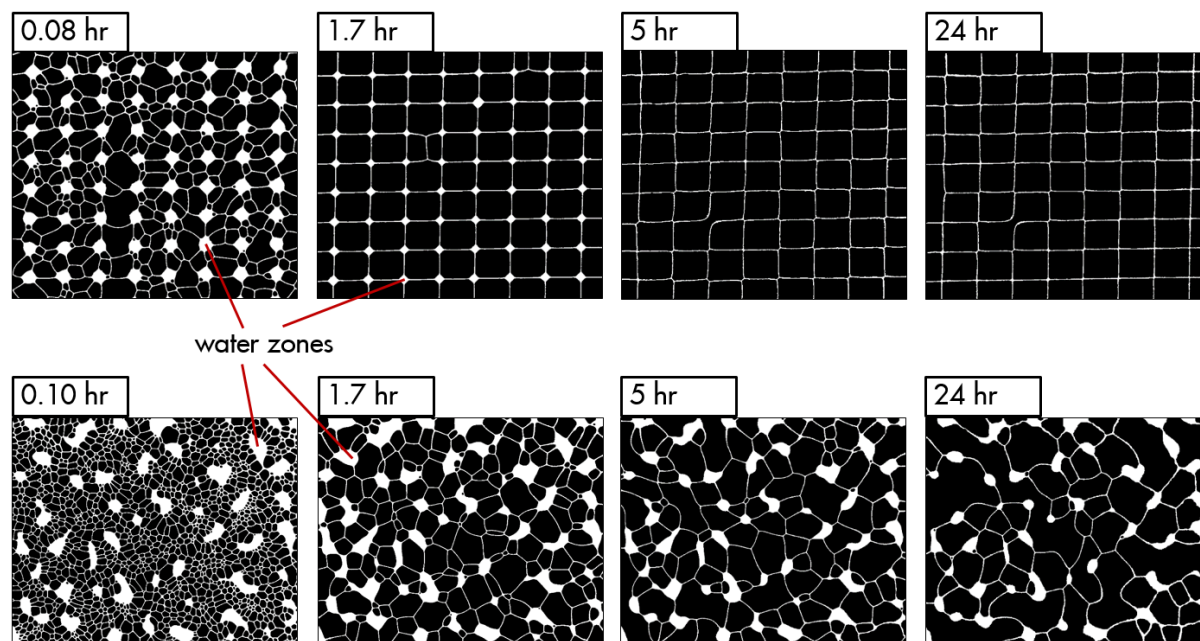


Figure 3.2. Processed images of foam 73 cm from the fracture inlet at different times of the experiments in Model A (top, image size: 7.8×6.8 mm) and B (bottom, image size: 12.3×9.8 mm). Water is shown in white, gas in black. Water zones occupy locations with narrow aperture in the model fracture.

3.3 Local aperture at water-gas interfaces

We relate aperture distribution in the model fractures (Fig. 2.6) and water-occupied area fraction to estimate the local aperture d_a , where water-gas interfaces locate at the edge of the water-occupied areas (water zones). In model fractures, the capillary pressure in foam tends to equalize during the period of coarsening. In foam, the Plateau borders form an interconnected network for water to redistribute and capillary pressure to equalize, at least within the region of the image. We assume that one interface would have the same local aperture d_a as others within the area of an image due to nearly uniform capillary pressure in that area of the fracture. We use the value of local aperture d_a of water-gas interfaces to estimate capillary pressure, and from that the radius of Plateau borders and the height of lamellae between the Plateau borders.

3.4 Water saturation and capillary pressure of foam

In this dissertation, we assume that contact angle θ is 0, as water strongly wets the glass model fractures. Figure 3.3 shows a schematic of foam in Model A for a case where bubbles each fill a pore body. The gap between the plates is much less than the radius of curvature of the water-gas interface as viewed from above (Fig. 3.2). All water-gas interfaces are thus close to cylindrical. In our model fractures, water exists in four locations: water zones at narrow aperture, Plateau borders, lamellae, and water films that wet fracture walls above and below.

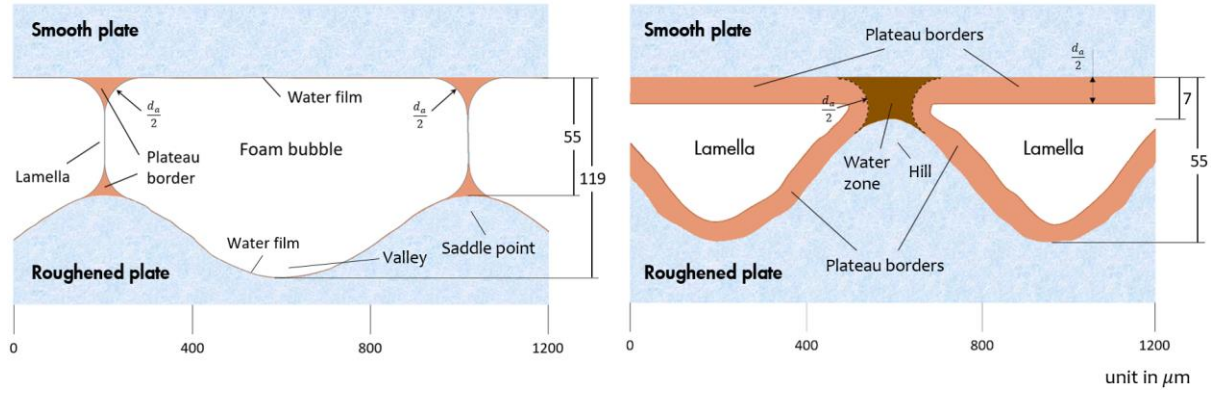


Figure 3.3. Schematic of foam texture in Model A for a case where bubbles each fill a pore body. **Left:** cross-section view of gas bubbles in pore bodies, with lamellae in pore throats. **Right:** perpendicular view of lamellae and Plateau borders located at pore throats and water zone located at the location with narrow aperture. d_a is the local aperture of water-gas interfaces. The vertical scale is greatly exaggerated in both images.

As shown in Fig. 3.3, water zones accumulate in locations with narrow aperture in the model fractures. We thus use the histogram of height on the roughened plates (Fig. 2.6) to relate water-occupied area fraction to the volume of the water zones $V_{water\ zone}$. Figure 3.4 shows the relation for the two model fractures. The calculation of water volume at different locations within the image is based on a defined fracture volume V_f' within the region of the images shown in Fig. 3.2: 1.03 mm^3 and 11.44 mm^3 within a region of 52.9 mm^2 and 120.8 mm^2 for Models A and B, respectively.

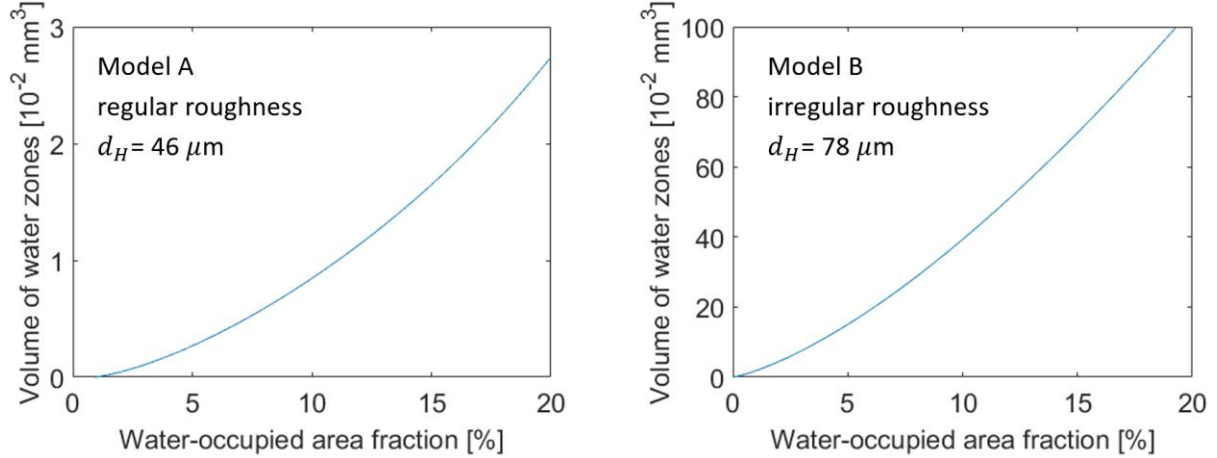


Figure 3.4. Relation of water-occupied area fraction to volume of water zones for Models A (left) and B (right). Volume of water zones is based on a defined fracture volume of 1.03 and 11.44 mm^3 for Models A and B, respectively.

In our model fractures, we observe foam with bubbles extending from top to bottom plates. Plateau borders form where lamellae meet glass plates above and below. Under strongly water-wet conditions, as here, the radius of the Plateau borders is half of the local aperture of water-gas interfaces d_a . The volume of water in Plateau borders is then given by:

$$V_{plateau\ border} = \left(\frac{4 - \pi}{4}\right) d_a^2 L_{lamella} \quad (3.1)$$

where $L_{lamella}$ is the sum of lengths of all lamellae in the image.

A small amount of water exists in sub-microscopic lamellae and water films along the glass plates. We estimate the volume of water in lamellae and water films by:

$$V_{lamella} = L_{lamella} \cdot d_{lamella} \cdot h_{lamella} \quad (3.2)$$

$$V_{water\ film} = 2 S'_g A_{image} d_{film} \quad (3.3)$$

where $d_{lamella}$ and $h_{lamella}$ are the thickness and height of lamella, d_{film} is the thickness of water film, S'_g is the gas area fraction, and A_{image} is the area of the image. Both $d_{lamella}$ and d_{film} depend on the surfactant, salinity and capillary pressure. In this dissertation, we assume both to be 30 nm (Hirasaki, 1991; Bergeron and Radke, 1992). As shown in Fig. 3.3 left, lamellae connect Plateau borders on the smooth plate above and the roughened plate below. In this chapter, we approximate $h_{lamella}$ as $(d_H - d_a)$ at different times of the experiments, where d_H is the hydraulic aperture of the model fracture, and d_a is the local aperture of water-gas interfaces. However, in Chapter 4, estimation of $h_{lamella}$ is more clear-cut when lamellae locate in specific locations in the model fracture at the end of coarsening experiments.

As shown in Fig. 3.2, there are no local water-occupied zones (water zones) at positions of narrow apertures in Model A after 5 hr. It is then difficult to estimate the local aperture of water-gas interfaces, and from that the radius of Plateau borders, water saturation and capillary pressure. It is nevertheless evident that the out-flow water rate is greater than the in-flow water rate at location 73 cm from the inlet of Model A. The water saturation after 5 hr there is at least lower than that at 1.7 hr, with greater capillary pressure.

Figure 3.5 shows water volume in different locations. Water zones and Plateau borders account for almost all water in foam. In both models, during the period of shut-in, if bubbles do not move, the in-flow and out-flow of water must take the paths through Plateau borders and water zones, as they are the only continuous paths for water flow.

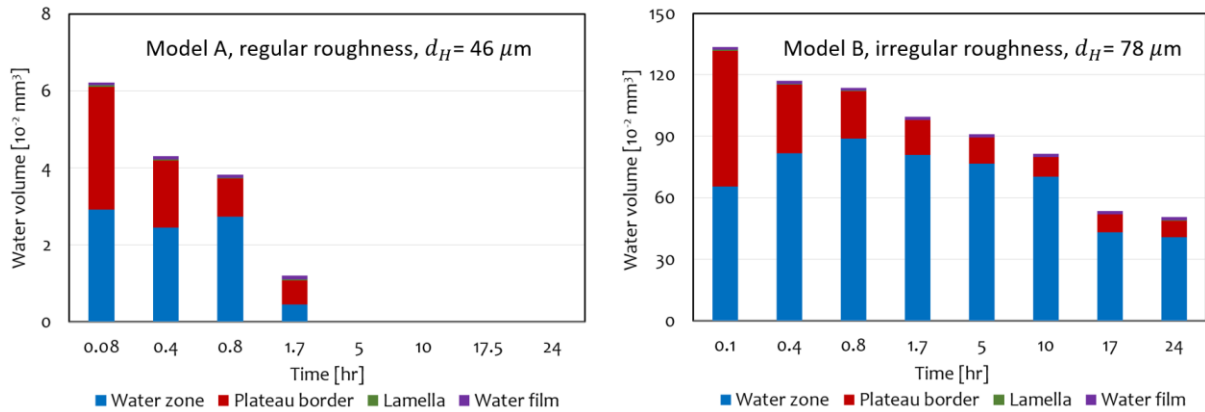


Figure 3.5. Water volume in water zones, Plateau borders, lamellae and water films in Models A (left) and B (right).

We calculate water volume V_w and water saturation S_w by:

$$V_w = V_{water\ zone} + V_{Plateau\ border} + V_{lamella} + V_{water\ film} \quad (3.4)$$

$$S_w = \frac{V_w}{V'_f} \quad (3.5)$$

where V_f' is the fracture volume within the region of the images shown in Fig. 3.2 (1.03 and 11.44 mm³ for Models A and B, respectively).

We estimate capillary pressure of foam P_c at a specific time by:

$$P_c = \frac{2 \gamma_s \cos \theta}{d_a} \quad (3.6)$$

where γ_s is the surface tension of the surfactant solution, θ is the contact angle, and d_a is the local aperture of water-gas interfaces.

Figure 3.6 shows the results of S_w and P_c at different times during the experiments in the two models. In both model fractures, the decrease in water saturation coincides with an increase in capillary pressure, as expected. The decrease in water saturation is due to the small leak upstream of the fracture inlet and consequent upstream flow of water. Compared to Model B, foam in Model A evolves under higher capillary pressure.

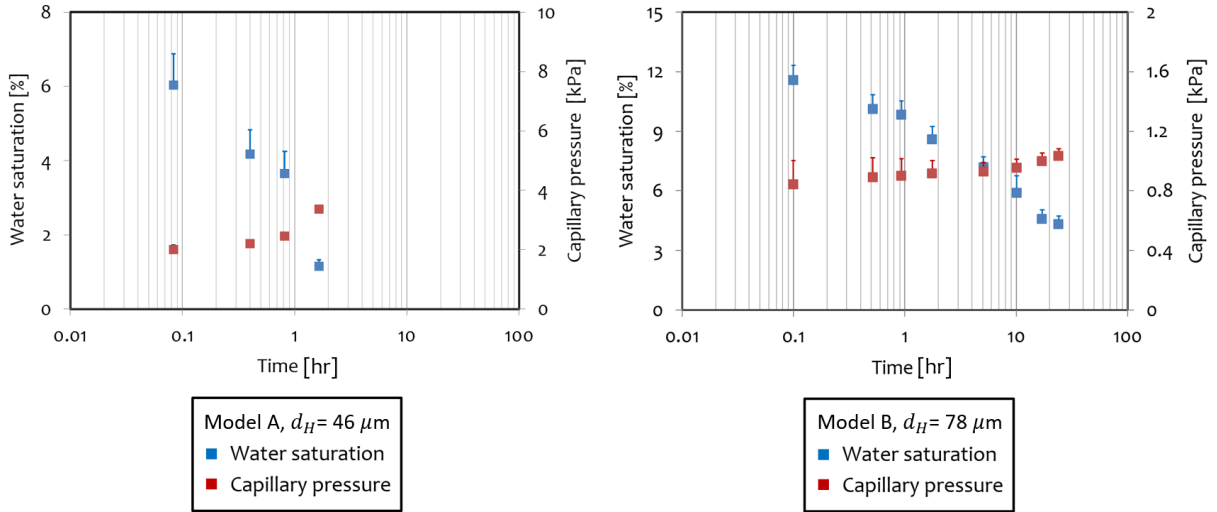


Figure 3.6. Water saturation and capillary pressure of foam in Models A (left) and B (right). The positive error bar on the data reflects the uncertainty of water saturation and capillary pressure estimation. The calculation of the uncertainty is described in the next Section.

In this chapter, by analyzing foam images, we examined foam texture and estimated water saturation and capillary pressure in the model fractures. Table 3.1 presents the results of water volume in different locations, water saturation, and capillary pressure of foam in the two model fractures.

	Time, hr	Aperture at water-gas interfaces, d_a , μm	Water volume in water zones, $V_{\text{water zone}}$, 10^{-2} mm^3	Water volume in Plateau borders, $V_{\text{Plateau border}}$, 10^{-2} mm^3	Water volume in lamellae, V_{lamella} , 10^{-2} mm^3	Water volume in water films, $V_{\text{water film}}$, 10^{-2} mm^3	Total water volume, V_w , 10^{-2} mm^3	Water saturation, S_w , %	Capillary pressure , P_c , kPa
Model A (regular roughness), $d_H = 46\ \mu\text{m}$	0.08	32	2.92	3.18	0.04	0.08	6.23	6.0	2.01
	0.4	29	2.45	1.73	0.03	0.09	4.30	4.2	2.21
	0.8	26	2.74	0.98	0.02	0.09	3.83	3.7	2.46
	1.7	19	0.45	0.63	0.02	0.10	1.20	1.2	3.37
	5								
	10								
	17.5								
24									
Model B (irregular roughness), $d_H = 78\ \mu\text{m}$	0.1	76	65.53	66.15	0.53	1.30	133.52	11.6	0.84
	0.4	72	81.66	33.55	0.30	1.40	116.91	10.1	0.89
	0.8	71	88.75	23.24	0.21	1.43	113.64	9.8	0.90
	1.7	70	80.74	17.01	0.16	1.48	99.39	8.6	0.91
	5	69	71.73	9.69	0.12	1.58	83.13	7.2	0.93
	10	67	61.11	9.21	0.10	1.56	71.98	5.9	0.96
	17	64	43.12	8.74	0.10	1.61	53.57	4.6	1.00
24	62	40.60	8.19	0.10	1.64	50.53	4.3	1.03	

Table 3.1. Results of water volume, water saturation, and capillary pressure in the two model fractures. Data in Model A after 5 hr are not presented, because there are no water zones at locations of narrow apertures and it is then difficult to estimate the local aperture of water-gas interfaces for these calculations.

The estimation of capillary pressure, crucial to our approach, is made possible by the variation of aperture with position in the models. This approach would not work in microfluidic devices with uniform depth of etching. The interconnected network of Plateau borders in foam is also essential to our assumption that water can redistribute, in a foam where bubbles are immobile, to equalize capillary pressure within the region of the images.

3.5 Estimated uncertainty of water saturation and capillary pressure

In this chapter, calculated water volume comprises four locations within the image in the model fractures. To this end, we convert water-occupied area fraction to water volume in water zones (as one of the four locations) using an integral-based correlation (Fig. 3.4). In raw images of foam (Fig. 2.7), water-gas interfaces around water zones appear as lighter boundaries compared to darker Plateau borders that also mark the location of lamellae. Using ImageJ software, we identified water zones to compute water-occupied area fraction. We further related aperture distribution of model fractures to water-occupied area fraction to estimate the local aperture d_a at water-gas interfaces, by which we estimated capillary pressure of foam (Eq. 3.6).

As shown in Fig. 3.7, we assume that the edge boundaries of water zones shown in processed foam images are in positions of the leading edges of the curved water-gas interfaces, as the refractive index of water is closer to that of glass when compared to gas. Therefore, there is a part of water along the edge of water zones, which is not included in the previous calculation of water volume. The uncertainty of water saturation δ_1 due to this is given by:

$$\delta_1 = \frac{V_e}{V'_f} = \left(\frac{4 - \pi}{8} \right) \frac{d_a^2 L_p}{V'_f} \quad (3.7)$$

where V_e is the volume of the water along the edge of water zones in the images (shown in purple in the schematic of Fig. 3.7), V'_f is the fracture volume within the image region, d_a is the local aperture of water-gas interfaces, and L_p is the total length of perimeter of water zones in the images.

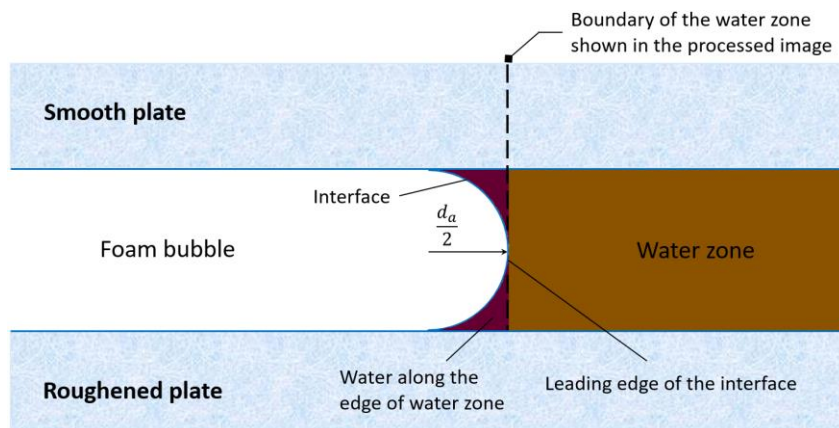


Figure 3.7. Schematic of a foam bubble contacting a water zone in the fracture. The dashed line marks the boundary location of the water zone shown in the processed foam image.

In addition, capillary pressure calculated using Eq. 3.6 assumes that water-gas interfaces are cylindrical with only one principle direction of curvature, because aperture of the interfaces (tens of microns) is much smaller than the radius of the interfaces r_h viewed from above (hundreds of microns). Thus, the estimation uncertainty of capillary pressure δ_2 by ignoring principal radius of curvature in the horizontal direction r_h is given by:

$$\delta_2 = \frac{\gamma_s \cos\theta}{r_h} \quad (3.8)$$

Using Eqs. 3.7 and 3.8, we obtain the uncertainty of our methods in estimating water saturation and capillary pressure. We present these values in Table 3.2.

	Time, hr	Water saturation, S_w , %	Capillary pressure, P_c , kPa	Total length of perimeter of water zones, L_p , mm	Volume of water along the edge of water zone, V_e , 10^{-2} mm^3	Principle Radius of interfaces in parallel with the fracture plane, r_h , μm	Uncertainty of water saturation, δ_1 , %	Uncertainty of capillary pressure, δ_2 , kPa
Model A (regular roughness), $d_H = 46 \mu\text{m}$	0.08	6.0	2.01	79	0.87	200	0.8	0.15
	0.4	4.2	2.21	75	0.68	281	0.7	0.11
	0.8	3.7	2.46	76	0.55	355	0.6	0.09
	1.7	1.2	3.37	44	0.17	429	0.2	0.07
	5							
	10							
	17.5							
	24							
Model B (irregular roughness), $d_H = 78 \mu\text{m}$	0.1	11.6	0.84	118	7.34	198	0.8	0.16
	0.4	10.1	0.89	128	7.15	240	0.7	0.13
	0.8	9.8	0.90	127	6.85	282	0.7	0.11
	1.7	8.6	0.91	122	6.41	358	0.7	0.09
	5	7.2	0.93	102	5.19	498	0.6	0.06
	10	5.9	0.96	111	5.33	563	0.9	0.06
	17	4.6	1.00	95	4.18	606	0.5	0.05
24	4.3	1.03	89	3.68	615	0.4	0.05	

Table 3.2. Uncertainty of water saturation and capillary pressure of foam in the two model fractures. Data in Model A after 5 hr are not presented, because there are no water zones at locations of narrow apertures and it is then difficult to estimate the local aperture of water-gas interfaces for these calculations.

3.6 Conclusions

In this chapter, we report a novel technique to analyze foam texture, and especially to estimate water saturation and capillary pressure of foam. We show that, in model fractures, water in foam lies in four locations: water zones at narrow aperture, Plateau borders, lamellae, and water films on glass plates. We relate the aperture distribution of model fractures and water-occupied area fraction to estimate the local aperture of water-gas interfaces. Using imaging analysis, we calculate water volume in the four different locations, and estimate water saturation and capillary pressure. We conclude that water zones and Plateau borders account for almost all the water of foam in model fractures. During re-distribution of water and gas in static foam with no bubble flow after shut-in, water flows in and out through the fracture following paths through Plateau borders and water zones, which are the only continuous paths for water flow. In model fractures, the decrease in water saturation coincides with the increase in capillary pressure, as expected. The uncertainty analysis in Section 3.5 confirms that our technique is reasonably accurate. Foam texture and properties including water saturation and capillary pressure have often been left unmeasured in previous studies. Our technique provides useful insights for studies of foam in porous media with complex geometry, where measuring such foam properties is challenging. This analysis is possible because our model fractures have variable aperture, unlike most microfluidic devices with uniform depth of etching.

4 Coarsening of Foam in Model Fractures²

4.1 Introduction

Coarsening reflects gas diffusion between foam bubbles that are not in pressure equilibrium. It can alter the structure of foam and weaken its capacity to reduce the mobility of gas. Therefore, it is important to understand coarsening to predict foam behavior. Foam coarsening by diffusion (Ostwald ripening) has been well studied in the context of bulk foam (Cohen-Addad et al., 1998; Weaire and Hutzler, 2001; Weaire, 2008; Cantat et al., 2013). By considering the mean number of faces per bubble, the classical von Neumann law describes coarsening behavior in bulk foams (Monnereau and Vignes-Adler, 1998). In bulk foams, coarsening usually interferes with drainage, enhancing the drainage velocity (Saint-Jalmes and Langevin, 2002). Hilgenfeldt et al. (2001) studied the coupling effects of these two mechanisms on foam evolution. They found that strong coarsening led to drainage times that were shorter and independent of the initial liquid content. They also incorporated the physics of both diffusive coarsening and drainage in their model and showed quantitative agreement with experiments. However, foam coarsening is less well understood in porous media. In particular, the mechanisms that may slow or stop coarsening have not been fully investigated. In porous media, foam bubbles rapidly attain a size close to or bigger than pore body. Plateau borders form where lamellae meet the walls. Gas can diffuse much faster through thin lamellae than through Plateau borders or bulk water.

Marchalot et al. (2008) studied foam coarsening in a microfluidic system (length \times width \times height: $2500 \times 1500 \times 40 \mu\text{m}$). They found that a typical time of foam ageing was about 2 to 3 min for polydisperse foam. The typical time would increase as the polydispersivity of foam bubbles decreases. They argued that most diffusion occurred through lamellae and the lamella height was about one-tenth of the height of the system. Jones et al. (2018b) also investigated coarsening behavior in a microfluidic model (length \times width \times height: $6000 \times 800 \times 5 \mu\text{m}$). They observed three coarsening regimes. Bubble size (2D average bubble area) of foam grew linearly with time at the beginning of coarsening. The coarsening rate then decreased as the effects of wall constraints became significant. The coarsening finally stopped after around half an hour, with the majority of lamellae located in pore throats, where lamella curvature was close to zero.

In this chapter, we repeat and extend the experiments of Chapter 3 to further investigate how foam evolves during coarsening by gas diffusion in models (Models A and B) approximating the geometry of a narrow natural fracture in a geological formation. Model A has regular roughness (Fig. 2.3), with a hydraulic aperture of $46 \mu\text{m}$. Model B has irregular roughness (Fig.

² This Chapter is based on Li, K., Sharifnik, M., Wolf, KH., and Rossen., W.R. 2021. Coarsening of Foam in Two Model Fractures with Different Roughness. *Colloids and Surfaces A: Physicochemical and Engineering Aspects*. <https://doi.org/10.1016/j.colsurfa.2021.127666>.

2.4), with a hydraulic aperture of $78 \mu\text{m}$. Unlike microfluidic models with uniform depth of etching (Buchgraber et al., 2012; Gauteplass et al., 2015), our model fractures each represents an open slit-like channel and has a distribution of continuously varied apertures over space. As described in Subsection 2.2.3, they are analogous to a 2D network of pore bodies (locations with wide aperture) and pore throats (locations with narrower aperture, connecting pore bodies).

To study coarsening, we inject pre-generated foam into the model fractures and shut in the fractures after foam flow reaches steady-state. Foam then coarsens once it stops flowing in the fractures. As our models are transparent, we visualize foam coarsening in the fractures by using a high-speed camera. We use ImageJ software to analyze foam images to study how foam evolves during coarsening in the fractures. In particular, we study how coarsening affects foam texture and lamella location. In addition, we use the technique of image analysis reported in Chapter 3 to estimate water saturation and capillary pressure of foam. We then estimate the height of lamellae through which gas can diffuse, and discuss how it relates to coarsening behavior.

4.2 Experiments and image analysis

In this Chapter, we conduct in total four experiments in the two model fractures (Table 4.1). We pre-generate foam by injecting surfactant solution and gas through the mixing tee at foam qualities f_g of 0.9 and 0.4 for both model fractures. The total interstitial velocity is 1.2 mm/s and 2 mm/s for Models A and B, respectively. The experimental procedures are described in detail in Section 3.2. We have observed that gas enters the fracture as relatively large bubbles instead of slugs. Within the model fracture, foam is further refined during propagation due to in-situ bubble generation. After foam flow achieves steady-state, we maintain the injection for at least 1.5 hr, and then shut in the model fracture for 24 hr at 20°C .

Experiment	Model fracture	Hydraulic aperture, μm	Total interstitial velocity, mm/s	Foam quality, -	Location where images are recorded (distance from fracture inlet), cm
4.1	Model A (regular roughness)	46	1.2	0.9	19
					73
4.2	Model A (regular roughness)	46	1.2	0.4	73
4.3	Model B (irregular roughness)	78	2	0.9	19
					73
4.4	Model B (irregular roughness)	78	2	0.4	73

Table 4.1. Coarsening experiments conducted in this chapter and locations where foam images are recorded in the model fractures.

Figure 4.1 shows pressure gradient with foam (calculated based on pressure drop from the inlet to the outlet of the model fractures) in the four experiments. Time zero in Fig. 4.1 marks the beginning of foam injection into the fractures. In both model fractures, steady-state foam at foam quality 0.9 reaches a greater pressure gradient than at foam quality 0.4. The experimental

observations are the same as described in Section 3.2. As we extend the experiments, here we review the coarsening behaviors described there. After shut-in, water and gas in foam flow along the model fractures to equalize pressure. At the beginning of the shut-in period, foam continues to flow, governed by a residual pressure gradient (Fig. 4.1). Once this pressure gradient drops below a value that cannot compete with the yield stress of the foam, foam mostly stops flowing (0.08, 0.09, 0.10 and 0.12 hr after the shut-in of the fractures for Experiments 4.1, 4.2, 4.3 and 4.4, respectively) and starts to coarsen due to diffusion between bubbles. As shown in Fig. 4.1, there is a small negative pressure gradient from the outlet toward the inlet of the fractures after foam stays at rest. This reverse pressure gradient evidently resulted from a small leak in the tubing upstream of the models. As a result, during foam coarsening in our experiments, except Experiment 4.4, trains of bubbles occasionally flowed in short bursts along separate pathways from the outlet toward the inlet. We also observed rare coalescence (rupture of lamellae) during convection of the bubble trains. However, bubble texture wasn't much different after those intermittent periods of convection: the occasional convection of bubbles along separate pathways and coalescence of lamellae haven't significantly affected the overall behavior of foam coarsening in our study. In addition, water in foam is transported along our models even during periods with no bubble flow.

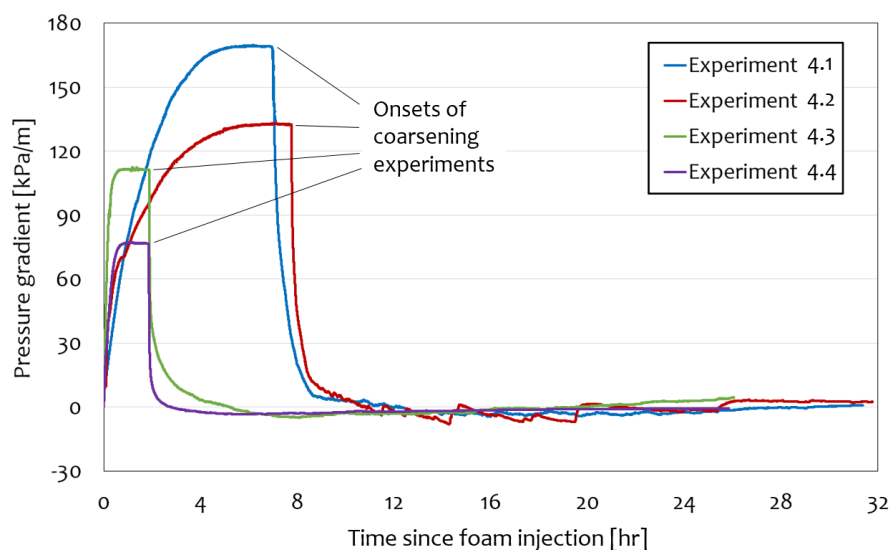


Figure 4.1. Pressure gradient of foam as a function of time since foam injection. Experiments 4.1 and 4.2 are conducted in Model A ($d_{HA} = 46 \mu\text{m}$) at foam quality 0.9 and 0.4, respectively; Experiments 4.3 and 4.4 are conducted in Model B ($d_{HB} = 78 \mu\text{m}$) at foam quality 0.9 and 0.4, respectively.

To study these behaviors, we investigate foam at different locations in the model fractures and record the images of coarsening for 24 hr at 4 frames per minute (see Table 4.1 for locations where images are recorded in each experiment). In this chapter, we set time to zero at the time of shut-in, as the onset of our each coarsening experiment. As shown in Fig. 4.2, we record foam images at an upstream location 19 cm from fracture inlet, where foam is still relatively coarse-textured, and a downstream location 73 cm from the inlet, where foam has a finer texture before coarsening begins. We use ImageJ software to quantify foam texture at different times of coarsening by measuring bubble density (number of bubbles per unit area of image), bubble size (2D average bubble area), area fraction of water-occupied zones at narrow aperture, and total length of lamellae. At steady state with injected foam quality 0.9, foam at location 73 cm

from the inlet has a bubble size (2D average bubble area) 23% and 38% smaller than the upstream foam at 19 cm in Models A and B, respectively.

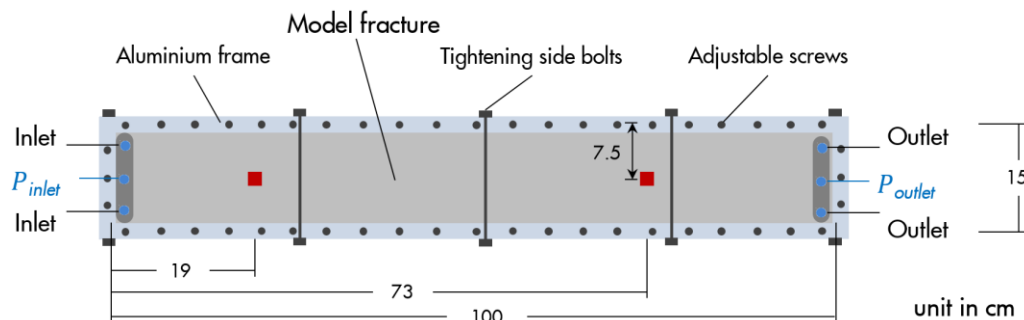


Figure 4.2. Horizontally-placed model fracture mounted in the aluminum clamping frame (top view). The red squares indicate the locations where foam is studied in this chapter.

In Chapter 3, we have concluded that water in foam within the images in our model fractures resides in four locations: water zones that occupy locations of narrow aperture, Plateau borders, lamellae between bubbles, and water films that wet glass walls above and below. As lamellae and water films have a small thickness of 30 nm (Hirasaki, 1991; Bergeron and Radke, 1992), water zones of narrow aperture and Plateau borders thus account for almost all the water. Using the technique reported in Chapter 3, we estimate local aperture of water-gas interfaces, water saturation, and capillary pressure of foam during coarsening. In addition, we estimate the height of the lamella surface that locates in a pore throat in the model fractures as $(d_t - d_a)$, where d_t is the typical pore-throat aperture of the model fractures (Table 2.1), and d_a is the local aperture of water-gas interfaces.

4.3 Foam coarsening in two model fractures with different roughness

During coarsening in the model fractures, we also observed rare coalescence events (rupture of lamellae). However, the coalescence of lamellae hasn't significantly affected the overall behavior of foam coarsening in our experiments. Figure 4.3 shows bubble density and bubble size at different locations in the two model fractures during a 24-hr coarsening period. These experiments are conducted at foam quality f_g of 0.9. In both model fractures, bubble density decreases and bubble size increases as foam coarsens. During coarsening, gas in bubbles at higher pressure diffuses through lamellae to bubbles at lower pressure. As a result, some bubbles disappear as all their gas diffuses into neighboring bubbles, and the remaining bubbles enlarge in size. As shown in Fig. 4.3, foam properties stay the same after 5 hr in Model A, indicating that coarsening stops. In Model B, coarsening rate slows down after 18 hr and bubble size still increases even up to 24 hr. It implies an ongoing gas diffusion, though at a small rate.

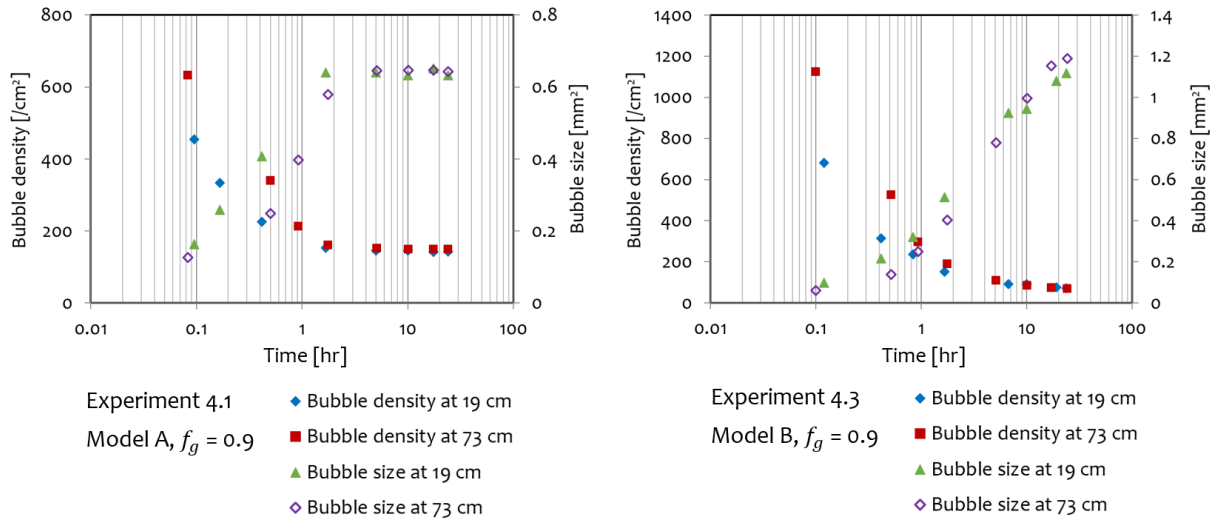


Figure 4.3. Bubble density and bubble size at different locations during coarsening in Models A (left) and B (right). Foam is injected at foam quality 0.9.

As coarsening stops in Model A and slows down to a small rate after 18 hr in Model B, foam gains the same bubble texture at 19 cm as at 73 cm from the fracture inlet for both models. However, bubble size increases at a greater rate in the first two hours at 19 cm than at 73 cm in both models, reflecting a greater coarsening rate. Figure 4.4 shows bubble number per pore body as a function of coarsening time for the two models. After coarsening stops in Model A, there is one bubble in each pore. In Model B, on average 3.3 bubbles stay in one pore after 24 hr of coarsening. Unlike in Model A, the definition of pore bodies in Model B is ambiguous, because there may be multiple local minima in height between well-defined pore boundaries (Fig. 2.4) in Model B. It is possible that a lamella might locate at the saddle point between two of these minima, with zero curvature, at the end of the coarsening experiment.

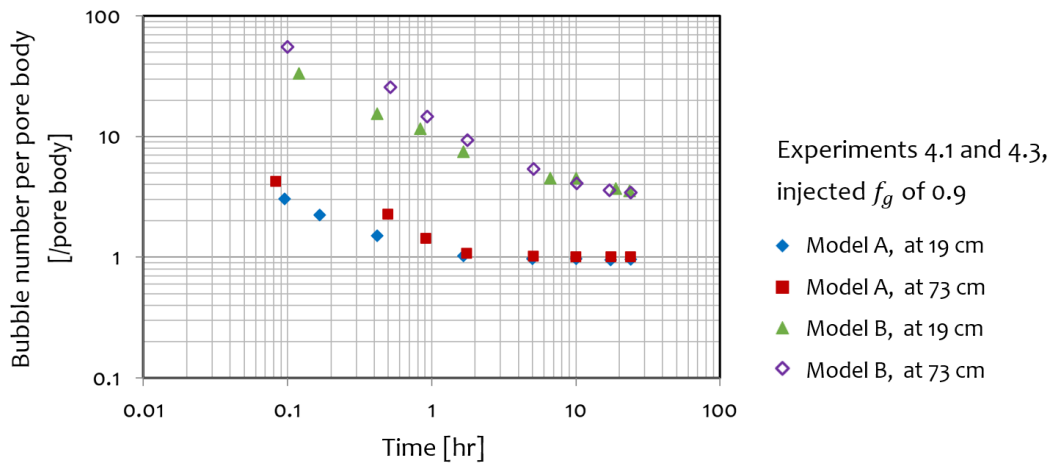


Figure 4.4. Bubble number per pore body at different locations during coarsening in Models A and B (Experiments 4.1 and 4.3). Foam is injected at foam quality 0.9.

Figures 4.5 and 4.6 display processed images of foam at different times of coarsening at the two different locations in Model A with regular roughness (Experiment 4.1, at injected foam quality 0.9). Bubbles each attain the same size as the pore body as coarsening stops in Model A. All lamellae then locate in pore throats with zero curvature. Although the lamella surface

area at 24 hr has an estimated height of $28\ \mu\text{m}$ at position 19 cm, and up to $55\ \mu\text{m}$ at position 73 cm in the fracture, coarsening stops, as all bubbles are in pressure equilibrium, with no driving force for gas diffusion.

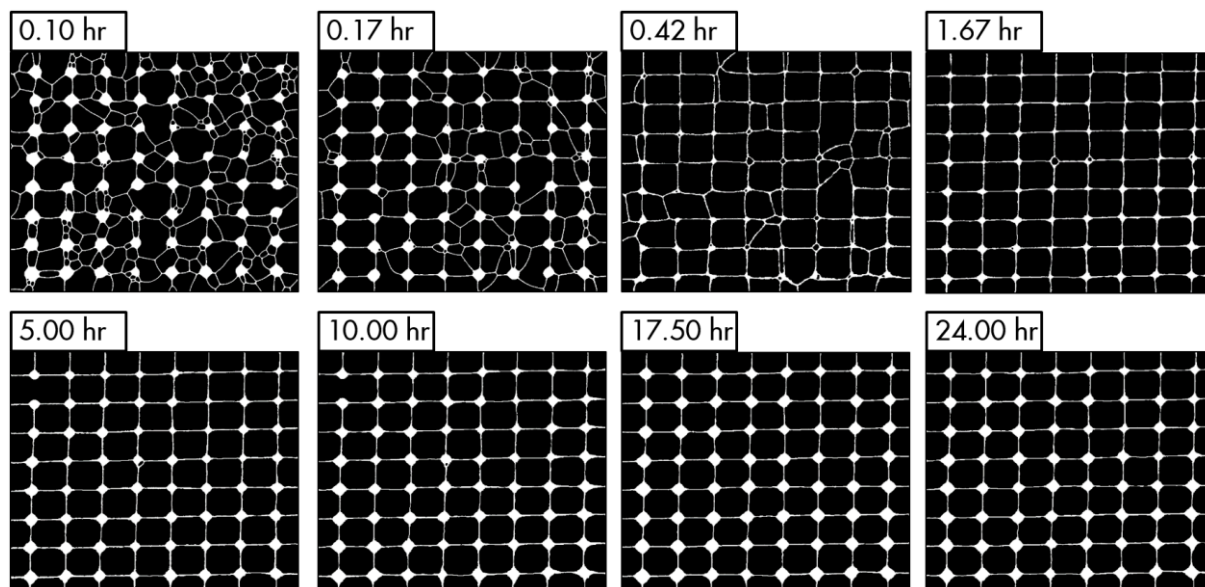


Figure 4.5. Processed images of foam 19 cm from the fracture inlet at different times of coarsening in Experiment 4.1 (in Model A with regular roughness, at foam quality 0.9), image size: 7.8×6.8 mm. Water is shown in white, gas in black.

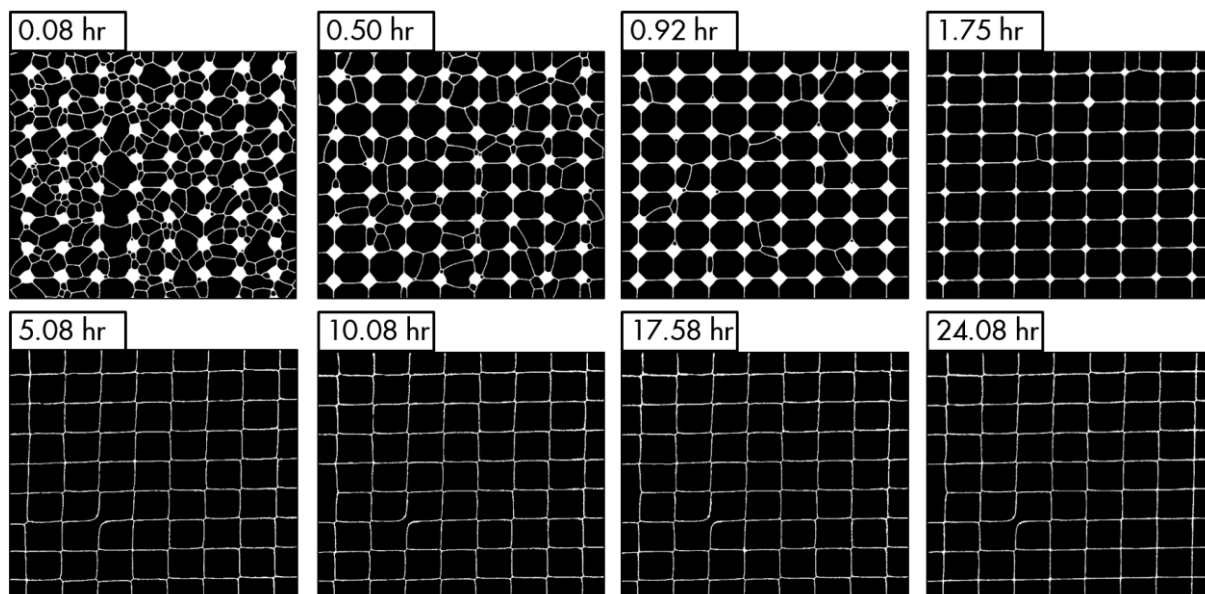


Figure 4.6. Processed images of foam 73 cm from the fracture inlet at different times of coarsening in Experiment 4.1 (in Model A with regular roughness, at foam quality 0.9), image size: 7.8×6.8 mm. Water is shown in white, gas in black.

Figures 4.7 and 4.8 display processed foam images during coarsening at the two locations in Model B (Experiment 4.3, at injected foam quality 0.9). Compared to Model A, Model B has a complex fracture geometry, due to its irregular roughness. In this fracture, a relatively small undulation in the bottom of a pore would not define a new pore. Therefore, it is challenging to conclude where lamellae locate in Model B after 24 hr of coarsening, with multiple foam

bubbles residing in one pore. During coarsening in the model fractures, foam bubbles restructure and lamellae relocate to achieve their minimum surface area. We therefore identify three types of lamella location in Model B at the end of Experiment 4.3: 1) in pore bodies, possibly at a local rise of height on the irregular-roughened plate: i.e., at the saddle point between two minima of height in the same pore body; 2) at pore throats; and 3) at locations of narrow aperture. We estimate the height of the lamella of case 1) as $(d_b - d_a)$, and that of case 2) as $(d_t - d_a)$, where d_b and d_t are the typical apertures of pore body and pore throat, respectively (Table 2.1), and d_a is the local aperture of water-gas interfaces. The estimated lamella heights of the first two cases are 112 and 30 μm for both locations at 19 and 73 cm on Model B. There would be gas diffusion through these lamellae if there were driving force. However, as shown in the bottom-right images (at 24 h) of Figs. 4.7 and 4.8, the lamellae of cases 1) and 2) may not be moving at the end of the coarsening process in Experiment 4.3, as they are in positions of little or no curvature, with little or no driving force for diffusion. Lamellae of case 3) form the exposed sides of small bubbles wedged into locations of narrow aperture in Model B, as shown in the red boxes in the bottom-right image of Fig. 4.8. Gas in these small bubbles with greater curvature has higher pressure compared to the neighboring bubbles. However, they can remain in place for a considerable period of time. At these locations, the estimated height of these lamellae is close to zero. Thus there is little or no lamella surface area for gas diffusion.

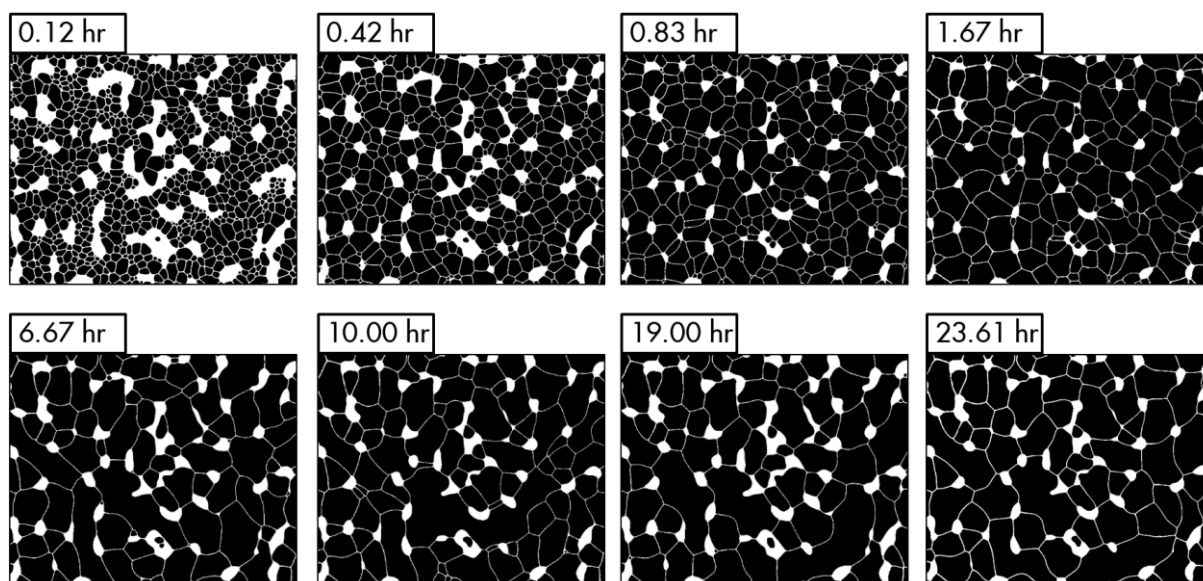


Figure 4.7. Processed images of foam 19 cm from the fracture inlet at different times of coarsening in Experiment 4.3 (in Model B with irregular roughness, at foam quality 0.9), image size: 12.3×9.8 mm. Water is shown in white, gas in black.

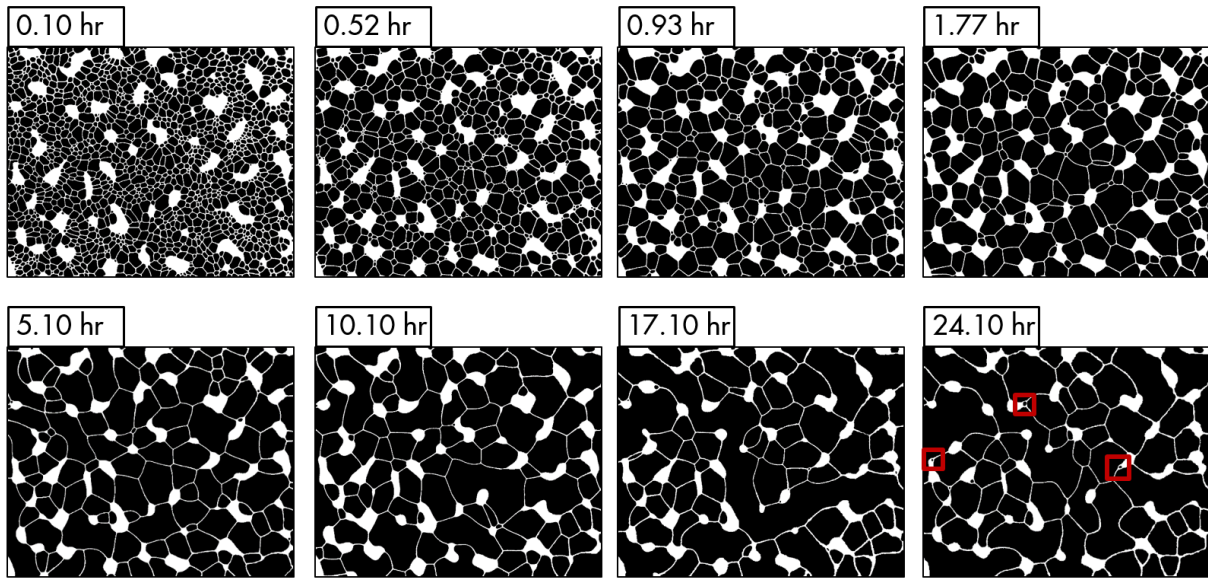


Figure 4.8. Processed images of foam 73 cm from the fracture inlet at different times of coarsening in Experiment 4.3 (in Model B with irregular roughness, at foam quality 0.9), image size: 12.3×9.8 mm. Water is shown in white, gas in black. Small bubbles in red boxes in the image at 24 hr are in locations of narrow aperture in the model fracture.

Figure 4.9 shows water saturation of foam during the 24-hr coarsening period in the model fractures. Water saturation at the two locations of both models decreases as foam coarsens, except that water saturation first decreases and then slowly increases after 2 hr at 19 cm in Model A. The water saturation at 73 cm in Model A from 5 hr of coarsening is not known. As shown in Fig. 4.6, as coarsening stops at 73 cm in Model A after 5 hr, there are no local water-occupied zones at positions of narrow apertures, and almost all water in foam locates in Plateau borders, at relatively high capillary pressure. It is then difficult to estimate the local aperture of water-gas interfaces, and from that the radius of Plateau borders, water saturation and capillary pressure. At the higher capillary pressure, the water saturation after 5 hr is nevertheless at least lower than that at 1.75 hr.

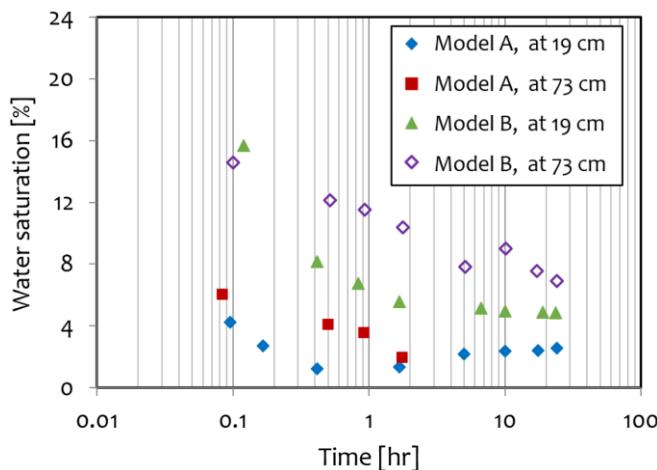


Figure 4.9. Water saturation of foam at different locations during coarsening in Models A and B. Foam is injected at foam quality 0.9.

After shut-in, this decrease of water saturation in both model fractures suggests that water continuously flows upstream into the inlet trough, tubing and fittings upstream of the model

through the network of Plateau borders and water zones even without bubble flow, under the small pressure gradient from outlet toward inlet (Fig. 4.1). At 19 cm, the foam is drier compared to 73 cm for both model fractures. This explains why foam coarsens at a greater rate at 19 cm compared to 73 cm, as the drier foam has Plateau borders of smaller dimension under higher capillary pressure, and hence larger lamella surface area available for diffusion.

4.4 Foam coarsening at two different injected foam qualities

Figure 4.10 compares bubble number per pore body during coarsening of foam injected at different foam qualities 0.4 and 0.9 in the two models. These data are based on analysis at the location 73 cm from the fracture inlet. Figures 4.11 and 4.12 display processed foam images at foam quality 0.4 at 73 cm in Models A and B (Experiments 4.2 and 4.4), respectively. In Model A, the coarsening of both foams at foam qualities 0.4 and 0.9 stops at about 5 hr, with one bubble occupying one pore. At injected foam quality 0.4, the estimated height of lamellae is $43 \mu\text{m}$ at the end of the coarsening. Similarly with foam at quality 0.9, all these lamellae at quality 0.4 locate at pore throats with zero curvature at 24 hr. There is no gas diffusion through these lamellae, and all bubbles are in equilibrium.

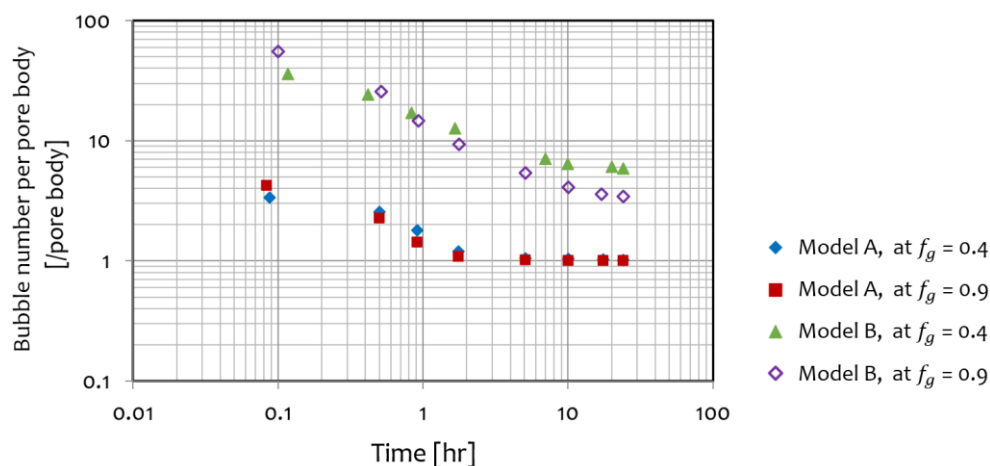


Figure 4.10. Bubble number per pore body during coarsening at different injected foam qualities in Models A and B. Data are based on foam analysis at 73 cm from the fracture inlet.

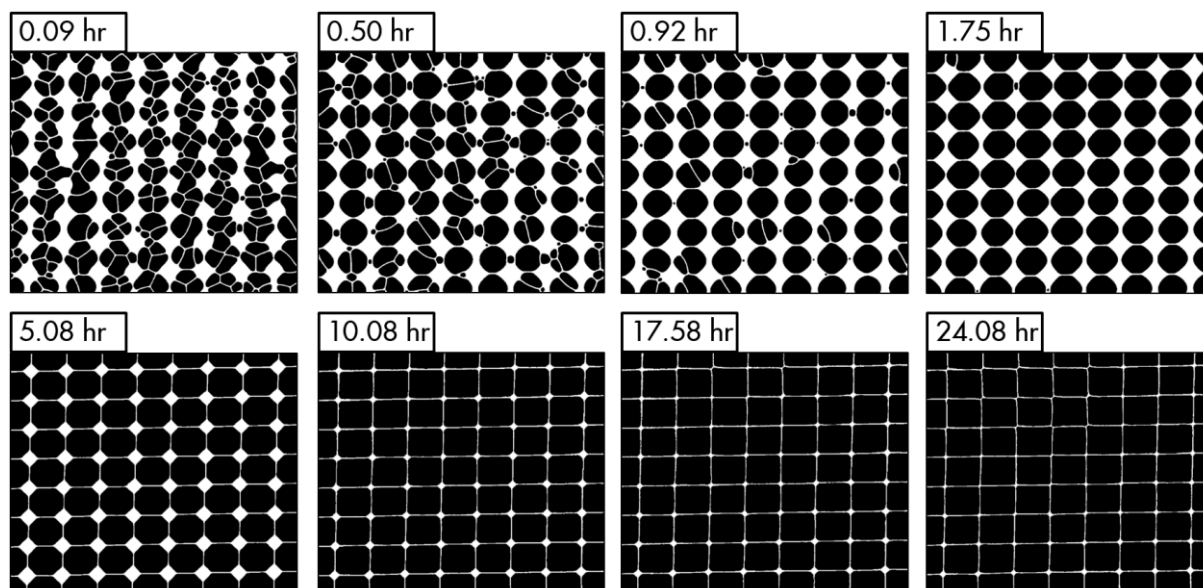


Figure 4.11. Processed images of foam 73 cm from the fracture inlet at different times of coarsening in Experiment 4.2 (in Model A with regular roughness, at foam quality 0.4), image size: 7.8×6.8 mm. Water is shown in white, gas in black.

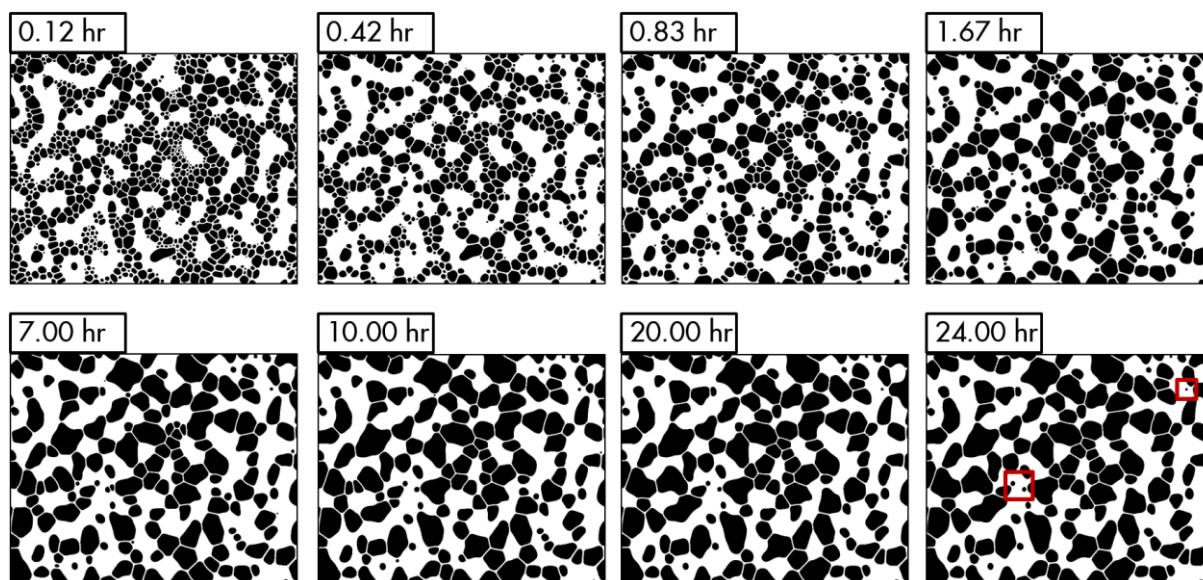


Figure 4.12. Processed images of foam 73 cm from the fracture inlet at different times of coarsening in Experiment 4.4 (in Model B with irregular roughness, at foam quality 0.4), image size: 12.3×9.8 mm. Water is shown in white, gas in black. Small bubbles in red boxes in the image at 24 hr are in locations of narrow aperture in the model fracture.

In Model B, compared to foam quality 0.9, foam injected at quality 0.4 coarsens at a slower rate. At the end of the coarsening experiment (at 24 hr), compared to 3.3 bubbles in one pore for foam injected at quality 0.9, there are 6 bubbles for foam at quality 0.4. Figure 4.13 shows water saturation at different injected foam qualities at position 73 cm from fracture inlet during the 24-hr coarsening period in the two model fractures. Water saturation at both foam qualities decreases as foam coarsens. During coarsening, water flows upstream into the inlet trough, tubing and fittings upstream of the model through Plateau borders and water zones under the small negative pressure gradient from the outlet toward the inlet of the fractures (Fig. 4.1). This

pressure gradient evidently results from a small leak in the tubing upstream of the models. Figure 4.14 shows capillary pressure as a function of water saturation of foam during coarsening at the location 73 cm from the fracture inlet in the two models. In both model fractures, the decrease in water saturation coincides with the increase in capillary pressure, as expected. The water saturation at foam quality 0.9 in Model A after 5 hr of coarsening is not given. There are no local water-occupied zones at locations of narrow apertures (Fig. 4.6). Almost all water in foam locates in Plateau borders. It is then difficult to estimate the local aperture of water-gas interfaces, and from that the radius of Plateau borders, water saturation and capillary pressure. It is evident that the out-flow water rate is greater than the in-flow water rate at position 73 cm from the inlet of Model A. The water saturation after 5 hr there is at least lower than that at 1.75 hr, with greater capillary pressure.

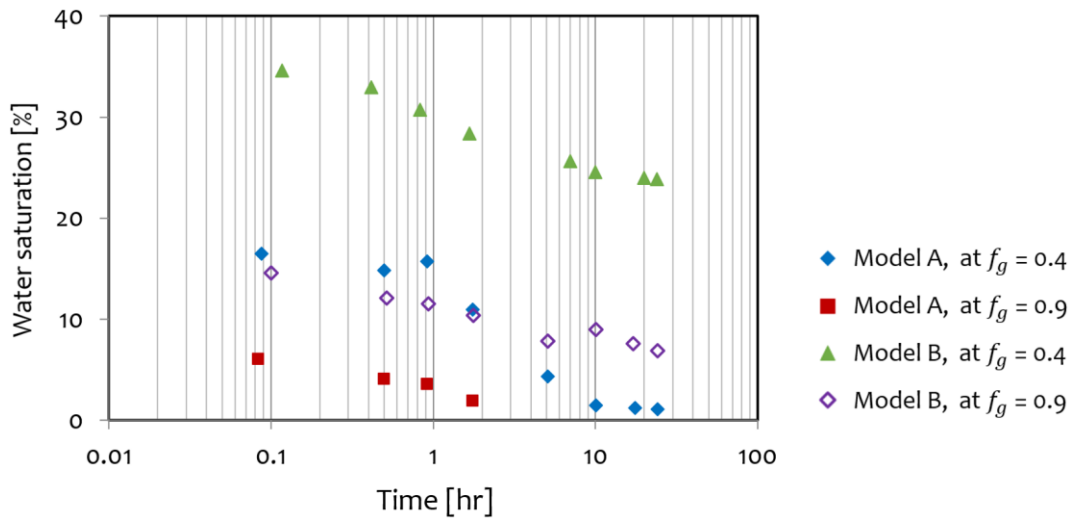


Figure 4.13. Water saturation of foam at different injected foam qualities during coarsening in Model A and Model B. Data are analyzed at the position 73 cm from fracture inlet.

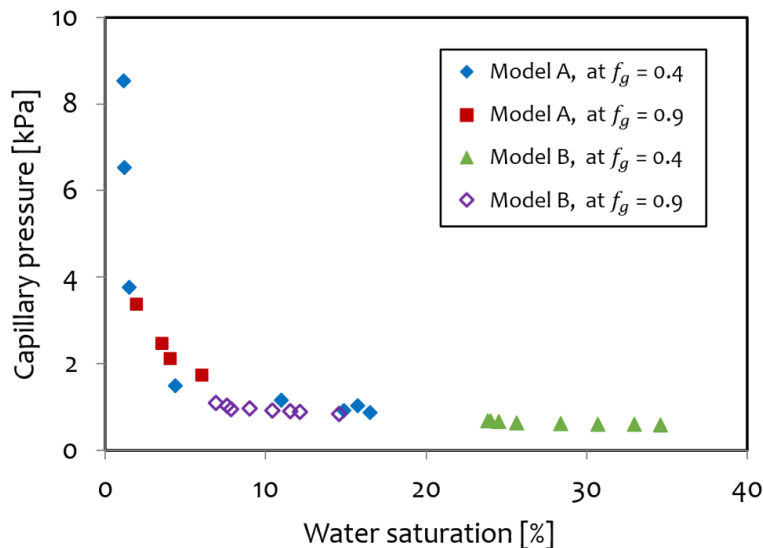


Figure 4.14. Capillary pressure as a function of water saturation of foam in the two model fractures.

At wetter conditions, the local aperture at water-gas interfaces in the fracture is larger, due to the lower capillary pressure. The Plateau borders of foam therefore are larger, and the height of lamellae between bubbles is smaller. Compared to dry foams, this lack of lamellae in wet

foams slows gas diffusion: hence the slower coarsening at foam quality 0.4. Similarly with foam at quality 0.9, lamellae of foam at quality 0.4 also stay in three locations of narrow aperture in Model B at the end of the coarsening experiment (bottom-right image in Fig. 4.12). However, the lamellae have smaller heights there: lamellae of case 1) possibly locate at a local rise of height in pore bodies. They have little or no curvature with an estimated height of 80 μm ; Lamellae of case 2) locate at pore throats and have an estimated height close to 0; and lamellae of case 3) form the exposed sides of small bubbles (as shown in the red boxes in the bottom-right image of Fig. 4.12) at narrow aperture in Model B. The estimated height of lamellae of this case is also close to 0. The gas diffusion rate through lamellae of all three cases is thus either zero or much weak at the end of the coarsening experiment.

4.5 Discussion

In this chapter, we have reported an experimental coarsening study of foam in two model fractures. Unlike microfluidic models with uniform depth of etching, our slit-like open fractures each have a distribution of apertures in space. Because of this variation, foam coarsening stops or reaches an insignificant rate as all lamellae move in locations with local minima in surface area, such as pore throats or local saddle points between two minima of heights in pore bodies. Coarsening rate approaches zero for bubbles at locations of narrow aperture (local hills on the roughened plates) because lamellae area approaches zero. Fracture models built with two smooth plates (without roughness) with a hydraulic aperture of tens of microns to millimeters have been used to study foam (Pieters and Graves, 1994; Chen et al., 2004; Yan et al., 2006; Géraud et al., 2016). We expect that static foam would coarsen into one large bubble in such models after a period of time, because with uniform aperture there are no locations with local minima in lamella area.

In 2D foams, the coarsening is generally described using von Neumann's law, by assuming that foam is confined in an infinite 2D space and bubbles are separated by lamellae with the same height (von Neumann, 1952; Glazier et al., 1987; Emília Rosa and Fortes, 1999). In our models, the aperture distribution of fractures fundamentally affects the coarsening behavior. The structure of foam is complex, with some water accumulated in locations of narrow aperture in the models. Therefore, it is difficult to formulate a scaling law to predict coarsening behavior in our model fractures. As an initial study, we adopted an image-analysis technique reported in Chapter 3 to relate the fracture geometries and foam bubble properties. In particular, we estimate the height of lamellae based on their locations in the model fractures, to study the coarsening process.

The network of Plateau borders and water zones acts as the paths for water to flow in and out along our fractures during coarsening. Although water zones are mostly narrower in aperture than the Plateau borders, they are much wider in area. This geometry suggests that the water zones have essentially no resistance to flow compared to other parts of the network. In the fractures, the total water saturation, which includes water zones and Plateau borders, is related to capillary pressure. Water is apparently transported from one side of the fractures to the other to equalize the difference in capillary pressure. The implication of the flow conductivity of the network on this water transport behavior deserves further study.

4.6 Conclusions

In this chapter, we study coarsening behavior of foam in two model fractures with different roughness. We find that bubble density decreases and average bubble size increases as foam coarsens in both model fractures. In Model A with regular roughness, coarsening stops and bubbles are in equilibrium after 5 hr. Each bubble then occupies one pore body and all lamellae remain at pore throats with zero curvature. However, foam continues to coarsen up to 24 hr in Model B with irregular roughness, although at a greatly-reduced rate. At the end of the coarsening experiments, either lamellae are in positions of little or no curvature, or the exposed sides of small bubbles wedged into locations of narrow aperture in Model B have an estimated lamella height close to zero. During coarsening in both model fractures, water flows in and out along the fractures following the network of Plateau borders and water zones at narrow apertures. At the two fixed locations in the fractures where we analyze foam, water saturation decreases as foam coarsens, which coincides with an increase in capillary pressure. Compared to foam injected at a lower foam quality, foam at a higher quality coarsens faster. In drier foam, the Plateau borders are smaller in size at higher capillary pressure. The height of lamellae is thus greater, hence allowing faster gas diffusion.

5 Effects of Gas Trapping on Foam Mobility in a Model Fracture³

5.1 Introduction

In unfractured porous media, the ability of foam to reduce the mobility of gas is strongly linked to the fraction of trapped gas, which is captured by capillary forces. Thus understanding the mechanism of gas trapping is crucial for an optimized design of field-scale foam application. Previous experimental studies (Radke and Gillis, 1990; Friedmann et al., 1991) have been carried out to investigate gas trapping in cores, by fitting the profile of a gas tracer in the effluent using a 1D model for tracer transport. It has been concluded that between 80% and almost 100% is trapped. Tang and Kovscek (2006) also reported on experimental work on gas trapping in a sandstone core. They found that trapped-gas fraction ranged from 88% to 56% at gas superficial velocities between 0.4 and 30 m/day. Nguyen et al. (2009) used X-ray CT to reconstruct the effluent tracer concentration. They found that the trapped-gas fraction decreases with an increasing gas rate, but weakly increases with a decreasing liquid rate. More recently, Kil et al. (2011) analyzed those CT images using a more-sophisticated mass-transfer model and estimated the trapped-gas fraction at 99%. Gas trapping has been well studied in unfractured porous media, as the key mechanism to reduce the mobility of gas. However, it is less well understood in fractures.

In this chapter, we study gas trapping in one model fracture (Model B) with irregular roughness (Fig. 2.4), and hydraulic aperture of $78 \mu\text{m}$. In particular, we study how foam evolves along the fracture and we program a macro to quantify gas trapping at given flow conditions. In addition, the effects of gas trapping on foam mobility are discussed. A fracture pore space possesses a very-different pore geometry compared to a grain framework. Therefore, we relate fracture pore-space geometry to the degree of gas trapping using the correlation of AlQuaimi and Rossen (2018a).

5.2 Experiments and image analysis

In this chapter, we pre-generate foam through the mixing tee at a fixed foam quality f_g of 0.9 and at varying total interstitial velocities v_t : 0.12, 0.23, 0.49, 0.89, 1.69, 3.14 and 6.79 mm/s. Foam is then injected into the horizontally-placed model fracture. Seven pressure transducers are used to measure pressure along the flow path. To quantify the mobility of steady-state foam, we use steady-state time-averaged pressure to calculate the apparent viscosity μ_{app} by:

³ This Chapter is based on Li, K., Wolf, K. H. A., and Rossen, W. R. 2021. Effects of Gas Trapping on Foam Mobility in a Model Fracture. *Transport in Porous Media*, **138**(1), 185-200. <https://doi.org/10.1007/s11242-021-01598-y>.

$$\mu_{app} = \frac{1}{12} \frac{1}{q_t} |\nabla P_{foam}| w d_H^3 \quad (5.1)$$

where $q_t = v_t d_H w$ is the total volumetric flow rate, ∇P_{foam} is pressure gradient of steady-state foam flow, w is the width of the model fracture, and d_H is the hydraulic aperture of the model fracture.

To study gas trapping and bubble texture in the foam, multiple images are taken during steady-state foam flow. We use ImageJ software to process images and calculate bubble density (number of bubbles per unit area of the image), bubble size (2D average bubble area), and polydispersity (ratio of standard deviation to average bubble size). The results are time- and location-averaged, meaning that images are taken (Fig. 5.1) and foam is analyzed at different times and also at different locations in each section of the model fracture after each experiment reaches steady-state.

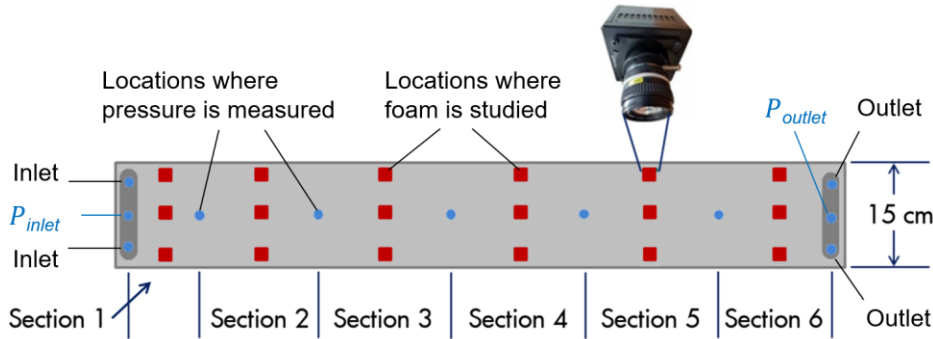


Figure 5.1. Horizontally-placed model fracture (top view). The red squares indicate the locations where foam is studied in this chapter.

In addition, we program a macro to study multiple time-lapse images during a 47-s foam flow. The macro indicates bubbles with a displacement smaller than the average bubble diameter as trapped gas. The area fraction of trapped gas $S'_{g,trap}$ can then be estimated using image analysis by:

$$S'_{g,trap} = \frac{A_{g,trap}}{A_{g,total}} \quad (5.2)$$

where $A_{g,trap}$ is area of trapped gas, and $A_{g,total}$ is the total area of gas within the region of one image. Equation 5.2 is a 2D estimation of trapped-gas fraction. In our model fracture with uneven aperture distribution, gas, trapped or flowing, tends to occupy locations of wider aperture. We believe this equation provides a useful measure of gas trapping and for relating it to pressure gradient and velocity.

5.3 Evolution of foam along model fracture

To investigate how foam evolves along the fracture, foam is first pre-generated and then injected into the fracture. After foam reaches steady-state, we record the pressure data to compute the apparent viscosity of foam (Eq. 5.1). Figure 5.2 shows the apparent viscosity of

foam in different sections along the model fracture (Fig. 5.1) at different total interstitial velocities.

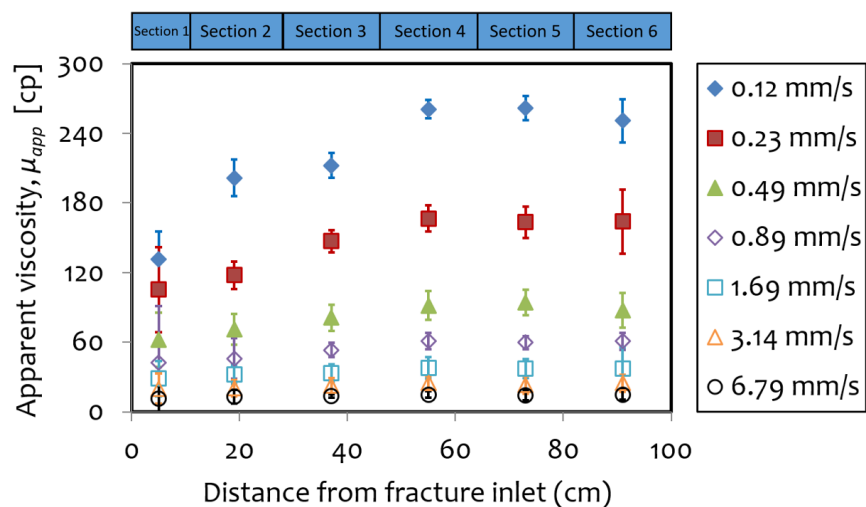


Figure 5.2. Apparent viscosity of foam in different sections along the model fracture at different total interstitial velocities.

As shown in Fig. 5.2, the apparent viscosity of foam monotonically decreases as velocity increases, reflecting the non-Newtonian nature of foam flow. For all velocities, apparent viscosity increases along the fracture, until it reaches its maximum magnitude in the last three sections: pre-generated foam is refined inside the fracture by in-situ foam generation. As foam propagates further along the fracture, it reaches a state with constant mobility.

Although we pre-generate foam through the mixing tee with a frit filter inside (mesh size: 10 μm), foam has coarsened considerably to relatively large bubbles by the time it enters the model fracture. As a result, foam texture is refined as it flows through the fracture. In our model fracture, using pre-generated foam, we have observed that lamella division is the principal mechanism of foam generation in situ. Figure 5.3 illustrates a 2.24-s time-lapse image of this process in section 1 of the model fracture in the experiment at v_t 0.89 mm/s. The highlighted bubbles demonstrate events where moving lamellae are divided, therefore creating new bubbles.

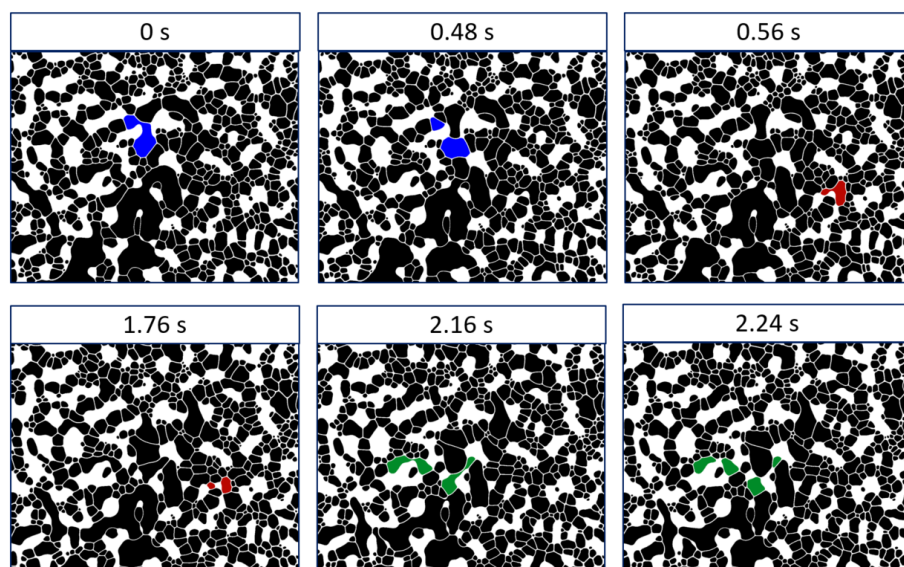


Figure 5.3. Foam generation by lamella division in section 1 of the model fracture. Foam injected at v_t 0.89 mm/s. Gas is shown in black, liquid in white. Liquid occupies areas with narrow aperture in the model fracture. Highlighted bubbles demonstrate foam generation by lamella division. Image size: 19.5×15.6 mm.

As a result of in-situ foam generation, as shown in Fig. 5.4, bubble texture becomes finer along the fracture until it reaches a nearly constant state in the last three sections. It is also evident that the bubbles are not uniform. Figure 5.5 shows bubble density and bubble size in different sections for foam injected at v_t 0.89 mm/s. The statistics are provided in Table 5.1. The standard deviation (SD) of bubble size is large, indicating that foam bubbles in our model fracture are polydisperse (with average polydispersivity of 0.81). Despite the large SD in bubble size, the uncertainty in the mean bubble size distribution is about one-tenth of the SD in our study, based on the 95%-confidence interval (Wonnacott and Wonnacott, 1972). Foam texture reaches a stable and constant state within our 1-m-long model fracture with bubble density increasing along the fracture up to its maximum average (509 per cm^2) in the last three sections, while average bubble size decreases to its minimum (0.139 mm^2). The apparent viscosity is also the same in the last three sections at 60 cp for foam injected at v_t 0.89 mm/s (Fig. 5.2). We conclude that foam has achieved local equilibrium (LE) in our model fracture (Ettinger and Radke, 1992; Ashoori et al., 2010; Chen et al., 2010).

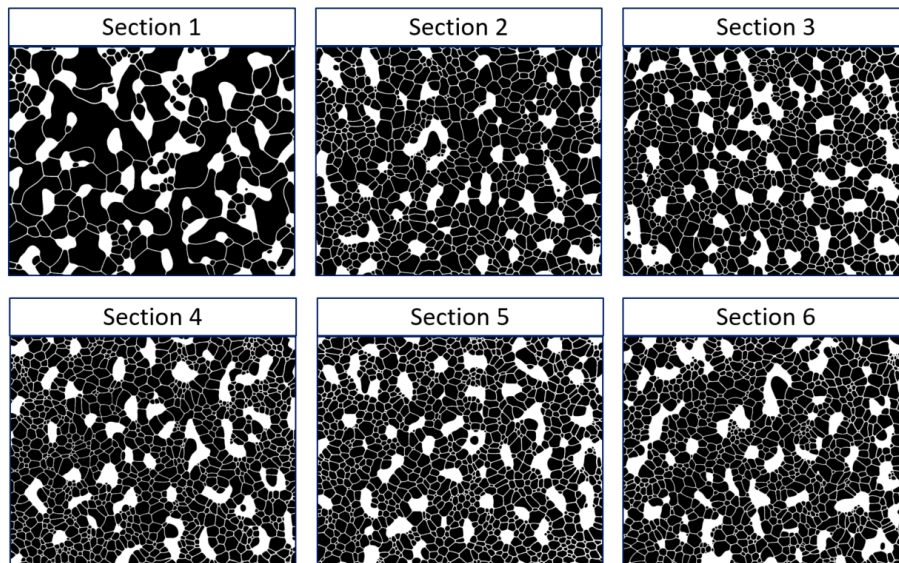


Figure 5.4. Evolution of foam texture in different sections along the model fracture. Foam injected at v_t 0.89 mm/s. Gas is shown in black, liquid in white. Liquid occupies areas with narrow aperture in the model fracture. Image size: 15.7×12.6 mm.

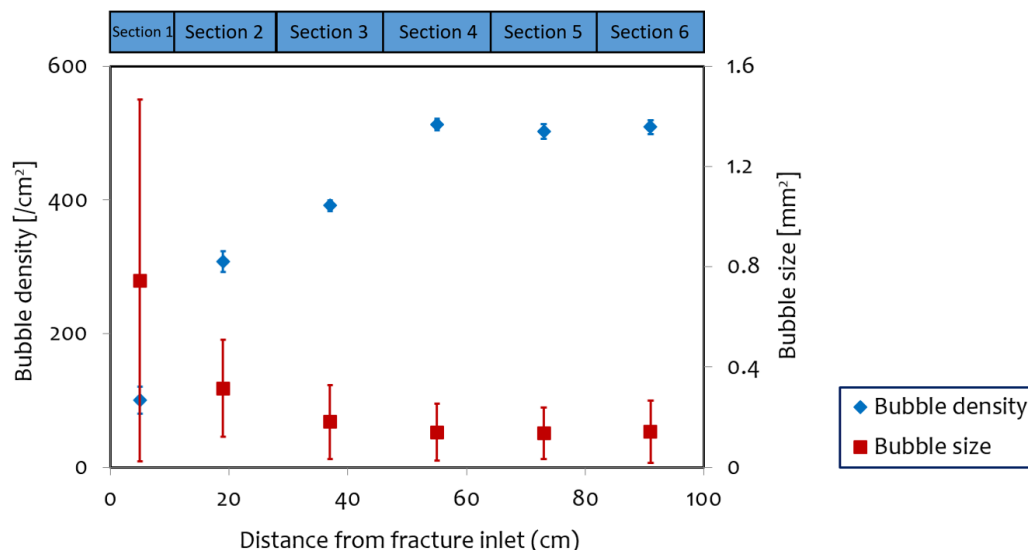


Figure 5.5. Bubble density and bubble size of foam in different sections along the model fracture. Foam injected at v_t 0.89 mm/s.

	Section 1	Section 2	Section 3	Section 4	Section 5	Section 6
Bubble density [1/cm ²]	100	308	391	513	502	509
SD bubble density [1/cm ²]	20	16	8	9	11	10
Bubble size [mm ²]	0.745	0.314	0.180	0.140	0.135	0.142
SD bubble size [mm ²]	0.721	0.193	0.148	0.113	0.102	0.125
Polydispersity [SD/average bubble size]	0.97	0.62	0.82	0.81	0.76	0.88

Table 5.1. Bubble properties in different sections along the model fracture. Foam injected at v_t 0.89 mm/s.

At LE, the rate of bubble generation equals that of bubble destruction. We have not observed bubble destruction, either by capillary coalescence or diffusive coarsening, in our experiments. This is probably because capillary pressure is relatively low and the critical time for foam coarsening by gas diffusion is longer than the residence time in the fracture (AlQuaimi and Rossen, 2019). Since no bubble destruction is observed, the implication is that foam generation also stops in the last three sections.

5.4 Gas trapping and foam mobility

In the rest of this chapter, we examine the properties of foam in the last three sections, where foam is at LE. To study gas trapping, we conduct foam experiments at different velocities. Figure 5.6 shows that there is a strong link between bubble texture and total interstitial velocity. Bubble density increases and bubble size decreases (finer foam texture) as velocity increases. Bubble properties are presented in Table 5.2. The large standard deviation of bubble size reflects the nonuniformity of foam bubbles, with average polydispersivity of 0.62.

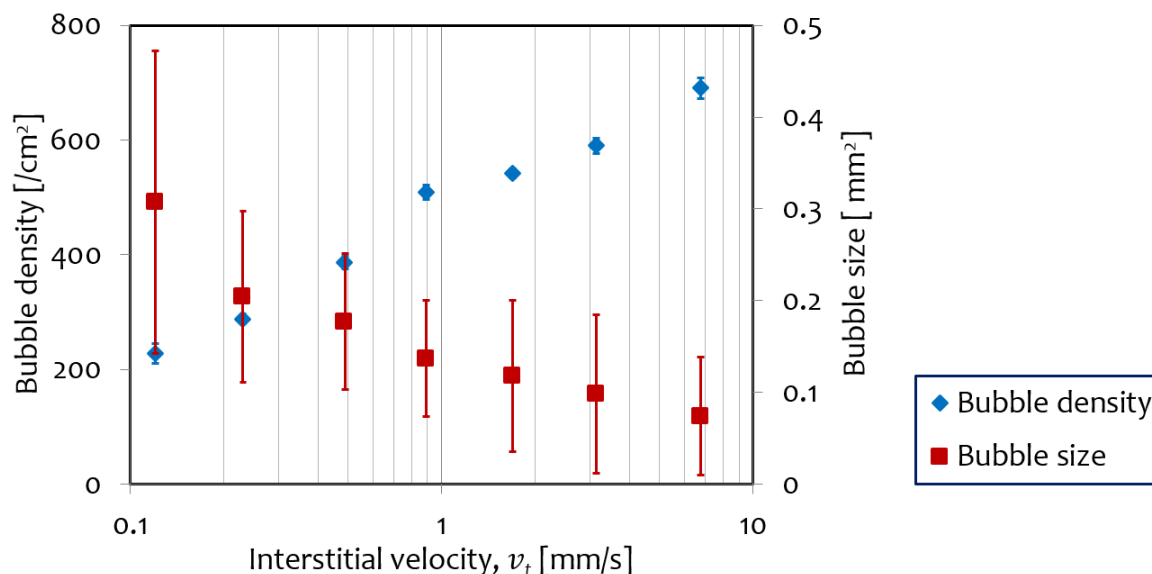


Figure 5.6. Bubble density and bubble size of LE foam at different total interstitial velocities.

Total Interstitial velocity [mm/s]	0.12	0.23	0.49	0.89	1.69	3.14	6.79
Bubble density [1/cm ²]	228	288	386	509	542	590	691
SD bubble density [1/cm ²]	18	9	11	12	8	14	18
Bubble size [mm ²]	0.308	0.204	0.177	0.137	0.118	0.099	0.074
SD Bubble size [mm ²]	0.165	0.093	0.074	0.063	0.082	0.086	0.064
Polydispersivity [SD/average bubble size]	0.54	0.46	0.42	0.46	0.70	0.88	0.87

Table 5.2. Bubble properties of LE foam injected at different total interstitial velocities.

At higher velocities, there is greater foam generation by lamella division. Compared to 0.12 mm/s, bubble density of LE foam injected at 6.79 mm/s increases by a factor of 3 and bubble size decreases by a factor of more than 4. Foam is finer at greater injection velocity.

Figure 5.7 shows the fraction of trapped gas and corresponding pressure gradient of the LE foam injected at different velocities. Trapped-gas fraction decreases as velocity increases. This is consistent with the finding of Jones et al. (2018a) in a microfluidic model. The inverse response of gas trapping with velocity reflects two factors. At low velocities, LE foam bubbles are coarser due to less in-situ division of bubbles (Fig. 5.8). Smaller bubbles are less likely to be trapped, because aperture does not vary as much across the bubble as it does for a larger bubble spanning a pore body. In addition, pressure gradient increases at higher velocities (Fig. 5.7). More gas bubbles become mobile because the increasing viscous forces dominate over capillary forces. Consequently, the amount of stagnant gas diminishes as velocity increases.

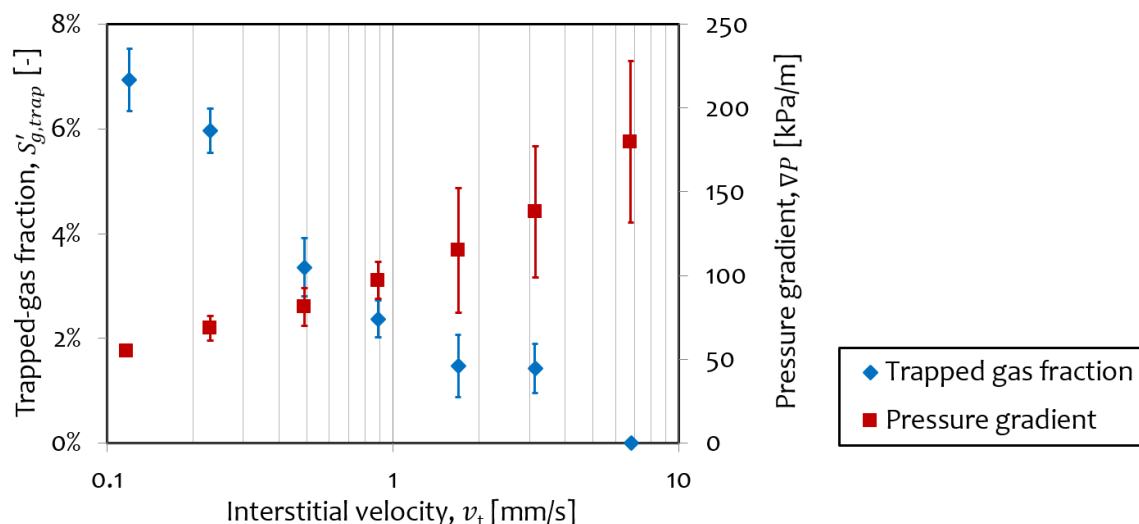


Figure 5.7. Fraction of trapped gas and corresponding pressure gradient of LE foam injected at different total interstitial velocities.

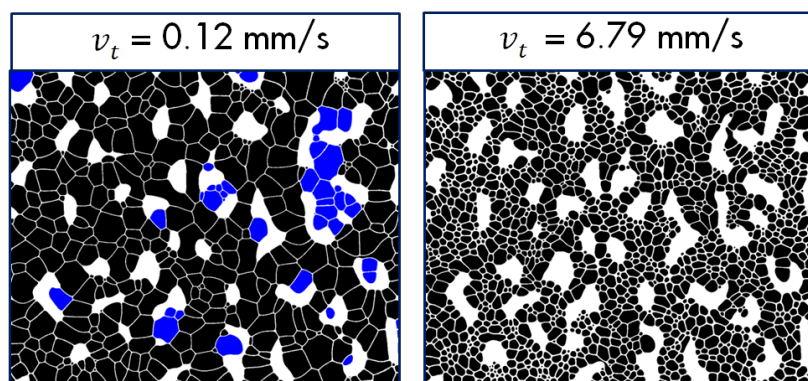


Figure 5.8. Images of foam texture at different interstitial velocities in section 5 of the model fracture. Left: at velocity 0.12 mm/s; right: at velocity 6.79 mm/s. Flowing gas is shown in black, trapped gas in blue, liquid in white. Liquid occupies areas with narrow aperture in the model fracture. Image size: 15.7×12.6 mm.

Compared to previous studies in geological porous media and microfluidic models, the fraction of trapped gas found in our model fracture is very small. At 0.12 mm/s, the fraction of trapped gas is 6.9% (Fig. 5.8, left). When injection velocity increases up to 6.79 mm/s, there is no gas trapping and all bubbles are able to flow (Fig. 5.8, right).

Figure 5.9 displays a strongly shear-thinning rheology in the model fracture. Despite the refinement in foam texture (Fig. 5.8), apparent viscosity decreases by a factor of 17, from 258 cp at 0.12 mm/s to 15 cp at 6.79 mm/s. Meanwhile, the fraction of flowing gas increases from 93.1% to 100%. At this high flowing-gas fraction, it is unlikely that gas trapping plays a key role in a 17-fold increase in foam mobility.

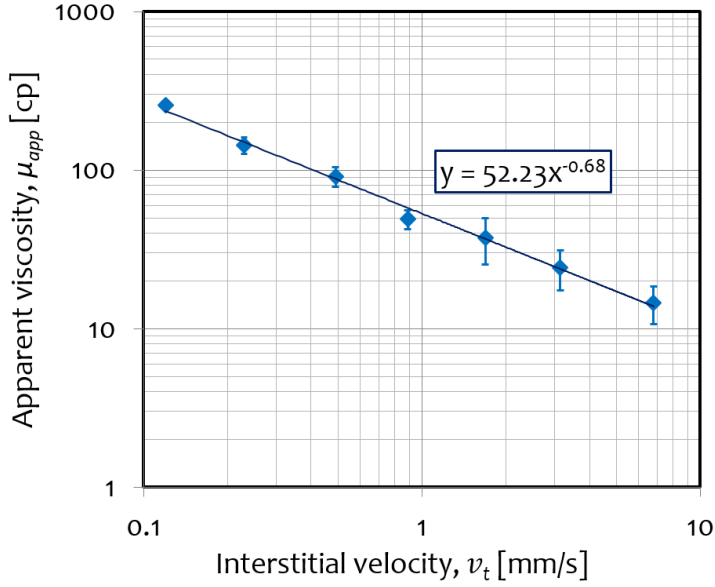


Figure 5.9. Apparent viscosity of LE foam at different total interstitial velocities. The shear-thinning rheology reflects a power-law exponent (Bird et al., 2002) of 0.32.

5.5 Discussion

Gas trapping results from the competition between viscous and capillary forces. In our model fracture, trapped-gas fraction is much less than that usually found in geological porous media and microfluidic models. This reflects the major difference in geometry between fractures and porous media. The trapping of non-wetting phase in porous media is conventionally related to the capillary number:

$$N_{ca} = \frac{\nabla P K}{\gamma \cos \theta} \quad (5.3)$$

where ∇P is the pressure gradient, K is the permeability of porous media, γ is the interfacial tension, and θ is the contact angle.

The geometry of the fracture pore space affects the mechanism of gas trapping in ways different from other porous media. AlQuaimi and Rossen (2018a) formulated a new capillary number N'_{ca} (Eq. 5.4) by adding a term (in brackets) to account for the effects of pore-space geometry of fracture on trapping of non-wetting phase.

$$N'_{ca} = \left(\frac{\nabla P K}{\gamma \cos \theta} \right) \left[\left(\frac{12}{2} \right) \left(\frac{d_t}{d_H} \right)^2 \left(\frac{L_t}{d_t} \right) \frac{1}{1 - \left(\frac{d_t}{d_b} \right)} \right] \quad (5.4)$$

where d_t , d_b and L_t are typical pore-throat aperture, typical pore-body aperture, and typical pore length, respectively, determined from the spatial distribution of aperture in the fracture. d_H is the hydraulic aperture.

Figure 5.10 shows trapped-gas fraction as a function of the new capillary number. Data apart from the blue diamonds are from the non-wetting phase desaturation experiments of AlQuaimi

and Rossen (2018a) using model fractures with a variety of geometries. The blue data are our experimental results for trapped-gas fraction. They correlate well with the predictions using the new capillary number. The agreement is good despite at least two differences between our results and the assumptions of AlQuaimi and Rossen (2018a). They assumed a non-wetting droplet of about pore size trying to get through the pore throat; our bubbles are smaller. They also assumed isolated non-wetting droplets immersed in the wetting phase. In our case the individual lamellae between bubbles are not as tightly curved as they pass through pore throats as in that case. Despite the fact that the bubble distribution of foam in our study is different from a single droplet immersed in water in the study of AlQuaimi and Rossen (2018a), we believe that geometric factors (typical pore-body and pore-throat apertures, ratio of throat to body aperture, etc.) that differ from one fracture to another would have a similar effect on the mobilization of trains of bubbles as on a single droplet. Nevertheless, this agreement testifies that viscous force is more significant compared to capillary force at our experimental conditions, hence yielding a small fraction of trapped gas in the fracture. The agreement between our results and this correlation suggests that the correlation could apply to fractures with other aperture distributions.

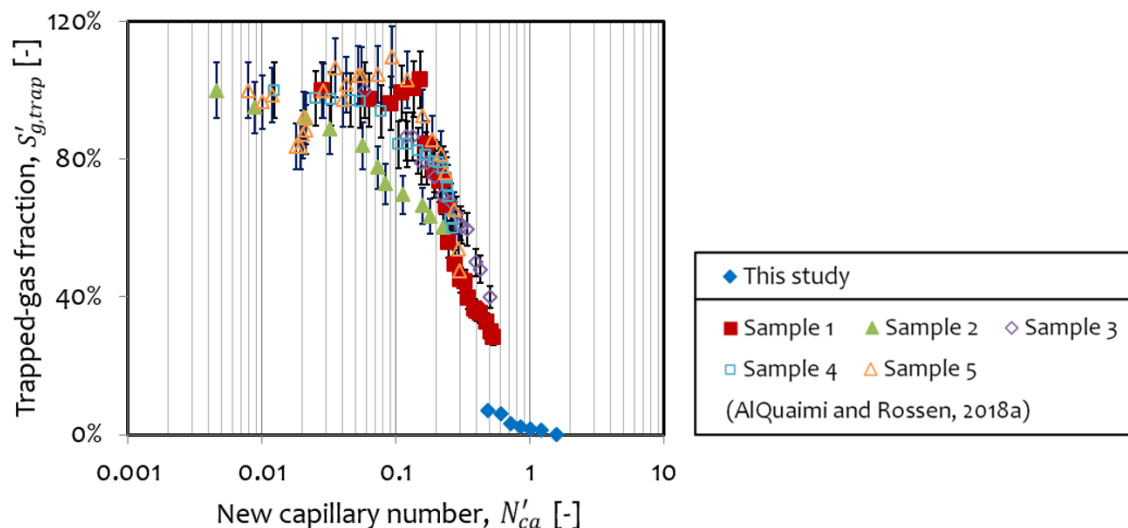


Figure 5.10. Trapped-gas fraction as a function of new capillary number. The standard deviation of the blue data is smaller than the scale of the symbol.

5.6 Conclusions

In this chapter, we investigate gas trapping and foam mobility in one model fracture with a pore-space geometry. We find that pre-generated foam is further refined after being injected into the model fracture, mainly by lamella division. Foam reaches local equilibrium, where the rate of bubble creation equals that of bubble destruction, within our 1-m-long model fracture. In the last three sections of the fracture, foam has the same texture and apparent viscosity. In addition, foam texture is finer with increasing total interstitial velocity, because more in-situ foam generation takes place at greater pressure gradient. The fraction of trapped gas decreases as velocity increases. However, the trapped-gas fraction found in our model fracture (less than 7%) is much lower than usually reported for either geological porous media or microfluidics.

At such low trapped-gas fraction, the effect of gas trapping on foam mobility is expected to be relatively insignificant. The results of trapped-gas fraction in our study correlate well with the capillary-number correlation of AlQuaimi and Rossen (2018a). Using this correlation, one could predict the extent of gas trapping in fractures of other geometries or at other velocities or pressure gradients.

6 Effects of Gravity on Foam in Model Fractures⁴

6.1 Introduction

In this chapter, we report a series of foam experiments in three model fractures with the same irregular roughness (Fig. 2.4) but different hydraulic apertures. Models B, C and D have a hydraulic aperture of 78, 98 and 128 μm . Their spatial properties are provided in Table 2.1. To investigate the effects of gravity on foam, we conduct experiments by horizontal injection in the three model fractures placed horizontally and sideways, i.e. with the model fractures turned on their long side, and in Model B placed vertically with injection upward or downward. We quantify foam texture and gas saturation to show how foam behaves in all three model fractures and we discuss how hydraulic aperture affects foam strength. In addition, we examine the effects of gravity on foam in sideways-placed fractures and we report how gas saturation varies at different heights of the fracture. We also compare how the influence of gravity differs between three model fractures with different hydraulic apertures.

6.2 Experiments and image analysis

Table 6.1 shows the eight experiments conducted in this chapter. We study foam by placing the fractures horizontally and sideways (turning the fracture on its long side). In particular, besides the sideways-flow experiment, we also place Model B vertically to study the effects of gravity. In Experiment 6.2, we inject foam upward. Afterward, we turn the model over and carry out Experiment 6.3 by injecting foam downward.

Experiment	Model fracture	Hydraulic aperture, μm	Model placement	Flow direction
6.1			Horizontally	Horizontal
6.2	Model B	78	Vertically	Upward
6.3	(irregular roughness)		Vertically	Downward
6.4			Sideways	Sideways
6.5	Model C	98	Horizontally	Horizontal
6.6	(irregular roughness)		Sideways	Sideways
6.7	Model D	128	Horizontally	Horizontal
6.8	(irregular roughness)		Sideways	Sideways

Table 6.1. Experiments conducted in this chapter.

⁴ This Chapter is based on Li, K., Wolf, K. H. A., and Rossen, W. R. 2021. Effects of Gravity on Foam Behaviour in Roughened Model Fractures. *SPE Journal*. <https://doi.org/10.2118/206735-PA>.

In all experiments, we pre-generate foam at foam quality f_g of 0.8, and at the total interstitial velocity v_t of 1 mm/s. Despite considerable foam coarsening by diffusion between the mixing tee and the fracture inlet, the pre-generated foam flows into the model fractures as relatively large bubbles instead of slugs. Foam texture is further refined during flow within the model fracture. Seven pressure transducers are used to measure the pressure at different locations along the model fracture (Fig. 5.1). We calculate the steady-state time-averaged pressure gradient ∇P_{foam} to quantify the strength of the steady-state foam. We also compute the standard deviation (SD) of steady-state pressure gradients to characterize the variability of our experimental results.

We take multiple images at different times and different locations in each section of the model fracture (Fig. 5.1) after each experiment reaches steady-state. We use ImageJ software to process and analyze the images to compute bubble density and bubble size. The calculated foam properties are time- and location-averaged. In Experiments 6.1, 6.2 and 6.3 on Model B, we program a macro to calculate the velocity of the gas-bubble train. Multiple time-lapse images during a 47-s period are processed. The macro identifies bubbles with a displacement greater than the average bubble diameter as flowing bubbles. The velocity of each flowing bubble is computed by the macro and is composed of a longitudinal (along the fracture) and a transverse vector (across the fracture). The transverse vector reflects the tortuosity of flow channels in the model fracture as well as the effects of gravity. We estimate the velocity of the gas-bubble train as the average longitudinal velocity of all flowing bubbles.

We use the technique reported in Section 5.2 to estimate the area fraction of the trapped gas $S'_{g,trap}$, and we relate it to the effects of gravity and hydraulic aperture of the model fractures. We also compute the 2D gas area fraction of the foam by:

$$S_g^{2D} = \frac{A_{g,total}}{A_{image}} \quad (6.1)$$

where $A_{g,total}$ is the total area of gas within the region of one image, and A_{image} is the area of the image.

In our model fractures with uneven distribution of aperture, gas, trapped or flowing, tends to occupy locations of wider aperture, and water occupies locations with narrower aperture. We use the aperture distribution of the three model fractures (Fig. 2.6) to convert S_g^{2D} to 3D gas saturation of foam. Figure 6.1 shows the conversion for the three model fractures. In addition, we compute water-occupied area fraction and use the technique reported in Section 3.3 to relate it to aperture distribution of the model fractures to estimate the local aperture d_a at water-gas interfaces, by which we estimate capillary pressure of foam using Eq. 3.6.

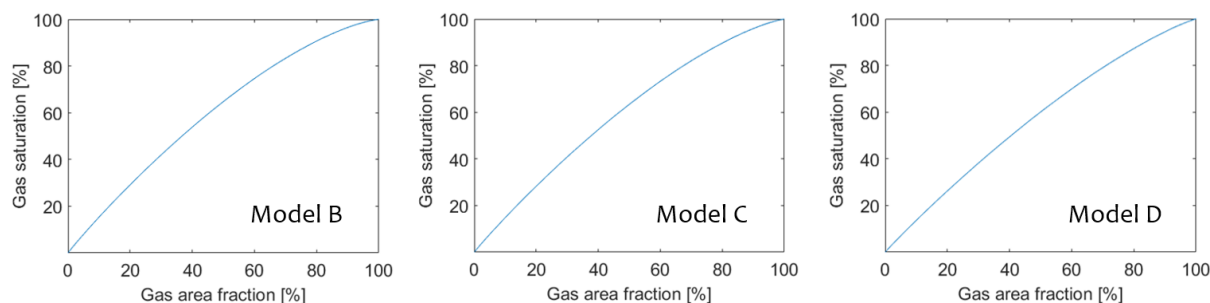


Figure 6.1. Conversion of gas area fraction to gas saturation for Models B, $d_{H_A}=78 \mu\text{m}$ (left), C, $d_{H_B}=98 \mu\text{m}$ (middle), and D, $d_{H_C}=128 \mu\text{m}$ (right).

6.3 Gravity effects on foam in vertical-flow experiments

We conducted Experiment 6.1 in Model B by placing the fracture horizontally, where foam is not affected by gravity. Figure 6.2 shows bubble density, bubble size and pressure gradient of the steady-state foam in different sections of the model fracture.

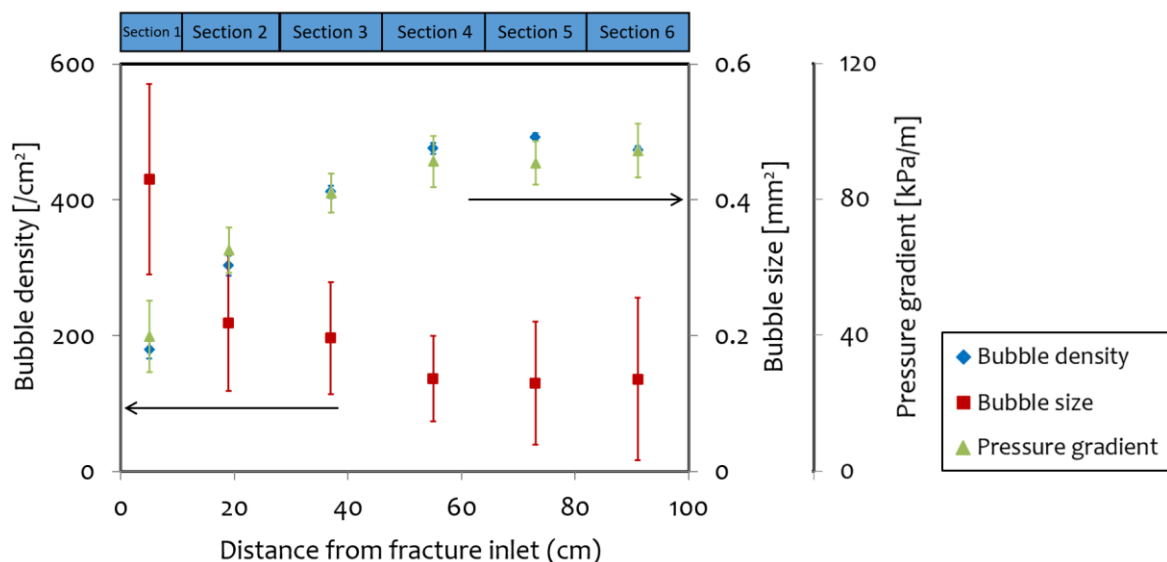


Figure 6.2. Bubble density, bubble size and pressure gradient of foam in different sections of Model B ($d_{H_B}=78 \mu\text{m}$) in Experiment 6.1 (horizontal orientation).

Although mesh size of the frit filter in the mixing tee upstream of the model fracture is $10 \mu\text{m}$, foam has coarsened into relatively large gas bubbles by the time it enters the fracture. As shown in Fig. 6.2, the bubble density increases and bubble size decreases along the fracture, indicating that the pre-generated foam is further refined as it propagates in the fracture. As in the experiments in Chapter 5, in experiments of this chapter we observe that, by injecting pre-generated foam, lamella division is the principal mechanism of in-situ foam generation. As a result of finer and stronger foam, the pressure gradient also increases. In Experiment 6.1, we study foam at different times after foam reaches steady-state to compute the standard deviation of bubble density. We average the standard deviation of bubble size in each section at different times. The large standard deviation of bubble size indicates that foam bubbles in our model

fracture are polydisperse. In the last three sections, foam texture reaches a stable and constant state with bubble density of 481 per cm^2 and bubble size of 0.135 mm^2 . The pressure gradient is also the same in the last three sections at approx. 92 kPa/m . We conclude that foam has achieved local equilibrium (LE) in Model B (Ettinger and Radke, 1992; Ashoori et al., 2010; Chen et al., 2010).

To study the effects of gravity, we place Model B vertically in Experiments 6.2 and 6.3. Before injecting foam, we clean the fracture with demineralized water, then vacuum and pre-saturate the fracture with surfactant solution. We then zero all seven pressure transducers, which means that measured pressures exclude the hydrostatic potential of the water in the fracture. Fig. 6.3 shows how measured pressure gradient evolves along the fracture for the three experiments. Experiment 6.2 (upward-flow) and Experiment 6.3 (downward-flow) also reach LE in the last three sections, where the pressure gradient reaches a stable magnitude. The LE pressure gradients (averaged across the last three sections) of both experiments are close to that of horizontal-flow experiment.

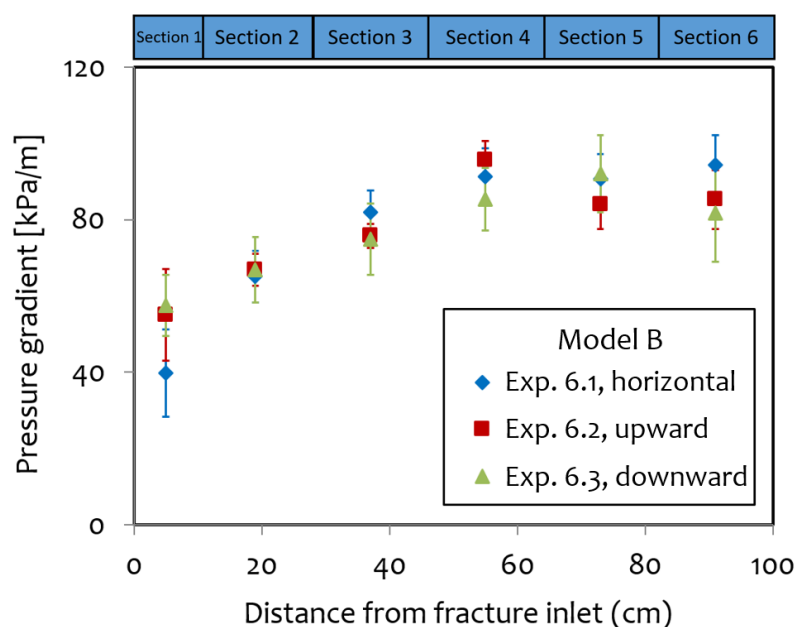


Figure 6.3. Pressure gradient of Experiments 6.1, 6.2 and 6.3 in Model B ($d_{H_B}=78 \mu\text{m}$).

In the rest of this chapter, we examine foam in the last three sections, where foam is at LE, unless otherwise indicated. We examine foam at different times and at different locations in the last three sections to compute the standard deviation (SD) of LE foam properties. Table 6.2 compares LE foam properties in Model B for Experiments 6.1, 6.2 and 6.3. In the vertical-flow experiments, Experiment 6.2 creates a finer-texture foam than Experiment 6.3. When the fracture stands vertically, water tends to accumulate in lower sections due to gravity. As a result, sections near the inlet of Experiment 6.2 are in a wetter state, which benefits in-situ foam generation (Rossen, 1996). In contrast, in Experiment 6.3, the inlet is located at the top of the fracture, where a drier condition is present. Events of lamella creation are reduced because of relatively drier conditions. Despite the different foam texture between upward-flow and

downward-flow experiments, the LE pressure gradient (excluding the hydrostatic potential of water) is not significantly affected.

Experiment (Model B)	Pressure gradient, kPa/m	SD	Bubble density, /cm ²	SD	Bubble size, mm ²	SD	Gas saturation, %	SD	Trapped gas fraction, %	SD	Velocity of bubble trains, mm/s
Exp. 6.1 (Horizontal)	92.1	7.3	481	31	0.135	0.008	78.3	1.3	4.2	0.3	0.98
Exp. 6.2 (Upward)	88.3	6.4	474	50	0.136	0.011	79.0	2.8	3.3	0.2	1.18
Exp. 6.3 (Downward)	86.4	10.4	354	25	0.178	0.030	78.0	6.0	6.0	0.6	0.84

Table 6.2. Properties of LE foam of Experiments 6.1, 6.2 and 6.3 in Model B ($d_{H_B}=78 \mu\text{m}$).

The fact that measured pressure gradient is similar in all three cases suggests that the potential gradient required for foam flow closely matches that of the water phase. On the other hand, one would expect a smaller potential gradient with larger bubbles (downward flow). The flow potential of a foam, with density less than that of water, might be somewhat less than that of water, reflected in our measured pressure differences. The combination of these two effects might explain why the measured pressure gradient for downward flow is so close to the other two values.

The trapped-gas fraction is also affected by gravity. Experiment 6.3 traps 6% of gas in pore bodies and Experiment 6.2 traps 3.3%. When foam flows downward in Experiment 6.3, the gravitational potential of gas (10 kPa/m), together with capillarity, hinders foam bubbles from flowing downward. In Experiment 6.2, the gravitational potential helps overcome the capillarity and moves bubbles upward, hence trapping less gas.

Despite the small trapped-gas fractions, the effect of gravity on the velocity of foam bubble trains is not significant. The velocities of bubble trains for the three experiments are all close to 1 mm/s. The calculated velocity is number-averaged based on all flowing bubbles. In this foam, smaller bubbles, much smaller than pore size, propagate faster due to less resistance. For bubbles as large as, or larger than, pores, relatively smaller bubbles would be expected to show greater resistance to flow (Falls et al., 1989). Although the velocity of bubble trains is computed from the number average velocity for all moving bubbles, big or small, we believe that it provides a useful indication of the properties of the flowing gas fraction.

6.4 Gravity effects on foam in sideways-flow experiments

In Experiment 6.4, we place Model B on its long side and inject foam sideways. Figure 6.4 shows that the pressure gradient of Experiment 6.4 is equivalent to Experiment 6.1, indicating that stable foam is also created in Experiment 6.4 when Model B stands on its side.

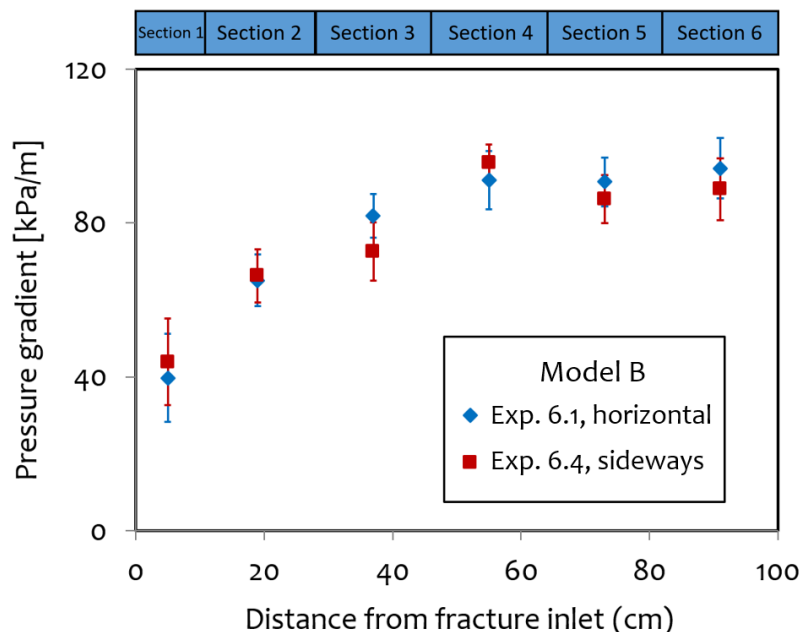


Figure 6.4. Pressure gradient of Experiments 6.1 and 6.4 in Model B ($d_{HB}=78 \mu\text{m}$).

In the sideways-flow experiments, we measure foam properties at the bottom, middle and top of each section, which locate at a height of 0, 7.5 and 15 cm of the fracture, respectively. Figure 6.5 shows bubble density and bubble size at various positions within the sections. Figure 6.6 shows processed images of foam. These images are representative of multiple images taken in the same locations and at different times.

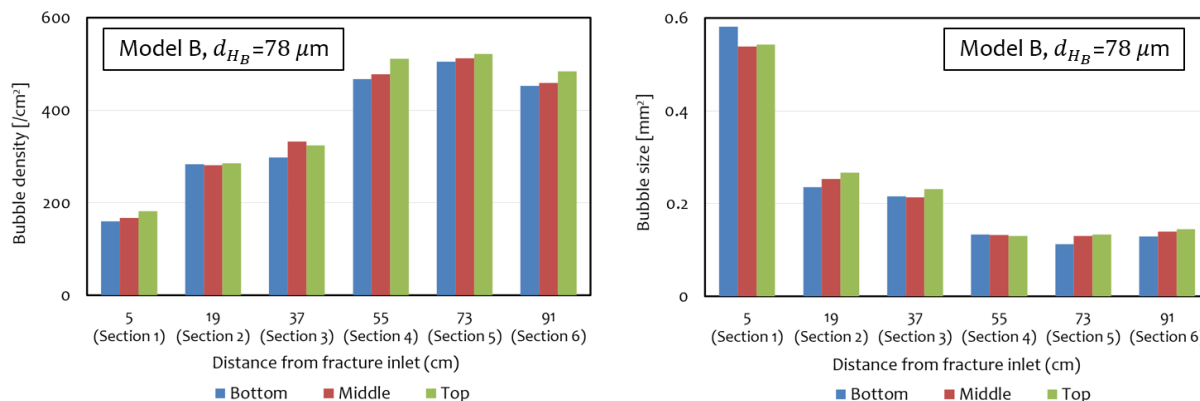


Figure 6.5. Bubble density (left) and bubble size (right) of foam in different sections and at different heights of Model B in Experiment 6.4 (sideways orientation).

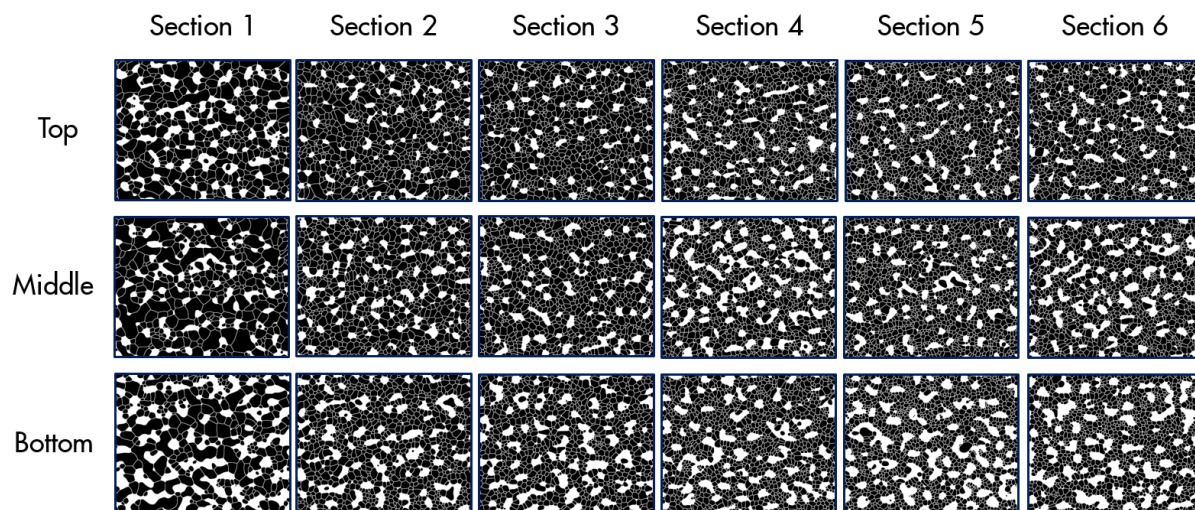


Figure 6.6. Processed images of foam in different sections and at different heights of Model B ($d_{HB} = 78 \mu\text{m}$) in sideways orientation. Images are taken at locations shown as red squares on the fracture in Fig. 5.1. Gas is shown in black, liquid in white. Liquid occupies areas with narrow aperture in the model fracture. Image size: $19.5 \times 15.6 \text{ mm}$.

Figure 6.5 shows that foam gets finer as it propagates in Model B. In section 1, foam along the height of the fracture is uniform with properties similar to those in the horizontal-flow experiment (Fig. 6.2): bubble density of 180 per cm^2 and bubble size of 0.43 mm^2 . We inject the same pre-generated foam into the fracture in both horizontal-flow and sideways-flow experiments. In the last three sections, both bubble density and bubble size increase modestly with elevation within the fracture. This suggests that some foam bubbles flow toward the top of the fracture under gravity. Figure 6.7 shows gas saturation within the model. In sections near the inlet, gas saturation is also reasonably uniform along the height of the fracture. As foam propagates, some gravity segregation takes place: drier foam flows at the top and wetter foam at the bottom. In the last two sections, gas saturation is more than 10% drier than at the bottom.

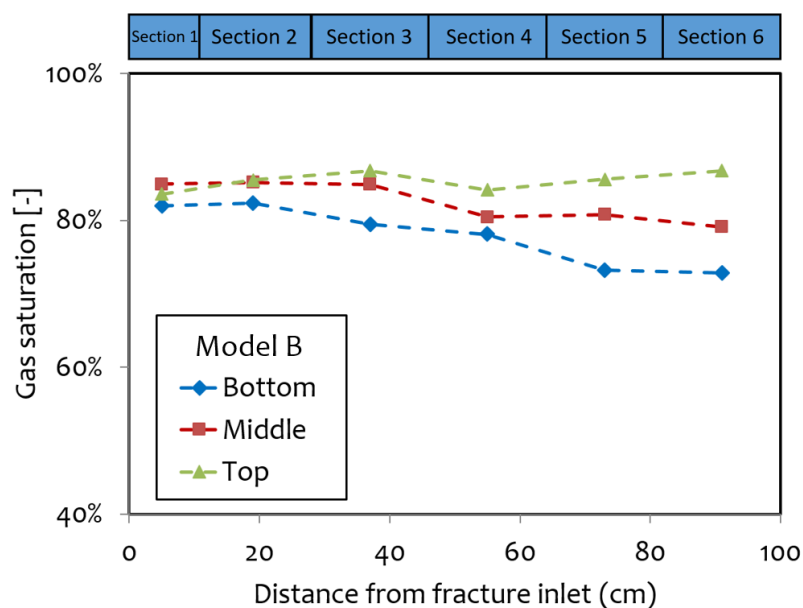


Figure 6.7. Gas saturation of foam in different sections and at different heights of Model B ($d_{H_B}=78 \mu\text{m}$) in Experiment 6.4 (sideways orientation).

Thus in Model B, foam is affected by gravity. Water and gas start to segregate as foam flows along the fracture. However, water and gas are not completely segregated in Model B (Fig. 6.6). With a hydraulic aperture of $78 \mu\text{m}$ and a height of 15 cm, foam is still in the capillary transition zone in this model fracture.

6.5 Effects of hydraulic aperture on foam in horizontal-flow experiments

In NFRs, an open fracture can have an aperture of hundreds of microns or more (Luthi and Souhaite, 1990). In this Section, we examine the effects of hydraulic aperture on foam in the three model fractures (Models B, C and D) with the same irregular roughness, but different hydraulic apertures of 78, 98 and $128 \mu\text{m}$, respectively. We conduct foam experiments on all three models by placing them horizontally. Figure 6.8 shows pressure gradients of Experiments 6.1, 6.5 and 6.7 in Models B, C and D. In all three model fractures, foam is stable and reaches local equilibrium in the last three sections, with a roughly uniform pressure gradient.

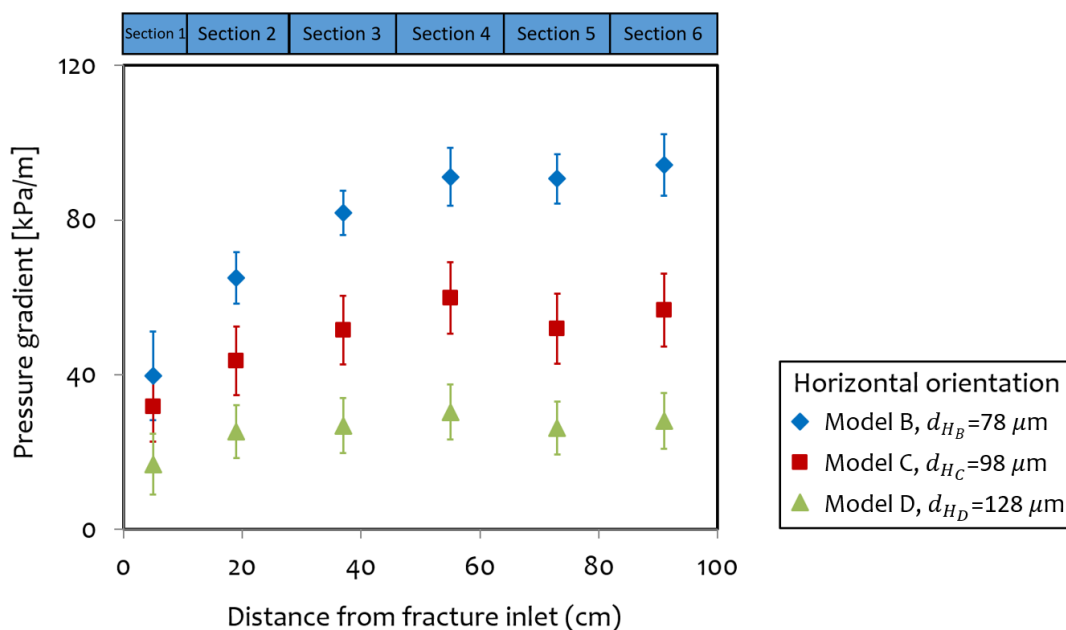


Figure 6.8. Pressure gradient of Experiments 6.1, 6.5 and 6.7 in Models B, C and D (horizontal orientation).

As shown in Fig. 6.8, the pressure gradient decreases as the hydraulic aperture of the fracture increases from Model B to Model D, indicating a weakening foam. As the aperture increases, the curvature of lamellae passing through pore throats in the fracture becomes smaller. Thus, less viscous force is required to overcome the capillary force, in order to move the foam bubbles.

Table 6.3 shows foam properties of the three experiments. Foam is much coarser in models with a larger aperture. In our model fractures, the pore throats are roughly in the shape of a slit.

The aspect ratio of the pore throat, $\frac{d_t}{w_t}$, of the three model fractures is 0.12, 0.14 and 0.18, respectively (Table 2.1). AlQuaimi and Rossen (2018b) argued that a smaller $\frac{d_t}{w_t}$ facilitates foam generation by snap-off at the throats. During initial drainage, more bubbles are also created in the fracture with a smaller ratio of pore-throat aperture to pore-body aperture, $\frac{d_t}{d_b}$, due to the drop in capillary pressure as a gas-water interface advances from the throat to the body (Rossen, 1996). During steady flow, a smaller fluctuation in local capillary pressure produces snap-off. Table 2.1 shows that both $\frac{d_t}{w_t}$ and $\frac{d_t}{d_b}$ increase from Model B to Model D. As the hydraulic aperture increases, less foam generation occurs: thus coarser foam. The contrast in bubble volumes is greater than the contrast in areas shown in Table 6.3, since Model D has larger hydraulic aperture as well as larger bubble area.

Experiment (Horizontal)	Hydraulic aperture, μm	Pressure gradient, kPa/m	SD	Bubble density, / cm^2	SD	Bubble size, mm^2	SD	Gas saturation, %	SD	Trapped gas fraction, %	SD
Exp. 6.1 (Model B)	78	92.1	7.3	481	31	0.135	0.008	78.3	1.3	4.2	0.3
Exp. 6.5 (Model C)	98	56.2	9.2	376	16	0.156	0.010	77.3	2.7	1.2	0.5
Exp. 6.7 (Model D)	128	28.2	7.0	200	6	0.313	0.021	79.3	2.1	0.0	0.0

Table 6.3. Properties of LE foam of Experiments 6.1, 6.5 and 6.7 in Models B, C and D (horizontal orientation).

In Model D, the lamella density per unit of length is smaller due to a coarser foam compared to the other two models. The resistance on the foam flow is therefore reduced (Hirasaki and Lawson, 1985). As a result, Model D creates the weakest foam with the lowest pressure gradient.

In addition, the trapped-gas fraction also decreases as the hydraulic aperture increases. The ratio of pore-throat aperture to pore-body aperture increases from Model B to Model D, signifying that the effect of capillary pressure on gas trapping is less pronounced. In Model D, there is no gas trapping. Viscous force dominates foam flow.

6.6 Effects of hydraulic aperture on gravity segregation in sideways-flow experiments

To further study the effects of gravity on foam, we conduct sideways-flow experiments in Models C and D by placing the model fractures on their long sides. Table 6.4 compares foams in section 2 of the fractures (near the inlet) for experiments with different fracture orientations. For both model fractures, in sideways-flow experiment, foam texture at different heights in section 2 of the fracture is reasonably uniform, indicating that gravity effects on foam near the inlet are insignificant. In addition, foam texture in the sideways-flow experiment is similar to that in horizontal-flow experiment, implying that we inject the same pre-generated foam into the model fracture, despite the orientations.

Experiment	Hydraulic aperture, μm	Location where foam is studied	Bubble density, $/\text{cm}^2$	Bubble size, mm^2
Exp. 6.5 (Model C, horizontal)	98	Section 2	284	0.238
Exp. 6.6 (Model C, sideways)	98	Bottom in section 2	271	0.266
		Middle in section 2	279	0.242
		Top in section 2	291	0.249
Exp. 6.7 (Model D, horizontal)	128	Section 2	153	0.430
Exp. 6.8 (Model D, sideways)	128	Bottom in section 2	141	0.455
		Middle in section 2	151	0.439
		Top in section 2	134	0.473

Table 6.4. Properties of foam in section 2 of Models C and D in experiments with different fracture orientations.

Figure 6.9 shows processed images of foam in different sections of Models C and D. Figures 6.10 and 6.11 show bubble density and bubble size of foam in the two model fractures. Figure 6.12 shows average bubble density and bubble size of foam (averaged across the last three sections) at different heights of all three model fractures.

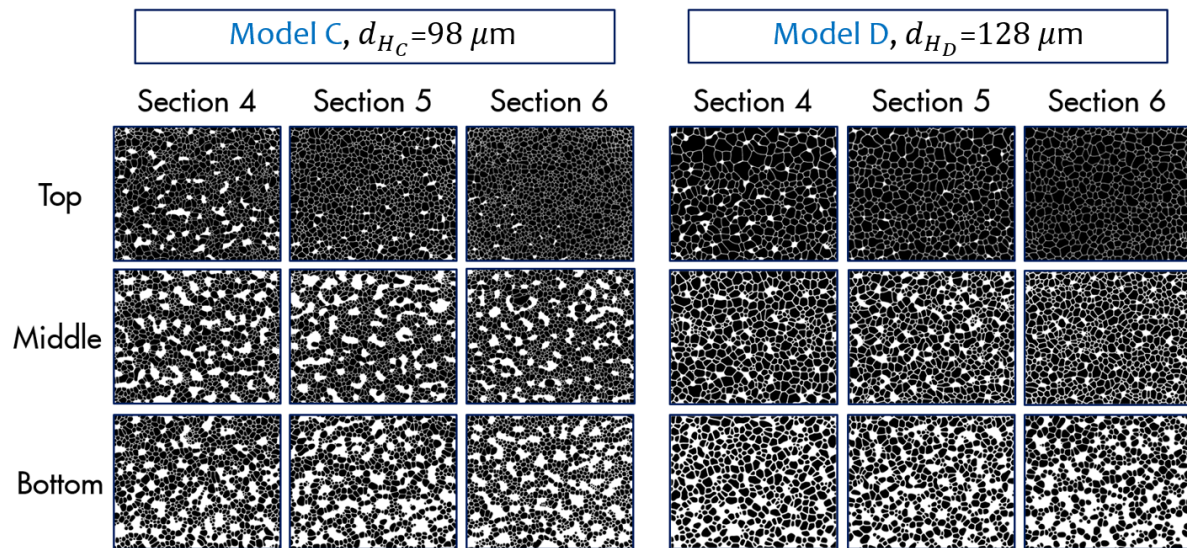


Figure 6.9. Processed images of foam in different sections and at different heights of Model C with $d_{H_C}=98 \mu\text{m}$ (left) and Model D with $d_{H_D}=128 \mu\text{m}$ (right) in sideways orientation. Gas is shown in black, liquid in white. Liquid occupies areas with narrow aperture in the model fracture. Image size: $19.5 \times 15.6 \text{ mm}$.

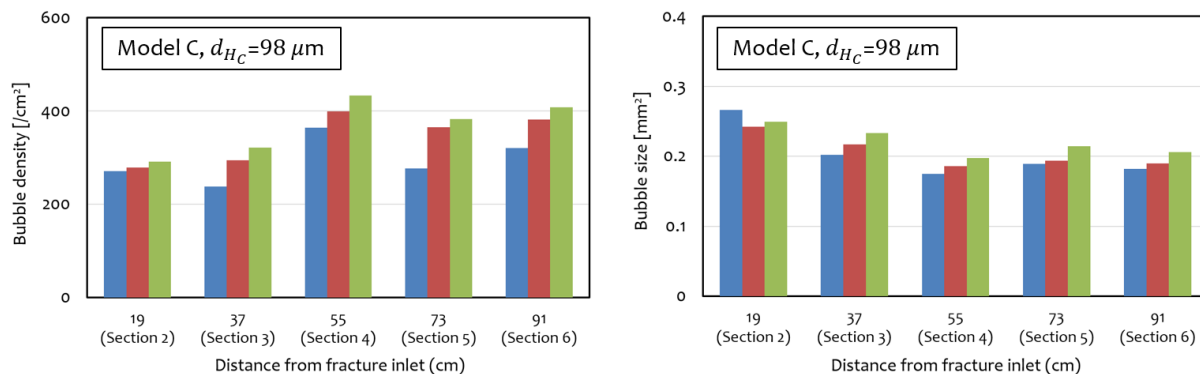


Figure 6.10. Bubble density (left) and bubble size (right) of foam in different sections and at different heights of Model C in Experiment 6.6 (sideways orientation).

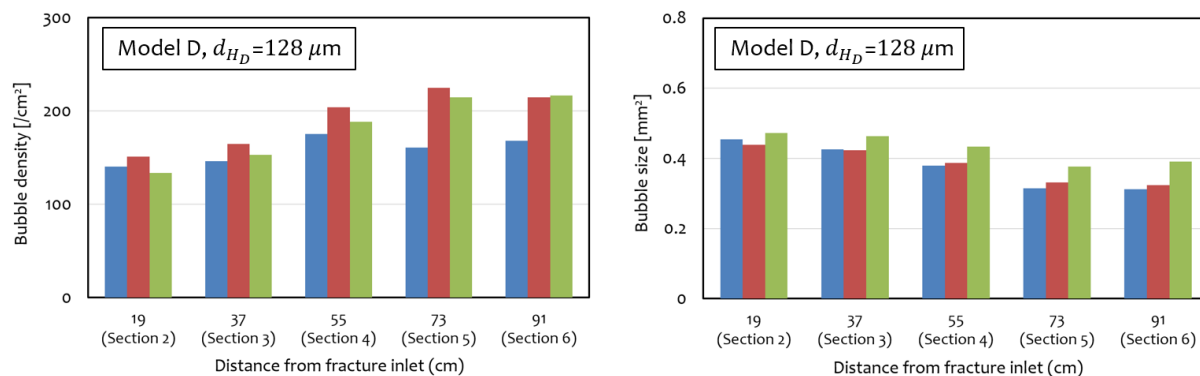


Figure 6.11. Bubble density (left) and bubble size (right) of foam in different sections and at different heights of Model D in Experiment 6.8 (sideways orientation).

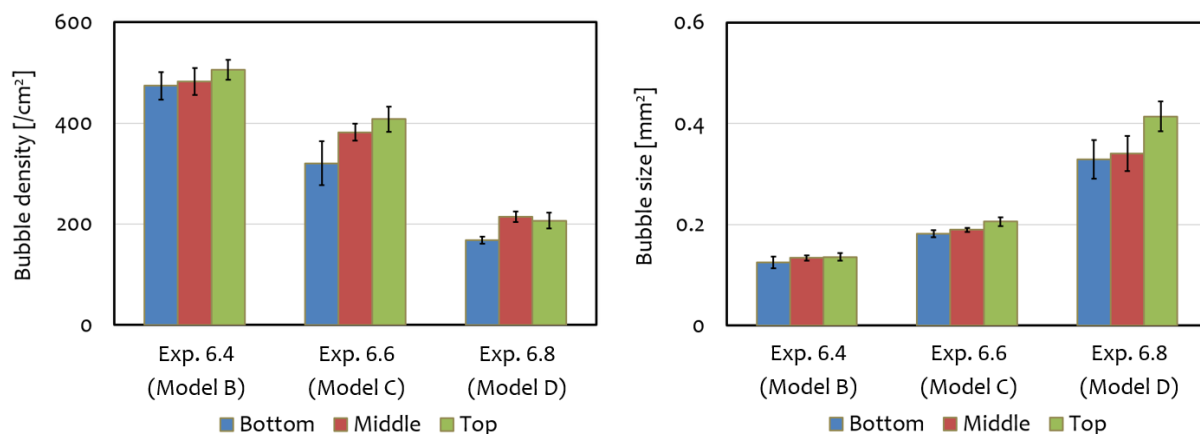


Figure 6.12. Bubble density (left) and bubble size (right) of foam (averaged across the last three sections) at different heights of Models B ($d_{H_B} = 78 \mu\text{m}$), C ($d_{H_C} = 98 \mu\text{m}$) and D ($d_{H_D} = 128 \mu\text{m}$) in Experiments 6.4, 6.6 and 6.8 (sideways orientation).

In Models B and C, bubble density of foam is greater at the top of the fractures. Foam bubbles tend to flow upward due to gravity in all three fractures, except Model D. However, the

difference of bubble density along the height of Model D is not significant. This could reflect the 24% larger bubble size (2D area) at the top of Model D than at the middle and the bottom. The larger bubble size means fewer bubbles per unit area of the foam.

Figure 6.13 shows gas saturation of foam in different sections and at different heights of Models C and D. As in Model B (Fig. 6.7), water and gas also segregate as foam propagates in Models C and D. As the hydraulic aperture increases from 78 to 98 to 128 μm , segregation increases along the fracture. As the aperture increases, the influence of the capillarity on the foam recedes. The effects of gravity increase, and, as a result, gravity segregation is greater.

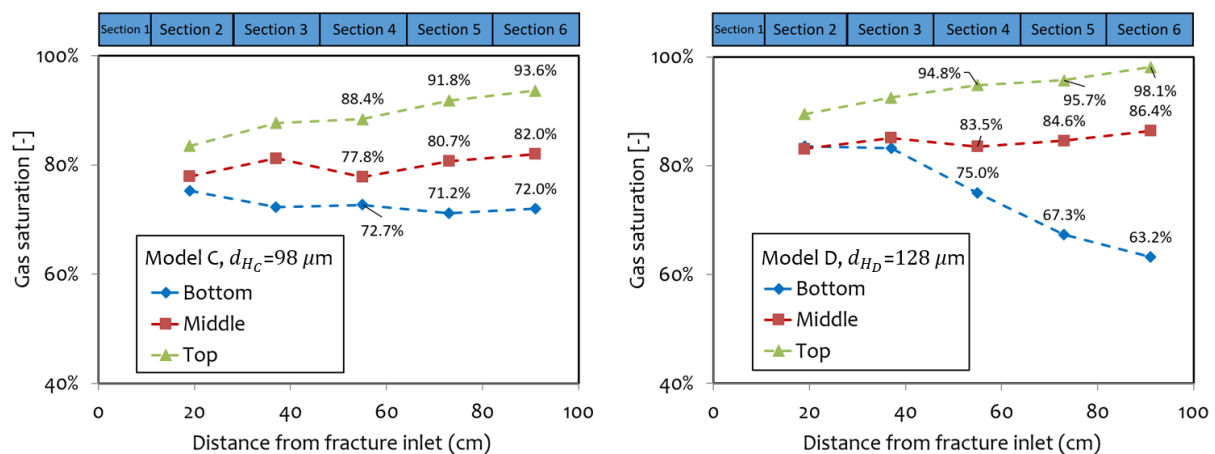


Figure 6.13. Gas saturation of foam in different sections and at different heights of Models C (left) and D (right) in sideways orientation.

Figure 6.14 compares gas saturation (averaged across the last three sections) at different heights of the three model fractures. In all three models, drier foam flows along the top of the fracture, and wetter foam at the bottom. The saturation at the top is 27.7%, 19.3% and 10.8% greater than at the bottom for Models D, C and B, respectively. Despite the gravity segregation in all three model fractures, water and gas are still not completely segregated, either at the top or the bottom (Figs. 6.6 and 6.9).

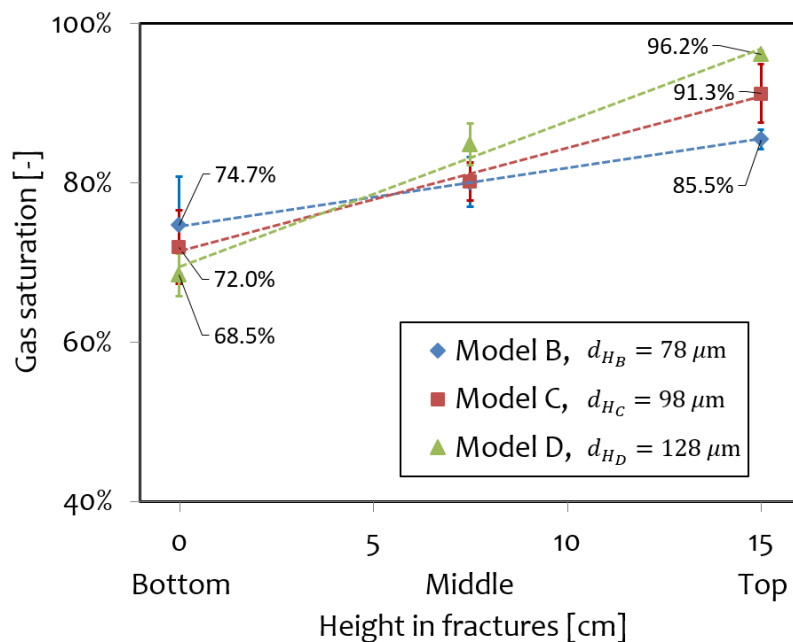


Figure 6.14. Gas saturation (averaged across the last three sections) at different heights of Models B, C and D in Experiments 6.4, 6.6 and 6.8 (sideways orientation).

In all sideways-flow experiments, we did not observe significant bubble destruction by capillary coalescence. At top of the fractures, the capillary pressure estimated from Eq. 3.6 is 1.12, 0.99 and 0.79 kPa for Models B, C and D, respectively. The hydrostatic potential of a 15-cm-high water column is 1.47 kPa. Though foam is affected by gravity in all sideways-flow experiments (with greater segregation with increasing aperture), all three models represent a capillary transition zone.

6.7 Discussion

In this chapter, we have reported eight foam experiments in model fractures with different orientations. Each model in our experiments represents a single open geological fracture, with no flow interaction with adjacent matrix. In horizontal-flow experiments with no gravity effects, foam gets coarser as hydraulic aperture increases. This seems to contradict the understanding of foam in porous media where stronger foam is created in high-permeability zones. In porous media, capillary pressure would be much greater than what we estimate in our model fractures (Behrenbruch et al., 2016). In low-permeability zones in porous media, high capillary pressure restrains foam generation and accelerates coalescence. As a result, stronger foam created in high-permeability zones diverts gas into low-permeability zones. In our model fractures, foam is stable in all three model fractures, with much lower capillary pressure compared to porous media. In model fractures with larger hydraulic aperture, less in-situ foam generation takes place, thus creating a weaker foam. Despite this fact, foam reaches LE in all three fractures. In addition, the pressure gradient seen in our horizontal-flow experiments (Fig. 6.8) suggests that foam similar to ours would benefit the diversion of gas from fractures into matrix in fractured reservoirs (Farajzadeh et al., 2010).

In experiments with the model on its long side, we observed segregation in all three fractures. The segregation increases as foam flows through all our three model fractures. Our model fractures (1-m-long and 15-cm-wide) are much smaller in dimension than geological fractures in NFRs. The extent of gravity segregation seen in our experiments suggests that foam in vertical natural fractures (meters tall and tens of meters long, often with much greater aperture) is problematic. As a result of gravity segregation, foam's capacity to divert gas in a tall fracture over large distances will be weakened.

Skoreyko et al. (2012) developed a foam model to simulate gas mobility control as a function of foam quality, foam degradation, regeneration, interfacial tension reduction and trapped gas in the naturally-fractured Cantarell field. Using this model, they matched laboratory and field data to better understand foam application in the field. Luo et al. (2019) implemented a mechanistic foam model combining foam and microemulsion to history-match oil recovery and pressure drop of foam corefloods in fractured oil-wet rock. The simulation results showed that pre-generated foam greatly resisted the fluid from flowing into the fracture near the injector and enhanced the diversion of injected fluids into the matrix.

As an initial study, the combined effects of gravity and aperture on foam reported in this chapter suggest that gravity segregation or even complete separation of water and gas is a major issue in field application in tall vertical natural fractures over large distances. This thus needs to be taken into account in modeling. The implication of possible dry-out or collapse of foam in fractures needs to be further studied.

6.8 Conclusions

In this chapter, we report a series of experiments to investigate the effects of gravity on foam behavior in three model fractures with the same roughness and different hydraulic apertures. Foam generation and destruction reach local equilibrium in the horizontal-flow experiments in all three model fractures and in the vertical-flow experiments in Model B. In model fracture with a larger hydraulic aperture, foam is coarser due to less in-situ foam generation. In both vertical-flow and sideways-flow experiments, foam is affected by gravity. In vertical-flow experiments with injection from the bottom, a finer-texture foam, with less gas trapping, is created, compared to injection from the top. In sideways-flow experiments, water and gas segregate to some extent as foam flows along the fracture: drier foam flows along the top of the fracture, and wetter foam along the bottom. The segregation is greater as hydraulic aperture increases; gravity becomes more influential as capillary effects weaken with larger aperture. In our experiments, foam is affected by gravity in model fractures with an aperture up to 128 μm . All three models (15 cm wide) represent a capillary transition zone, with greater segregation with increasing aperture. The extent of gravity segregation seen in our experiments suggests that foam in vertical natural fractures (meters tall and tens of meters long, often with much greater aperture) is problematic and could impair foam's capacity to divert gas flow in a tall fracture over large distances.

7 Conclusions and Recommendations

7.1 Conclusions

Foam has many applications in underground settings, such as acid stimulation (Thompson and Gdanski, 1993), aquifer remediation (Portois et al., 2018), and enhanced oil recovery (EOR) (Kovscek and Radke, 1994; Rossen, 1996). In EOR, foam can improve the sweep and increase recovery by reducing the mobility of gas by a factor of hundreds or more (Tang and Kovscek, 2006). In naturally fractured reservoirs (NFRs), foam can also build up a viscous pressure gradient in fractures, and then divert the flow of gas into the matrix, hence delaying gas breakthrough, reducing gas/oil ratio, and improving oil production (Kovscek et al., 1995; Farajzadeh et al., 2010; Haugen et al., 2014). Despite the field successes in NFRs and the major progress in theoretical understanding (Subsections 1.4.1 and 1.4.2), foam application in NFRs is still far less understood than in unfractured porous media.

This dissertation aims to expand our understanding of foam injection in naturally fractured reservoirs through an experimental approach. To this end, we create four 1-m-long, 15-cm-wide glass model fractures (Models A, B, C and D) with different roughness and hydraulic apertures. Each model consists of one smooth plate on top and another plate on bottom with a roughened side facing the top plate. Between the two plates is a slit-like channel representing a single open geological fracture. Model A has regular roughness. Models B, C and D, with increasing hydraulic apertures, have the same irregular roughness. We study the aperture distribution of the model fractures to characterize their geometries as a 2D network of pore bodies and pore throats.

In the experiments, we use a dual-cylinder pump to inject liquids, and a mass-flow controller to inject gas. A mixing tee with a frit filter inside (mesh size: $10\ \mu\text{m}$) is installed upstream of the fracture inlet to pre-generate foam. The pre-generated foam is then injected into the model fractures to reach the steady state. Seven absolute-pressure transducers are mounted at different locations along the model fracture to measure the pressure. We visualize foam in the model fractures using a high-speed camera and quantify its different properties using ImageJ software. In particular, we calculate water saturation and capillary pressure of foam and study diffusive coarsening, gas trapping, and gravity effects on foam in fractures.

In **Chapter 3**, we conduct experiments in Models A and B. We report a novel technique to analyze foam texture, and especially to estimate water saturation and capillary pressure of foam. We conclude that water in foam in our model fractures lies in four locations: water zones at narrow aperture, Plateau borders, lamellae, and water films on glass plates. Water zones and Plateau borders account for almost all the water of foam in model fractures. During redistribution of water and gas in static foam with no bubble flow after shut-in, water flows in and out through the fracture following paths through Plateau borders and water zones. In our model fractures, the decrease in water saturation with time coincides with an increase in capillary pressure, as expected. Capillary pressures are relatively low, which explains why we did not observe much rupture of foam films throughout our experiment.

In **Chapter 4**, we extend the experiments of Chapter 3 to investigate foam coarsening by gas diffusion between bubbles in Models A and B. We conclude that bubble density decreases and average bubble size increases as foam coarsens in model fractures. At the end of the coarsening experiments, either lamellae are in positions of little or no curvature, or the exposed sides of small bubbles wedged into locations of narrow aperture in Model B have an estimated lamella height close to zero. As a result, coarsening stops because bubbles are at equal pressure or slows nearly to a stop because bubbles lose contact through lamellae. Compared to foam injected at a lower foam quality, foam at a higher quality coarsens faster. In drier foam, the Plateau borders are smaller in size at higher capillary pressure. The height of lamellae is thus greater, hence allowing faster gas diffusion.

In **Chapter 5**, we study gas trapping and foam mobility in Model B. We conclude that foam reaches local equilibrium, where the rate of bubble creation equals that of bubble destruction, within our 1-m-long model fracture. Trapped-gas fraction decreases as velocity increases. However, the trapped-gas fraction found in our model fracture (less than 7%) is much lower than usually reported for either geological porous media or microfluidics. At such low trapped-gas fraction, the effect of gas trapping on foam mobility in the model fracture is expected to be relatively insignificant. The results of trapped-gas fraction in our experiments correlate well with the capillary-number correlation of AlQuaimi and Rossen (2018a). Using this correlation, one could predict the extent of gas trapping in fractures of other geometries or at other velocities or pressure gradients.

In **Chapter 6**, we investigate the effects of gravity on foam in Models B, C and D. We conclude that, in model fracture with a larger hydraulic aperture, foam is coarser due to less in-situ foam generation. In both vertical-flow and sideways-flow experiments, foam is affected by gravity. In vertical-flow experiments with injection from the bottom, a finer-texture foam, with less gas trapping, is created, compared to injection from the top. In sideways-flow experiments, water and gas segregate to some extent as foam flows along the fracture. The segregation is greater as hydraulic aperture increases; gravity becomes more influential as capillary effects weaken with larger aperture. The extent of gravity segregation seen in our experiments in a model 1 m long and 15 cm wide suggests that foam in vertical natural fractures (meters tall and tens of meters long, often with much greater aperture) is problematic and could impair foam's capacity to divert gas flow in a tall fracture over large distances.

As an initial study, the results of this dissertation enrich our knowledge of foam in fractures with complex geometries (roughness, varying apertures, orientation, etc.). Our results would also have an application to foam aquifer remediation and CO₂ sequestration.

7.2 Recommendations for future work

In this dissertation, we inject a solution of 1 wt% AOS C14-16 surfactant with zero salinity and nitrogen to create foam. All experiments are conducted at 20°C and atmospheric pressure. For future specific field applications, study with other surfactants with salinities and gases under more-realistic temperature and pressure is imperative.

Like most previous studies (Fernø et al., 2016; Brattekkås et al., 2020), this dissertation investigates foam behavior in model fractures, with no flow interaction between fractures and adjacent matrix. Under water-wet conditions, capillary pressure in the matrix would be much greater than what we estimate in our model fractures in Chapter 3 (Behrenbruch et al., 2016). The capillary interactions with the matrix may imply more coalescence and possibly faster bubble diffusion between bubbles. Capillarity is an important property that affects foam stability, so this topic deserves further study.

In Chapter 4, we study foam coarsening by gas diffusion in the model fractures. The time scale of our experiments (24 hours) is relatively short in terms of field applications. It is then relevant to examine the significance of coarsening in a long process and to verify whether diffusion comes to equilibrium with the generation of new lamellae. We also find that the network of Plateau borders and water zones acts as the paths for water to flow in and out along our fractures during coarsening. In the fractures, Plateau borders and water zones account for almost all the water. During coarsening, water is transported from one side of the fractures to the other to equalize the difference in capillary pressure. The implication of the flow conductivity of the network on this water transport behavior deserves further research. Of course in natural fractures, water transport through and along the matrix is another major factor.

In Chapter 6, our results suggest that gravity segregation or even complete separation of water and gas is a major issue in field application in tall vertical natural fractures over large distances. Future modeling of foam in fractures should take this mechanism into account. It is then worthwhile to further study the implication of possible dry-out or collapse of foam in fractures at greater gas saturations than examined here.

Oil is not used in this dissertation. In unfractured porous media, oil, as a de-foaming agent, can strongly damage the stability of foam under immiscible conditions by different mechanisms (Bernard et al., 1980; Yang and Reed, 1989; Schramm, 1994). Oils with a smaller carbon number have a stronger adverse impact on foam stability than those with a greater carbon number (Andrianov et al., 2012). Kahrobaei et al. (2018) studied the effects of oil on CO₂ foam under miscible conditions in Bentheimer sandstone cores. They found that CO₂ foam still showed good control of gas mobility in the presence of oil under miscible conditions. CO₂ foam at all compositional variations of oil exhibited shear-thinning behavior. As the geometries of unfractured porous media are distinct from that of fractures, it is consequential to understand how oil affects foam in fractures. This also has significance in field applications.

In addition, our glass model fractures are strongly water-wet. In the field, carbonate naturally fractured reservoirs are mostly oil- or mixed-wet (Seethepalli et al., 2004). This would also affect both foam stability in the fracture and the capillary interactions between the fractures and the adjacent matrix. If the fracture is not water-wet in the presence of surfactant, foam stability in the fracture would be greatly reduced. In addition, if the matrix is not water-wet, it might not draw off water from the foam in the fractures and destabilize the foam. The fact that the surfactant in the foam might alter the wettability makes the whole process more complicated (Hirasaki and Zhang, 2003; Gupta and Mohanty, 2008). The effects of wettability therefore deserve further investigation.

In this dissertation, we study foam in model fractures with two kinds of roughness patterns (Figs. 2.3 and 2.4). The roughness of the roughened plate of each model is created by moulding during the manufacturing process. We use a digital microscope to profile the roughness and characterize the aperture distribution of the model fractures. The roughness in our study is not realistic as in geological fractures. We use glass from a manufacturer because a wide variety of different roughness patterns is available. Our overall goal of this research effort (including the study of AlQuaimi and Rossen, 2018b) is, by making model fractures of a wide range of roughness and aperture distributions, to relate these geometrical properties to foam behavior. We therefore recommend a simulation study to build a model that works for a variety of real fracture geometries by taking into account all our studied physics including effects of diffusive coarsening, gas trapping, and gravity on foam.

BIBLIOGRAPHY

- Aguilera, R. 1995. Naturally Fractured Reservoirs, PennWell Pub. Co., Tulsa.
- Allan, J. and Sun, S. Q. 2003, October. Controls on recovery factor in fractured reservoirs: lessons learned from 100 fractured fields. In SPE Annual Technical Conference and Exhibition. OnePetro. <https://doi.org/10.2118/84590-MS>.
- AlQuaimi, B. I. and Rossen, W. R. 2018a. Capillary desaturation curve for residual nonwetting phase in natural fractures. *SPE Journal*, **23**(03), 788-802. <https://doi.org/10.2118/189448-PA>.
- AlQuaimi, B. I. and Rossen, W. R. 2018b. Foam generation and rheology in a variety of model fractures. *Energy & Fuels*, **33**(1), 68-80. <https://doi.org/10.1021/acs.energyfuels.8b02178>.
- AlQuaimi, B.I. and Rossen, W.R. 2019. Study of foam generation and propagation in fully characterized physical-model fracture. *Journal of Petroleum Science and Engineering*, **175**, 1169-1181. <https://doi.org/10.1016/j.petrol.2018.06.025>.
- Alvarez, J. M., Rivas, H. J., and Rossen, W. R. 2001. Unified model for steady-state foam behavior at high and low foam qualities. *SPE journal*, **6**(03), 325-333. <https://doi.org/10.2118/74141-PA>.
- Andrianov, A., Farajzadeh, R., Mahmoodi Nick, M., Talanana, M., and Zitha, P. L. 2012. Immiscible foam for enhancing oil recovery: bulk and porous media experiments. *Industrial & Engineering Chemistry Research*, **51**(5), 2214-2226. <https://doi.org/10.1021/ie201872v>.
- Ashoori, E., Marchesin, D., and Rossen, W. R. 2010, September. Roles of transient and local equilibrium foam behavior in porous media—traveling wave. In ECMOR XII-12th European Conference on the Mathematics of Oil Recovery (pp. cp-163). European Association of Geoscientists & Engineers. <https://doi.org/10.3997/2214-4609.20144931>.
- Balan, H. O., Balhoff, M. T., Nguyen, Q. P., and Rossen, W. R. 2011. Network modeling of gas trapping and mobility in foam enhanced oil recovery. *Energy & Fuels*, **25**(9), 3974-3987. <https://doi.org/10.1021/ef2006707>.
- Behrenbruch, P., Huu, M. T. D., Hoang, T. G., and Bui, K. D. 2016, October. Modelling of drainage capillary pressure: a comparative study of various analytical capillary pressure formulations in matching laboratory results. In SPE Asia Pacific Oil & Gas Conference and Exhibition. Society of Petroleum Engineers. <https://doi.org/10.2118/182469-MS>.
- Bergeron, V. and Radke, C. J. 1992. Equilibrium measurements of oscillatory disjoining pressures in aqueous foam films. *Langmuir*, **8**(12), 3020-3026. <https://doi.org/10.1021/la00048a028>.
- Bernard, G. C., Holm, L. W., and Harvey, C. P. 1980. Use of surfactant to reduce CO₂ mobility in oil displacement. *Society of Petroleum Engineers Journal*, **20**(04), 281-292. <https://doi.org/10.2118/8370-PA>.
- Bird, R., Stewart, W., Lightfoot, E. 2002. Transport Phenomena 2nd edition John Wiley and Sons. New York.
- Bond, D. C. and Holbrook, O. C. 1958. U.S. Patent No. 2,866,507. Washington, DC: U.S. Patent and Trademark Office.
- BP Statistical Review of World Energy. 2021. <https://www.bp.com/content/dam/bp/business-sites/en/global/corporate/pdfs/energy-economics/statistical-review/bp-stats-review-2021-middle-east-insights.pdf>.
- Brattekkås, B., Eide, Ø., Johansen, S. A., Vasshus, S. S., Polden, A. G., and Fernø, M. A. 2020. Foam flow and mobility control in natural fracture networks. *Transport in Porous Media*, **131**(1), 157-174. <https://doi.org/10.1007/s11242-019-01249-3>.
- Brown, S. R. 1987. Fluid flow through rock joints: the effect of surface roughness. *Journal of Geophysical Research: Solid Earth*, **92**(B2), 1337-1347. <https://doi.org/10.1029/JB092iB02p01337>.
- Buchgraber, M., Castanier, L. M., and Kovscek, A. R. 2012, October. Microvisual investigation of foam flow in ideal fractures: role of fracture aperture and surface roughness. In SPE Annual Technical Conference and Exhibition. OnePetro. <https://doi.org/10.2118/159430-MS>.
- Cantat, I., Cohen-Addad, S., Elias, F., Graner, F., Höhler, R., Pitois, O., Rouyer, F., and Saint-Jalmes, A. 2013. Foams: structure and dynamics. OUP Oxford.

- Chen, C. Y., Horne, R. N., and Fourar, M. 2004. Experimental study of liquid-gas flow structure effects on relative permeabilities in a fracture. *Water resources research*, **40**(8). <https://doi.org/10.1029/2004WR003026>.
- Chen, M., Yortsos, Y. C., and Rossen, W. R. 2006. Pore-network study of the mechanisms of foam generation in porous media. *Physical Review E*, **73**(3), 036304. <https://doi.org/10.1103/PhysRevE.73.036304>.
- Chen, Q., Gerritsen, M. G., and Kovscek, A. R. 2010. Modeling foam displacement with the local-equilibrium approximation: theory and experimental verification. *SPE Journal*, **15**(1), 171-183. <https://doi.org/10.2118/116735-PA>.
- Cheng, L., Reme, A. B., Shan, D., Coombe, D. A., and Rossen, W. R. 2000, April. Simulating foam processes at high and low foam qualities. In SPE/DOE improved oil recovery symposium. OnePetro. <https://doi.org/10.2118/59287-MS>.
- Cohen-Addad, S., Hoballah, H., and Höhler, R. 1998. Viscoelastic response of a coarsening foam. *Physical Review E*, **57**(6), 6897. <https://doi.org/10.1103/PhysRevE.57.6897>.
- Conn, C. A. 2015. The characterization and visualization of multi-phase systems using microfluidic devices (Doctoral dissertation).
- Cosentino, L., Coury, Y., Daniel, J. M., Manceau, E., Ravenne, C., Van Lingen, P., Cole, J., and Sengul, M. 2002. Integrated study of a fractured Middle East reservoir with stratiform super-K intervals-part 2: upscaling and dual-media simulation. *SPE Reservoir Evaluation & Engineering*, **5**(01), 24-32. <https://doi.org/10.2118/76642-PA>.
- Dominguez, G. C. 1992. Carbonate reservoir characterization: A geologic-engineering analysis, part I. Elsevier.
- Emília Rosa, M. and Fortes, M. A. 1999. Coarsening of two-dimensional foams confined by walls. *Philosophical Magazine A*, **79**(8), 1871-1886. <https://doi.org/10.1080/01418619908210397>.
- Ettinger, R. A. and Radke, C. J. 1992. Influence of texture on steady foam flow in Berea sandstone. *SPE reservoir engineering*, **7**(01), 83-90. <https://doi.org/10.2118/19688-PA>.
- Falls, A. H., Musters, J. J., and Ratulowski, J. 1989. The apparent viscosity of foams in homogeneous bead packs. *SPE Reservoir Engineering*, **4**(02), 155-164. <https://doi.org/10.2118/16048-PA>.
- Farajzadeh, R., Wassing, B., and Boerrigter, P. 2010, September. Foam assisted gas oil gravity drainage in naturally-fractured reservoirs. In SPE Annual Technical Conference and Exhibition. OnePetro. <https://doi.org/10.2118/134203-MS>.
- Fernø, M. A., Gauteplass, J., Pancharoen, M., Haugen, A., Graue, A., Kovscek, A. R., and Hirasaki, G. 2016. Experimental study of foam generation, sweep efficiency, and flow in a fracture network. *SPE journal*, **21**(04), 1140-1150. <https://doi.org/10.2118/170840-PA>.
- Ferreira, T. and Rasband, W. 2012. ImageJ user guide. ImageJ/Fiji, 1, 155-161.
- Fried, A. N. 1961. The foam-drive process for increasing the recovery of oil. US Department of the Interior, Bureau of Mines.
- Friedmann, F., Chen, W.H., Gauglitz, P.A. 1991. Experimental and simulation study of high-temperature foam displacement in porous media. *SPE reservoir engineering*, **6**(01), 37-45. <https://doi.org/10.2118/17357-PA>.
- Friedmann, F., Hughes, T. L., Smith, M. E., Hild, G. P., Wilson, A., and Davies, S. N. 1997, October. Development and testing of a new foam-gel technology to improve conformance of the Rangely CO₂ flood. In SPE Annual Technical Conference and Exhibition. OnePetro. <https://doi.org/10.2118/38837-MS>.
- Gauglitz, P. A., Friedmann, F., Kam, S. I., and Rossen, W. R. 2002, April. Foam generation in porous media. In SPE/DOE Improved Oil Recovery Symposium. OnePetro. <https://doi.org/10.2118/75177-MS>.
- Gauteplass, J., Chaudhary, K., Kovscek, A. R., and Fernø, M. A. 2015. Pore-level foam generation and flow for mobility control in fractured systems. *Colloids and Surfaces A: Physicochemical and Engineering Aspects*, **468**, 184-192. <https://doi.org/10.1016/j.colsurfa.2014.12.043>.
- Géraud, B., Jones, S. A., Cantat, I., Dollet, B., and Méheust, Y. 2016. The flow of a foam in a two-dimensional porous medium. *Water Resources Research*, **52**(2), 773-790. <https://doi.org/10.1002/2015WR017936>.
- Glazier, J. A., Gross, S. P., and Stavans, J. 1987. Dynamics of two-dimensional soap froths. *Physical Review A*, **36**(1), 306. <https://doi.org/10.1103/PhysRevA.36.306>.
- Gong, J., Vincent-Bonnieu, S., Kamarul Bahrim, R. Z., Che Mamat, C. A., Tewari, R. D., Mahamad Amir, M. I., and Rossen, W. R. 2020. Injectivity of Multiple Slugs in Surfactant Alternating Gas Foam EOR: A CT Scan Study. *SPE Journal*. <https://doi.org/10.2118/199888-PA>.

- Groenenboom, J., Kechut, N. I., and Mar-Or, A. 2017, October. Foam-assisted WAG: Injection strategies to optimize performance. In SPE/IATMI Asia Pacific Oil & Gas Conference and Exhibition. OnePetro. <https://doi.org/10.2118/186991-MS>.
- Gupta, R. and Mohanty, K. K. 2008, April. Wettability alteration of fractured carbonate reservoirs. In SPE Symposium on Improved Oil Recovery. OnePetro. <https://doi.org/10.2118/113407-MS>.
- Haugen, Å., Mani, N., Svenningsen, S., Brattækås, B., Graue, A., Ersland, G., and Fernø, M. A. 2014. Miscible and immiscible foam injection for mobility control and EOR in fractured oil-wet carbonate rocks. *Transport in porous media*, **104**(1), 109-131. <https://doi.org/10.1007/s11242-014-0323-6>.
- Hilgenfeldt, S., Koehler, S. A., and Stone, H. A. 2001. Dynamics of coarsening foams: accelerated and self-limiting drainage. *Physical review letters*, **86**(20), 4704. <https://doi.org/10.1103/PhysRevLett.86.4704>.
- Hirasaki, G. J. and Lawson, J. B. 1985. Mechanisms of foam flow in porous media: apparent viscosity in smooth capillaries. *Society of Petroleum Engineers Journal*, **25**(02), 176-190. <https://doi.org/10.2118/12129-PA>.
- Hirasaki, G. J. 1991. Wettability: fundamentals and surface forces. *SPE Formation Evaluation*, **6**(02), 217-226. <https://doi.org/10.2118/17367-PA>.
- Hirasaki, G.J., Miller, C.A., Szafranski, R., Lawson, J.B., and Akiya, N. 1997. Surfactant/foam process for aquifer remediation. In International symposium on oilfield chemistry. SPE 37257-MS. <https://doi.org/10.2118/37257-MS>.
- Hirasaki, G. and Zhang, D. L. 2003, February. Surface chemistry of oil recovery from fractured, oil-wet, carbonate formation. In International Symposium on Oilfield Chemistry. OnePetro. <https://doi.org/10.2118/80988-MS>.
- Hughes, R. G. and Blunt, M. J. 2001. Network modeling of multiphase flow in fractures. *Advances in Water Resources*, **24**(3-4), 409-421. [https://doi.org/10.1016/S0309-1708\(00\)00064-6](https://doi.org/10.1016/S0309-1708(00)00064-6).
- IEA. 2019. Number of EOR projects in operation globally, 1971-2017. Paris. <https://www.iea.org/data-and-statistics/charts/number-of-eor-projects-in-operation-globally-1971-2017>.
- Jones, S. A., Getrouw, N., and Vincent-Bonnieu, S. 2018a. Foam flow in a model porous medium: II. The effect of trapped gas. *Soft matter*, **14**(18), 3497-3503. <https://doi.org/10.1039/C7SM02458D>.
- Jones, S. A., Getrouw, N., and Vincent-Bonnieu, S. 2018b. Foam flow in a model porous medium: I. The effect of foam coarsening. *Soft matter*, **14**(18), 3490-3496. <https://doi.org/10.1039/C7SM01903C>.
- Kahrobaei, S., Li, K., Bonnieu, S. V., and Farajzadeh, R. 2018. Effects of compositional variations on CO₂ foam under miscible conditions. *AIChE Journal*. **64**(2) 758-764. <https://doi.org/10.1002/aic.15938>.
- Kalra, S. and Wu, X. 2014, April. CO₂ injection for enhanced gas recovery. In SPE Western North American and Rocky Mountain Joint Meeting. OnePetro. <https://doi.org/10.2118/169578-MS>.
- Kamali, F., Hussain, F., and Cinar, Y. 2017. An experimental and numerical analysis of water-alternating-gas and simultaneous-water-and-gas displacements for carbon dioxide enhanced oil recovery and storage. *SPE Journal*, **22**(02), 521-538. Paper Number: SPE-183633-PA.
- Katiyar, A., Patil, P. D., Rohilla, N., Rozowski, P., Evans, J., Bozeman, T., and Nguyen, Q. 2019, October. Industry-first hydrocarbon-foam EOR pilot in an unconventional reservoir: design, implementation, and performance analysis. In Unconventional Resources Technology Conference, Denver, Colorado, 22-24 July 2019 (pp. 233-255). Unconventional Resources Technology Conference (URTeC); Society of Exploration Geophysicists. <https://doi.org/10.15530/urtec-2019-103>.
- Kennedy, D. K., Kitziger, F. W., and Hall, B. E. 1992. Case study on the effectiveness of nitrogen foams and water zone diverting agents in multistage matrix acid treatments. *SPE production engineering*, **7**(02), 203-211. <https://doi.org/10.2118/20621-PA>.
- Khatib, Z. I., Hirasaki, G. J., and Falls, A. H. 1988. Effects of capillary pressure on coalescence and phase mobilities in foams flowing through porous media. *SPE reservoir engineering*, **3**(03), 919-926. <https://doi.org/10.2118/15442-PA>.
- Kil, R.A., Nguyen, Q.P., Rossen, W.R. 2011. Determining trapped gas in foam from computed-tomography images. *SPE Journal*, **16**(01), 24-34. <https://doi.org/10.2118/124157-PA>.
- Kim, J., Dong, Y., Rossen, W.R. 2005. Steady-state flow behavior of CO₂ foam. *SPE journal*, **10**(04), 405-415. <https://doi.org/10.2118/89351-PA>.

- Kovscek, A.R., Radke, C.J. 1994. Fundamentals of foam transport in porous media, in: L. L. Schramm (ed), *Foams in the Petroleum Industry*, Washington, D.C., Amer. Chem. Soc. 242, 115-163.
- Kovscek, A. R., Trethewey, D. C., Persoff, P., and Radke, C. J. 1995. Foam flow through a transparent rough-walled rock fracture. *Journal of Petroleum Science and Engineering*, **13**(2), 75-86. [https://doi.org/10.1016/0920-4105\(95\)00005-3](https://doi.org/10.1016/0920-4105(95)00005-3).
- Kovscek, A. R., Tang, G. Q., and Radke, C. J. 2007. Verification of Roof snap off as a foam-generation mechanism in porous media at steady state. *Colloids and Surfaces A: Physicochemical and Engineering Aspects*, **302**(1-3), 251-260. <https://doi.org/10.1016/j.colsurfa.2007.02.035>.
- Lake, L. W., Johns, R., Rossen, B., and Pope, G. A. 2014. *Fundamentals of enhanced oil recovery* (Vol. 1, p. 1). Richardson, TX: Society of Petroleum Engineers. ISBN: 978-1-61399-328-6.
- Lian, P. and Cheng, L. 2012. The characteristics of relative permeability curves in naturally fractured carbonate reservoirs. *Journal of Canadian Petroleum Technology*, **51**(02), 137-142. <https://doi.org/10.2118/154814-PA>.
- Luo, H., Mateen, K., Ma, K., Ren, G., Neillo, V., Blondeau, C., and Hirasaki, G. 2019, September. In-Depth Understanding of the Ultra-Low-Interfacial-Tension Foam Flood in Oil-wet Fractured Media through Simulation with an Integrative Mechanistic Foam Model. In SPE Annual Technical Conference and Exhibition. Society of Petroleum Engineers. <https://doi.org/10.2118/196123-MS>.
- Luthi, S. M. and Souhaite, P. 1990. Fracture apertures from electrical borehole scans. *Geophysics*, **55**(7), 821-833. <https://doi.org/10.1190/1.1442896>.
- Maloney, D. and Doggett, K. 1997. Multiphase flow in fractures. In Proceedings from the international symposium of the society of core analysts in Calgary, Calgary.
- March, R., Doster, F., and Geiger, S. 2018. Assessment of CO₂ storage potential in naturally fractured reservoirs with dual-porosity models. *Water Resources Research*, **54**(3), 1650-1668. <https://doi.org/10.1002/2017WR022159>.
- Marchalot, J., Lambert, J., Cantat, I., Tabeling, P., and Jullien, M. C. 2008. 2D foam coarsening in a microfluidic system. *EPL (Europhysics Letters)*, **83**(6), 64006. <https://doi.org/10.1209/0295-5075/83/64006>.
- Monnerneau, C. and Vignes-Adler, M. 1998. Dynamics of 3D real foam coarsening. *Physical Review Letters*, **80**(23), 5228. <https://doi.org/10.1103/PhysRevLett.80.5228>.
- Narr, W., Schechter, D. S., and Thompson, L. B. 2006. *Naturally fractured reservoir characterization* (Vol. 112). Richardson, TX: Society of Petroleum Engineers. ISBN: 978-1-55563-112-3.
- Nelson, R. 2001. *Geologic analysis of naturally fractured reservoirs*. Elsevier. Gulf Professional Publishing, Woburn, MA, USA, 2nd edition.
- Nguyen, Q. P. 2004. *Dynamics of Foam in Porous Media*, ISBN: 90-9017776-0.
- Nguyen, Q. P., Rossen, W. R., Zitha, P. L., and Currie, P. K. 2009. Determination of gas trapping with foam using X-ray computed tomography and effluent analysis. *SPE Journal*, **14**(02), 222-236. <https://doi.org/10.2118/94764-PA>.
- Ocampo-Florez, A., Restrepo, A., Rendon, N., Coronado, J., Correa, J. A., Ramirez, D. A., Torres, M., Sanabria, R., Lopera, S. H. 2014, December. Foams prove effectiveness for gas injection conformance and sweep efficiency improvement in a low porosity fractured reservoir–field pilots. In International Petroleum Technology Conference. OnePetro. <https://doi.org/10.2523/IPTC-17950-MS>.
- Ocampo, A., Restrepo, A., Clavijo, J., and Mejía, J. M. 2020, August. Successful Foams EOR Field Pilot in a Naturally Fractured Reservoir by the Injection of the Foaming Agent Dispersed in the Gas Stream. In SPE Improved Oil Recovery Conference. OnePetro. <https://doi.org/10.2118/200377-MS>.
- Odling, N. E. 1994. Natural fracture profiles, fractal dimension and joint roughness coefficients. *Rock mechanics and rock engineering*, **27**(3), 135-153.
- Olsson, R. and Barton, N. 2001. An improved model for hydromechanical coupling during shearing of rock joints. *International journal of rock mechanics and mining sciences*, **38**(3), 317-329. [https://doi.org/10.1016/S1365-1609\(00\)00079-4](https://doi.org/10.1016/S1365-1609(00)00079-4).
- Osterloh, W. T. and Jante, M. J. 1992, April. Effects of gas and liquid velocity on steady-state foam flow at high temperature. In SPE/DOE Enhanced Oil Recovery Symposium. OnePetro. <https://doi.org/10.2118/24179-MS>.
- Patzek, T. W. 1996. Field applications of steam foam for mobility improvement and profile control. *SPE Reservoir Engineering*, **11**(02), 79-86. <https://doi.org/10.2118/29612-PA>.

- Persoff, P. G., Pruess, K., and Myer, L. 1991. Two-phase flow visualization and relative permeability measurement in transparent replicas of rough-walled rock fractures. Presented at the 16th Workshop on Geothermal Reservoir Engineering, Stanford, CA.
- Persoff, P. and Pruess, K. 1995. Two-phase flow visualization and relative permeability measurement in natural rough-walled rock fractures. *Water resources research*, **31**(5), 1175-1186. <https://doi.org/10.1029/95WR00171>.
- Phelps, R. E. and Strauss, J. P. 2002. Capturing reservoir behavior by simulating vertical fracture and super-k zones in the Ghawar field. *SPE Reservoir Evaluation & Engineering*, **5**(04), 333-340. <https://doi.org/10.2118/79048-PA>.
- Pieters, D. A. and Graves, R. M. 1994, October. Fracture relative permeability: linear or non-linear function of saturation. In International Petroleum Conference and Exhibition of Mexico. OnePetro. <https://doi.org/10.2118/28701-MS>.
- Pope, G. A. 1980. The application of fractional flow theory to enhanced oil recovery. *Society of Petroleum Engineers Journal*, **20**(03), 191-205. <https://doi.org/10.2118/7660-PA>.
- Portois, C., Essouayed, E., Annable, M.D., Guiserix, N., Joubert, A., Atteia, O. 2018. Field demonstration of foam injection to confine a chlorinated solvent source zone. *Journal of contaminant hydrology*, **214**, 16-23. <https://doi.org/10.1016/j.jconhyd.2018.04.003>.
- Pruess, K. and Tsang, Y. W. 1990. On two-phase relative permeability and capillary pressure of rough-walled rock fractures. *Water Resources Research*, **26**(9), 1915-1926. <https://doi.org/10.1029/WR026i009p01915>.
- Radke, C.J., Gillis, J.V. 1990. A dual tracer technique for determining trapped gas saturation during steady foam flow in porous media. Paper SPE 20519 presented at the 65th Annual Technical Conference and Exhibition, New Orleans. In Tech. Conf. Exhib., New Orleans, LA. <https://doi.org/10.2118/20519-MS>.
- Ransohoff, T. C. and Radke, C. J. 1988. Mechanisms of foam generation in glass-bead packs. *SPE reservoir engineering*, **3**(02), 573-585. <https://doi.org/10.2118/15441-PA>.
- Rodríguez, F., Ortega, G., Sánchez, J. L., and Jiménez, O. 2001, April. Reservoir Management Issues in the Cantarell Nitrogen Injection Project. In Offshore Technology Conference. OnePetro. <https://doi.org/10.4043/13178-MS>.
- Romm, E. S. 1966. Flow characteristics of fractured rocks. Nedra, Moscow, 283.
- Rossen, W. R. and Kumar, A. T. 1992, October. Single-and two-phase flow in natural fractures. In SPE Annual Technical Conference and Exhibition. OnePetro. <https://doi.org/10.2118/24915-MS>.
- Rossen, W. R. 1996. Foams in enhanced oil recovery in *Foams: Theory, Measurements, and Application*, ed. Prud'homme, Robert K., 57, 413-464.
- Rossen, W. R. 1999. Foam in porous media. In *Foams and Emulsions* (pp. 335-348). Springer, Dordrecht.
- Rossen, W. R. 2003. A critical review of Roof snap-off as a mechanism of steady-state foam generation in homogeneous porous media. *Colloids and Surfaces A: Physicochemical and Engineering Aspects*, **225**(1-3), 1-24. [https://doi.org/10.1016/S0927-7757\(03\)00309-1](https://doi.org/10.1016/S0927-7757(03)00309-1).
- Saint-Jalmes, A. and Langevin, D. 2002. Time evolution of aqueous foams: drainage and coarsening. *Journal of Physics: Condensed Matter*, **14**(40), 9397.
- Sanchez Bujanos, J. L., Astudillo Abundes, A. V., Morales, J., and Rodriguez Torres, A. 2005, June. Nitrogen injection in the Cantarell complex: results after four years of operation. In SPE Latin American and Caribbean Petroleum Engineering Conference. OnePetro. <https://doi.org/10.2118/97385-MS>.
- Schechter, D. S., McDonald, P., Sheffield, T., and Baker, R. 1996, March. Reservoir characterization and CO₂ pilot design in the naturally fractured Spraberry trend area. In Permian Basin Oil and Gas Recovery Conference. OnePetro. <https://doi.org/10.2118/35469-MS>.
- Schramm, L. L. 1994. Foam sensitivity to crude oil in porous media. in *Foams, Fundamentals and Applications in the Petroleum Industry*, Advances in Chemistry Series 242, American Chemical Society, 165-197. <https://doi.org/10.1021/ba-1994-0242.ch004>.
- Seethapalli, A., Adibhatla, B., and Mohanty, K. K. 2004, April. Wettability alteration during surfactant flooding of carbonate reservoirs. In SPE/DOE symposium on improved oil recovery. OnePetro. <https://doi.org/10.2118/89423-MS>.
- Seyyedsar, S. M., Farzaneh, S. A., and Sohrabi, M. 2015, September. Enhanced heavy oil recovery by intermittent CO₂ injection. In SPE Annual Technical Conference and Exhibition. OnePetro. <https://doi.org/10.2118/175140-MS>.

- Skoreyko, F. A., Villavicencio, A. P., Rodriguez Prada, H., and Nguyen, Q. P. 2012, January. Understanding foam flow with a new foam EOR model developed from laboratory and field data of the naturally fractured cantarell field. In SPE improved oil recovery symposium. Society of Petroleum Engineers. <https://doi.org/10.2118/153942-MS>.
- Spirov, P., Rudyk, S. N., and Khan, A. 2012, February. Foam assisted WAG, Snorre Revisit with new foam screening model. In North Africa Technical Conference and Exhibition. OnePetro. <https://doi.org/10.2118/150829-MS>.
- Stearns, D. W. and Friedman, M. 1972. Reservoirs in fractured rock: Geologic exploration methods, 82-106.
- Steinsbø, M., Brattekkås, B., Ersland, G., Bø, K., Opdal, I. E., Tunli, R., Graue, A., Fernø, M. A. 2015, April. Foam as mobility control for integrated CO₂-EOR in fractured carbonates. In IOR 2015-18th European Symposium on Improved Oil Recovery (pp. cp-445). European Association of Geoscientists & Engineers. <https://doi.org/10.3997/2214-4609.201412125>.
- Tang, G.Q., Kovscek, A.R. 2006. Trapped gas fraction during steady-state foam flow. *Transport in porous media*, **65**(2), 287-307. <https://doi.org/10.1007/s11242-005-6093-4>.
- Tang, J., Vincent-Bonnieu, S., and Rossen, W. R. 2019, September. CT Coreflood Study of Transient Foam Flow with Oil. In SPE Annual Technical Conference and Exhibition. Society of Petroleum Engineers. <https://doi.org/10.2118/196202-MS>.
- Teigland, R. and Kleppe, J. 2006, April. EOR survey in the North Sea. In SPE/DOE Symposium on Improved Oil Recovery. OnePetro. <https://doi.org/10.2118/99546-MS>.
- Thompson, K.E. and Gdanski, R.D. 1993. Laboratory study provides guidelines for diverting acid with foam. *SPE Production & Facilities*, **8**(04), 285-290. <https://doi.org/10.2118/23436-PA>.
- Tsang, Y. W. 1984. The effect of tortuosity on fluid flow through a single fracture. *Water Resources Research*, **20**(9), 1209-1215. <https://doi.org/10.1029/WR020i009p01209>.
- Tsang, Y. W. 1992. Usage of "equivalent apertures" for rock fractures as derived from hydraulic and tracer tests. *Water Resources Research*, **28**(5), 1451-1455. <https://doi.org/10.1029/92WR00361>.
- van Golf-Racht, T. D. 1982. Fundamentals of fractured reservoir engineering. Elsevier.
- von Neumann, J. 1952. Metal interfaces. American Society for Metals, Cleveland, 108.
- Weaire, D. L. and Hutzler, S. 2001. The physics of foams. Oxford University Press.
- Weaire, D. 2008. The rheology of foam. Current Opinion in *Colloid & Interface Science*, **13**(3), 171-176. <https://doi.org/10.1016/j.cocis.2007.11.004>.
- Witherspoon, P. A., Wang, J. S., Iwai, K., and Gale, J. E. 1980. Validity of cubic law for fluid flow in a deformable rock fracture. *Water resources research*, **16**(6), 1016-1024. <https://doi.org/10.1029/WR016i006p01016>.
- Wonnacott, T.H. and Wonnacott, R.J. 1972. Introduction statistics for Business and Economics. John Wiley and Sons.
- Yan, W., Miller, C. A., and Hirasaki, G. J. 2006. Foam sweep in fractures for enhanced oil recovery. *Colloids and Surfaces A: Physicochemical and Engineering Aspects*, **282**, 348-359. <https://doi.org/10.1016/j.colsurfa.2006.02.067>.
- Yang, S. H. and Reed, R. L. 1989, October. Mobility control using CO₂ forms. In SPE Annual Technical Conference and Exhibition. OnePetro. <https://doi.org/10.2118/19689-MS>.

ACKNOWLEDGEMENTS

The past four years of my Ph.D. is a wonderful academic journey for me, with many setbacks and successes. I acknowledge the sponsorship of **Joint Industry Project (JIP)** on Foam for Enhanced Oil Recovery (funded by Shell, Equion, Engie, ConocoPhillips, and PEMEX) at Delft University of Technology. The experimental work in this dissertation was conducted in **Geo-energy & Geoscience and Engineering Laboratory** at Delft University of Technology.

I would like to express my deep gratitude to **prof.dr. W.R. Rossen** and **dr. S. Vincent-Bonnieu**, for hiring me for this research. I thank my promotor **prof.dr. W.R. Rossen** for your insightful opinions and constructive suggestions on my doctoral work. I appreciate how patient and prudent you are when you treat our work and how zealous you are to offer me help whenever I need it. I learn much from you on how to reflect on our study and how to deliver practical implications. I enjoy our meetings, where there is always something to draw out to improve my academic skill. I thank my promotor **dr. K-H.A.A. Wolf** for helping me to complete my work, especially in terms of how to create model fractures that best represent real natural fractures. I learn from you how to be tolerant of uncertainty in research. Thank you for our meetings where I always get support and comfort. I also thank **dr. Janice Rossen** for showing confidence in my study. I appreciate your enthusiasm and cordiality.

I would like to thank **prof.dr. H. Bertin**, **prof.dr. R.A.W.M. Henkes**, **prof.dr. P.L.J. Zitha**, **dr. A. Pluymakers**, and **dr. S. Vincent-Bonnieu** for being independent members of my doctoral committee, and for evaluating and improving my dissertation.

I thank **Michiel Slob** for your technical help on our experimental setup. Your expertise in the laboratory contributes much to this doctoral study. I give my appreciation to **Marlijn Ammerlaan**, **Jens van den Berg**, **Lydia Broekhuijsen-Bentvelzen**, **Marc Friebel**, **Jolanda van Haagen-Donker**, **Ralf Haak**, **Karel Heller**, **Regina Hoffmann**, **Ellen Meijvogel-de Koning**, **Guus Lohlefink**, **Joost van Meel**, **Nancy van Veen**, **Paul Vermeulen**, and **Wim Verwaal** for your kind help in the office and laboratory.

I thank faculty members **prof.dr. G. Bertotti**, **prof.dr. J. Bruining**, **prof.dr. P.L.J. Zitha**, **dr. A. Barnhoorn**, **dr. R. Farajzadeh**, and **dr. D. Voskov**, for your discussion on my doctoral study, from where I get many ideas to improve my work.

I thank my colleagues and friends **dr. B.I. AlQuaimi**, **dr. C. Boeije**, **dr. R.S. Castillo**, **dr. J. Gong**, **dr. A. Hussain**, **dr. M. Janssen**, **dr. S. Jones**, **dr. S. Kahrobaei**, **dr. M. Khait**, **dr. X. Lyu**, **dr. R. Prabhakaran**, **dr. S. Shah**, **dr. J. Tang**, **dr. Y. (Yang) Wang**, **dr. Y. (Yuhang) Wang**, **dr. M.M. Yegane**, **dr. G. Yu**, **Siamak Abolhassani**, **Peter Jan Bleeker**, **Ellis Bouw**, **Michael Epke**, **Shihao Fu**, **Martijn Hurkmans**, **Naveen Ilango**, **Yap Fu Kai**, **Anna Kottsova**, **Kishan Ramesh Kumar**, **Thom Leo**, **Tim Maas**, **Muhammad Mohsan**, **Frank Pennekamp**, **Ana Rodríguez Palmeiro**, **Kiarash Mansour Pour**, **Daan Thomassen**, **Xiaoming Tian**, **Fanxiang Xu**, **Michiel Wapperom** for every moment we share together. I also thank **Delft Chinese Football Club**, **Delft Comedy Football Club**, and **Delft Chinese Badminton Team**. I have much fun playing games with friends in these groups.

I am grateful to my mother **Wang Huajun**, my father **Li Yide**, my mother-in-law **Wang Guirong**, my father-in-law **Liu Suo**, my sister-in-law **Liu Li**, my brother **Li Lei**, and all other **families**, who have been by my side to back me up, for holding strong confidence in my capacity. I am grateful to my wife **Liu Naiyi** for believing in me and helping me in life. I am grateful to your company!

SCIENTIFIC CONTRIBUTION

Journal publications:

5. Li, K., Wolf, K. H. A., and Rossen, W. R. 2021. Effects of Gas Trapping on Foam Mobility in a Model Fracture. *Transport in Porous Media*, **138**(1), 185-200. <https://doi.org/10.1007/s11242-021-01598-y>.
4. Li, K., Wolf, K. H. A., and Rossen, W. R. 2021. Effects of Gravity on Foam Behaviour in Roughened Model Fractures. *SPE Journal*. <https://doi.org/10.2118/206735-PA>.
3. Li, K., Wolf, K. H. A., and Rossen, W. R. 2021. A Novel Technique to Estimate Water Saturation and Capillary Pressure of Foam in Model Fractures. *Colloids and Surfaces A: Physicochemical and Engineering Aspects*. <https://doi.org/10.1016/j.colsurfa.2021.127800>.
2. Li, K., Sharifnik, M., Wolf, KH., and Rossen., W.R. 2021. Coarsening of Foam in Two Model Fractures with Different Roughness. *Colloids and Surfaces A: Physicochemical and Engineering Aspects*. <https://doi.org/10.1016/j.colsurfa.2021.127666>.
1. Kahrobaei, S., Li, K., Bonnieu, S. V., and Farajzadeh, R. 2018. Effects of compositional variations on CO₂ foam under miscible conditions. *AIChE Journal*. **64**(2) 758-764. <https://doi.org/10.1002/aic.15938>.

Conference proceedings:

9. Li, K., Sharifnik, M., Wolf, KH., and Rossen., W.R. 2021. Coarsening of Foam in Two Model Fractures with Different Roughness. In EAGE Annual 82nd Conference & Exhibition, 18-21 October 2021, Amsterdam, The Netherlands. European Association of Geoscientists & Engineers. <https://doi.org/10.3997/2214-4609.202113048>.
8. Li, K., Wolf, K. H. A., and Rossen, W. R. 2021. A Novel Technique of Image Analysis on Foam in Fractures. InterPore2021, 31 May 2021 to 4 June 2021, Online conference.
7. Li, K., Sharifnik, M., Wolf, KH., and Rossen., W. R. 2021. A Laboratory Study of Foam Coarsening in Model Fractures. InterPore2021, 31 May 2021 to 4 June 2021, Online conference.
6. Li, K., Wolf, K. H. A. A., and Rossen, W. 2021, April. An Experimental Study of Foam Trapping and Foam Mobility in a Model Fracture. In IOR 2021 (Vol. 2021, No. 1, pp. 1-10). Vienna, Austria. European Association of Geoscientists & Engineers. <https://doi.org/10.3997/2214-4609.202133018>.
5. Li, K., Rossen, W., and Wolf, K. 2020, December. An Experimental Study of the Effect of Gravity on Foam in Fractures. In 82nd EAGE Annual Conference & Exhibition (Vol. 2020, No. 1, pp. 1-5). Amsterdam, The Netherlands. European Association of Geoscientists & Engineers. <https://doi.org/10.3997/2214-4609.202011063>.
4. Li, K., Wolf, K. H. A., and Rossen, W. R. 2020. Effects of Gas Trapping on Foam Mobility in a Model Fracture. EUFOAM 2020 Conference, 6-9 July, 2020, Aberystwyth, United Kingdom.
3. Li, K., Wolf, K. H. A., and Rossen, W. R. 2020. An Investigation of the Effect of Gravity on Foam in Model Fractures. InterPore2020, 31 August 2020 to 4 September 2020, Qingdao, China.
2. Li, K., Wolf, K. H. A., and Rossen, W. R. 2020. Foam Trapping and Foam Mobility in a Model Fracture. InterPore2020, 31 August 2020 to 4 September 2020, Qingdao, China.
1. Kahrobaei, S., Li, K., Bonnieu, S. V., and Farajzadeh, R. 2017, April. Effects of compositional variations on CO₂ foam under miscible conditions. In IOR 2017-19th European Symposium on Improved Oil Recovery (Vol. 2017, No. 1, pp. 1-12). European Association of Geoscientists & Engineers. <https://doi.org/10.3997/2214-4609.201701793>.